

Department of Civil Engineering
University College London
University of London

NONLINEAR DYNAMICS AND CHAOS: THEIR RELEVANCE TO SAFE
ENGINEERING DESIGN

BY MOHAMED SANAA SOLIMAN

Thesis submitted for the degree of Doctor of Philosophy
October 1990

ProQuest Number: 10631501

All rights reserved

INFORMATION TO ALL USERS

The quality of this reproduction is dependent upon the quality of the copy submitted.

In the unlikely event that the author did not send a complete manuscript and there are missing pages, these will be noted. Also, if material had to be removed, a note will indicate the deletion.



ProQuest 10631501

Published by ProQuest LLC (2017). Copyright of the Dissertation is held by the Author.

All rights reserved.

This work is protected against unauthorized copying under Title 17, United States Code
Microform Edition © ProQuest LLC.

ProQuest LLC.
789 East Eisenhower Parkway
P.O. Box 1346
Ann Arbor, MI 48106 – 1346

To God and my parents.

ACKNOWLEDGMENTS

I am particularly grateful to my supervisor, Professor J.M.T. Thompson, for his guidance and support throughout this research.

I would also like to thank my colleagues and teaching staff at U.C.L, namely; Dr. Erol Yarimer, Dr. Nick Alexander, Dr. Steve Bishop, Dennis Leung and Dr. Lawrence Virgin for their simulating discussions. I would also like to thank Nigel Stocks and Dr. R. Mannella, Lancaster University, for supplying data used in chapter four. Special thanks go to Rod Rainey, of W.S. Atkins, for his simulating discussions on ship capsize.

It is also a pleasure to acknowledge the support from the Department of Civil Engineering at University College, namely Prof. K.J. Ives and Mike Gregory; and grants from the Science and Engineering Research Council of Great Britain.

I would also like to thank my friends and colleagues in the postgraduate Structures Laboratory for their help: Manou, Christos, Behrokh, Ali, Xion-Nian and Esi.

I also thank Dr. Mohsin Mirza and Nabila Kauwaf for their support.

I owe a special debt of gratitude to my parents and sister for their encouragement.

Abstract

As many engineering systems are neither linear nor nearly linear, they are normally modelled by nonlinear equations for which closed-form analytical solutions are unobtainable. However with the advent of powerful computers, equations can be readily integrated numerically, so that the response from a given set of starting conditions is easily established. Unlike linear systems where all initial conditions lead to one type of motion, be it to an equilibrium point or to a harmonic oscillation, nonlinear systems can exhibit chaotic transients which can settle down to a rich and complex variety of competing steady state solutions.

Associated with each steady state solution is its basin of attraction. Under the variation of a control parameter, as the attractors move and bifurcate, the basins also undergo corresponding changes and metamorphoses. Associated with the homoclinic tangling of the invariant manifolds of the saddle solution, basin boundaries can change in nature from smooth to fractal, resulting in regions of chaotic transients.

The aim of the thesis is to investigate how the size and nature of the basin of attraction changes with a control parameter. We show that there can exist a rapid loss of engineering integrity accompanying the rapid erosion and stratification of the basin.

We explore the engineering significance of the basin erosions that occur under increased forcing. Various measures of engineering integrity are introduced: a global measure assesses the overall basin area; a local measure assesses the distance from the attractor to the basin boundary; a velocity measure is related to the size of impulse that could be sustained without failure; and a stochastic integrity measure assesses the stability of an attractor subjected to an external noise excitation. Since engineering systems may be subjected to pulse loads of finite duration, attention is given to both the absolute and transient basins of attraction. The significant erosion of these at homoclinic tangencies is particularly high-lighted in the present study, the fractal basins having a severely reduced integrity under all four criteria.

We also apply the basin erosion phenomena to the problem of ship capsizing. We make a numerical analysis of the steady state and transient motions of the semi-empirical nonlinear differential equations, which have been used to model the resonant rolling motions of real ships. Examination of the safe basin in the space of the starting conditions shows that transient capsize can occur at a wave height that is a small fraction of that at which the final steady state motions lose their stability. It is seen that the basin is eroded quite suddenly throughout its central region by gross striations, implying that transient capsizing might be a reasonably repeatable phenomenon, offering a new approach to the quantification of ship stability in waves.

We conclude from this thesis that the stability of nonlinear engineering systems may, in the future, be based on the basin erosion phenomenon relating to chaotic transients and incursive fractals.

Table of Contents

1 INTRODUCTION	1
2 BACKGROUND THEORY	5
2.1 The Poincaré map	5
2.2 Stability of the steady state	6
2.3 Response and bifurcations	9
2.4 Basins of attraction	10
Figures	13
3 INTEGRITY MEASURES AND BASIN EROSION	17
3.1 Introduction	17
3.2 Transient basins and integrity measures	18
3.3 Numerical simulations	20
3.4 Choices of frequencies	20
3.5 Erosion of the basin of attraction	22
3.5.1 Results for $\omega=3.4$	22
3.5.2 Results for $\omega=2.4$	24
3.5.3 Results for $\omega=1.0$ and $\omega=0.85$	25
3.5.4 Results for $\omega=0.65$	27
3.6 Tangling and detangling	28
3.7 Local integrity of the attractor	30
3.7.1 Local integrity measures	31
3.7.2 Impact loading	33
3.8 Summary of chapter	34
Figures	37
4 STOCHASTIC ANALYSIS	49
4.1 Stochastic integrity measures	50
4.2 Numerical simulations	52
4.2.1. Stochastic integrity	52
4.2.2. Noise modelling	53
4.3 Noise sensitivity of attractors	56
4.3.1 Varying noise intensity	56
4.3.2 Comparison with analogue simulations	57
4.3.3 Stochastic integrity curves	59
4.3.4 Correlation between stochastic integrity and basin of attraction	61

4.3.5 Noise modelling	63
4.4 Summary of chapter	63
Figures	66
5 ENGINEERING RELEVANCE OF BASIN EROSION AND CHAOTIC TRANSIENTS	73
5.1 Introduction	73
5.2 Fractal boundaries in control space	74
5.3 Four dimensional phase-control space	75
5.4 Control space basins and the escape boundary	76
5.5 Fractal dimension	78
5.6 Transient basins as a new approach to ship capsize	80
5.6.1 Ship capsize as the escape from a potential well	80
5.6.2 Relevance of current study	81
5.6.3 Computer time integrations must replace analysis	81
5.6.4 Complexity and irrelevance of the steady states	82
5.6.5 Transient basins and engineering integrity curves	84
5.6.6 Dramatic and dangerous erosion of the safe basin	85
5.6.7 Control space basin as a transient capsize diagram	86
5.6.8 Implications for wave-tank experiments	86
5.7 Design against earthquakes	87
5.8 Summary of chapter	87
Figures	89
6 APPLICATION TO SHIP CAPSIZE	94
6.1 Introduction	94
6.2 Mathematical modelling and the general roll equation	96
6.3 Background theory	99
6.4 Steady state behaviour	100
6.4.1 Steady state roll response	100
6.4.2 Steady state bifurcation diagram	102
6.5 Transient behaviour	104
6.5.1 Safe basins	104
6.5.2 Erosion of the safe basins	106
6.5.3 Transient capsize diagram	108

6.6 Roll Damping	109
6.7 Conclusions	110
Figures	113
7 CONCLUSIONS	125
REFERENCES	129

CHAPTER 1: INTRODUCTION

There are many vibratory problems in engineering. Structures subjected to earthquakes, ships subjected to wind and waves or bridges subjected to vehicle and environmental conditions are just a few examples to mention. Differential equations, which represent the essential aspects of the structure and sufficiently describe the dynamics of the system, may often be used to model such problems. However as real-world problems are neither linear or nearly linear, they are normally modelled by nonlinear equations for which closed-form analytical solutions are unobtainable. However there has been a spectacular growth in nonlinear dynamics in recent years, made possible on one hand by great theoretical strides in Poincaré's qualitative topological approach and on the other hand by the wide availability of powerful computers. This has allowed equations to be readily integrated numerically, so that the response from a given set of starting conditions is easily established. Typical dynamical systems exhibit a start up transient, after which the motions settles down to some form of long term recurrent behaviour. Unlike linear systems where all initial conditions lead to one type of motion; be it to an equilibrium point or to a harmonic oscillation, nonlinear systems can exhibit a rich and complex variety of competing steady state solutions.

The phase portraits of many nonlinear systems are often characterized by the existence of one or more stable attractors, which typically include point equilibria, periodic oscillations (harmonic and subharmonic), quasi-periodic solutions and chaotic attractors. Each attractor is embedded in its own domain or basin of attraction, bounded by a separatrix associated with an unstable saddle solution. Indeed much work has been done on how point, periodic, quasi-periodic and chaotic attractors are created, changed and destroyed as a system parameter is varied. The mechanisms include the well-known local bifurcations, together with subharmonic cascades, intermittencies, crises, etc. In

addition it is important to recognize that in typical dynamical systems several attractors often coexist at fixed parameter values. This has lead to much interest in basins of attraction, and how they too undergo changes and metamorphoses. Under the variation of a control parameter, as the attractors move and bifurcate, the basins also undergo corresponding changes and metamorphoses. These changes in size and shape are usually continuous but can be discontinuous as when an attractor vanishes, along with its basin, at a saddle-node bifurcation. Associated with the homoclinic tangling of the invariant manifolds of the saddle solution, basin boundaries can also change in nature from smooth to fractal.

The aim of the thesis is to investigate how the size of the basin of attraction changes with a control parameter. We show that there can exist a rapid loss of engineering integrity accompanying the rapid erosion and stratification of the basin. This as we shall show in subsequent chapters has important practical and theoretical implications.

As an illustrative example we shall consider the problem of the sinusoidally forced motions of a particle in a single potential well, $V=x^2/2 - x^3/3$. This system is chosen because the escape of a dynamical system is a recurrent theme in physics and engineering. In the field of marine engineering, for example, the roll response of a vessel in regular seas can be modelled by this type of problem (Thompson, Bishop & Leung, 1986).

We thus consider the mechanical oscillator with the single generalised co-ordinate x described by the equation;

$$\ddot{x} + \beta\dot{x} + x - x^2 = F \sin \omega t \quad (\dot{x} \equiv y) \quad (1.1)$$

where β , ω , F are system parameters and a dot denotes differentiation with respect to time.

In chapter 2 we give a brief outline of nonlinear dynamical phenomena, as well as introducing the basic techniques used in nonlinear dynamics to investigate periodically forced mechanical oscillators.

In chapter 3 we explore the engineering significance of the basin erosions that occur under increased forcing. Various measures of engineering integrity of the constrained attractor are introduced: a global measure assesses the overall basin area; a local measure assesses the distance from the attractor to the basin boundary; and a velocity measure is related to the size of impulse that could be sustained without failure.

Since engineering systems may be subjected to pulse loads of finite duration, attention is given to both the absolute and transient basin boundaries. The significant erosion of these at homoclinic tangencies is particularly high-lighted in the present study, the fractal basins having a severely reduced integrity under all three criteria.

Chapter 4 examines the dynamical response of attractors subjected to external fluctuations. Introducing a superimposed noise excitation, we quantify the response in terms of a stochastic integrity measure, and correlate this with the geometrical changes experienced by the deterministic basin of attraction.

In chapter 5 we investigate the four dimensional phase-control space spanned by $\{x(0), \dot{x}(0), F, \omega\}$. We explore the engineering significance of the control cross-section corresponding for example to $x(0), \dot{x}(0) = 0$. The fractal boundary in this section is a failure locus for a mechanical system subjected, while resting in its ambient state, to a sudden pulse of excitation. We assess the relative magnitude of the uncertainties implied by this fractal structure. Absolute and transient basins are examined giving control-space maps analogous to familiar pictures of the Mandelbrot set. Generalising from this prototype study, it is argued that in engineering design, against boat capsize or earthquake damage, for example, a study of the safe basins should augment, and perhaps entirely replace, conventional analysis of the steady state attracting solutions.

In chapter 6 we apply the ideas presented in the previous chapters to the problem of ship capsize. We make a numerical analysis of the steady state and transient motions of the semi-empirical nonlinear differential equations, which have been used to model the resonant rolling motions of two ships. Examination of the safe basin in the space of the starting conditions shows that transient capsizes can occur at a wave height that is a small fraction of that at which the final steady state motions lose their stability. It is seen that the basin is eroded quite suddenly throughout its central region by gross striations, implying that transient capsize might be a reasonably repeatable phenomenon, offering a new approach to the quantification of ship stability in waves. Such an approach has the twin advantages of being both conceptually simpler, and at the same time more relevant, than one based on the steady state rolling motions. The latter analysis can be dangerously non-conservative.

A summary and conclusion of the thesis is presented in chapter 7. We also outline the research that should be made in the near future, on both the theoretical and practical levels, concerning the ideas presented in this thesis.

CHAPTER 2: BACKGROUND THEORY

In this chapter we give a general outline of nonlinear dynamical phenomena. Readers desiring a more detailed discussion in classical nonlinear vibrations should consult books like Nafyeh and Mook (1979). New concepts in nonlinear dynamics such as chaos are excellently reviewed in books by Thompson and Stewart (1986), Moon (1987) and Guckenheimer and Holmes (1983). We also introduce the basic techniques used in nonlinear dynamics to investigate periodically forced vibratory systems. We pay particular attention to *forced* or *driven* mechanical oscillators, described for example by the non-autonomous differential equation

$$m\ddot{x} + f(x, \dot{x}) = F \sin \omega t \quad (2.1)$$

Here the forcing is sinusoidal with a magnitude of F and a frequency of ω , and the phase space is three-dimensional spanned by x, \dot{x} and t . This phase space is full of non-crossing trajectories which spiral around the time axis looking like a stranded cable. It is sometimes convenient to plot the *phase projection* in the subspace of x and \dot{x} , but here the trajectories will constantly cross one another.

We notice here that this non-autonomous second-order differential equation can be converted into three first-order equations if we set $\dot{x} = y$ and employ the standard trick of regarding t as one of the variables with the third equation simply $\dot{t} = 1$.

2.1 The Poincaré Map

A standard technique in dealing with the three-dimensional phase space (x, \dot{x}, t) of our periodically driven oscillator is to inspect the projection (x, \dot{x}) whenever t is a

multiple of $T = (2\pi/\omega)$ as shown in figure 2.1. Here T is the periodic time of the forcing. Clearly a similar trajectory bundle emerges from each $t=mT$ plane ($m=0,1,2,3,\dots$) so that photographs of every interval would be identical. This does not mean that a particular trajectory repeats itself with period T ; the one shown in figure 2.1 repeats itself every $2T$. The repetition after T of the trajectory bundle is conveniently treated in topological dynamics by imagining the whole bundle of one interval twisting back onto itself forming a torus. Most of these trajectories will represent *transient motions*, but within the bundle of a dissipative system will usually exist some *steady state* trajectories, or *attractors*. In many nonlinear systems there can be many competing attractors, repellers and saddles.

If the steady state trajectory repeats itself with period T of the forcing, the corresponding oscillation is usually termed the *fundamental solution*. If it repeats itself after n intervals, so that it has period nT it is called a *subharmonic of order n* (figure 2.1 shows an $n=2$ subharmonic). A steady state attractor that never repeats itself is usually termed a *chaotic attractor*. The result of inspecting the phase projection at only the specific times $t=mT$, is to see a sequence of dots, representing the so-called Poincaré mapping. Transient motions would appear as a sequence of dots and the emergence of a stable fundamental solution would be seen as a repetition of just one fixed mapping point. A subharmonic of order n would be a systematic jumping between n mapping points. A chaotic attractor would appear a scatter of points on an ordered fractal structure that never repeat themselves.

2.2 Stability of the steady state

As was shown in the previous section, the Poincaré mapping technique for flows allows us to condense the behaviour of three-dimensional trajectories to a mapping

of a two-dimensional surface of section to itself. Thus the stability properties of the map reflect the stability properties of the flow. In this section we outline how this is done by considering equation (1.1) as an illustrative example. In order to do so we can write equation (1.1) as set of three autonomous first order equations

$$\begin{aligned}\dot{x} &= y \\ \dot{y} &= -x + x^2 - \beta y + F \sin \phi \\ \dot{\phi} &= \omega\end{aligned}\tag{2.2}$$

with the three controls (F, ω, β) .

The divergence of trajectories in the three dimensional phase space, R^3 , spanned by (x, y, t) , is governed by

$$\frac{\partial \dot{x}}{\partial x} + \frac{\partial \dot{y}}{\partial y} + \frac{\partial \dot{\phi}}{\partial \phi} = -\beta\tag{2.3}$$

so we have a constant exponential contraction, of the phase volume, V , according to

$$\dot{V} = -\beta V\tag{2.4}$$

$$V(t) = V(0)e^{-\beta t}$$

We now introduce Poincaré sections (x, y) defined by

$$t = t_p + iT \left(i = 1, 2, \dots, T = \frac{2\pi}{\omega} \right)\tag{2.5}$$

$$\phi = \phi_p = \omega t_p$$

and the associated map

$$P(\phi_p): \{x(t_p), y(t_p)\} \rightarrow \{x(t_p + T), y(t_p + T)\}\tag{2.6}$$

This maps takes us iteratively from (x_i, y_i) to (x_{i+1}, y_{i+1}) according to an implied functional relationship

$$x_{i+1} = G(x_i, y_i) \quad (2.7)$$

$$y_{i+1} = H(x_i, y_i)$$

where G and H can be evaluated numerically for any (x_i, y_i) by making a Runge-Kutta numerical time integration through one forcing period.

Let $x_i + x^E$ and $y_i + y^E$ be a fixed point of (2.7), and superimposing a small disturbance, we get

$$x_{i+1} = x^E + \zeta_{i+1} = G(x^E + \zeta_{i+1}, y^E + \eta_{i+1}) \quad (2.8)$$

$$y_{i+1} = y^E + \eta_{i+1} = H(x^E + \zeta_{i+1}, y^E + \eta_{i+1})$$

Expanding G and H in a Taylor series at the fixed point, retaining only the linear part of the expansion, and abbreviating the first derivatives as a, b, c, d we obtain the variational equation

$$\zeta_{i+1} = a\zeta_i + b\eta_i \quad (2.9)$$

$$\eta_{i+1} = c\zeta_i + d\eta_i$$

or in matrix form

$$\gamma_{i+1} = M\gamma_i$$

The eigenvalues Λ_1, Λ_2 , of the matrix M, thus determine the stability criterion for two-dimensional maps which is best discussed in the complex plane. If the eigenvalues are both inside the unit circle the system is stable; if at least one of the eigenvalues is outside the unit circle the system is unstable. The stability boundary is the unit circle itself. If the eigenvalues are real there are only two points at which they can cross the stability boundary, at $\Lambda = \pm 1$. When one of the eigenvalues say Λ_1 , is equal to 1 and $|\Lambda_2| < 1$ the system is in a state of *incipient divergence*; when Λ_1 is equal to -1 and $|\Lambda_2| < 1$, the system in a state of *incipient flip*. These types of instability are essentially one-dimensional, involving only one eigenvalue. If the

eigenvalues are complex conjugate they can cross the unit circle at an angle $\theta \neq 0, \pi$ and is called a *Neimark instability*. Figure 2.2 shows the stability transitions for the equilibrium states of flows and maps in the complex plane (Thompson & Stewart, 1986).

2.3 Response and bifurcations

Nonlinear systems can have many steady state solutions, which can be stable or unstable, at a fixed set of control parameters. Once these are found they can be followed as paths under the variation of a primary control, while bifurcations of these paths can be followed in control space under the variation of a second parameter.

The response of these steady states, under the variation of a control parameter, can be very complex indeed (Thompson, 1989). Unlike linear systems where the solutions are invariably harmonic, nonlinear systems can exhibit harmonic, subharmonic, quasi-periodic or even chaotic oscillations. In this section we outline a "typical" sequence of attractor bifurcations, which can occur in many nonlinear oscillators. We use the oscillator described by (1.1), as an illustrative example.

Figure 2.3 shows a schematic response curve with the corresponding stability transitions.

From S^0 , the path S^1 starts as an attracting focus, becomes a directly attracting node at a where the eigenvalues becomes real and positive, and folds at A where Λ_1 penetrates the unit circle. From fold A to fold B we have a directly unstable saddle D_r^1 (where r for resonant distinguishes this from the hilltop saddle D^1), and the path restabilizes at fold B as Λ_1 re-enters the unit circle at +1. Physically however, folds A and B give rise to a region of resonant hysteresis where the two stable attractors

are separated by an $n=1$ solution which is directly unstable with both eigenvalues positive and real with $1 < \Lambda_1 < \infty$, $0 < \Lambda_2 < 1$. This results in jumps to and from resonance at A and B respectively. Λ_1 then becomes complex at b, passing completely around the unit circle to give an inversely attracting node with real negative eigenvalues between c and C. At C, Λ_1 passes out of the unit circle at -1, and we have a supercritical flip bifurcation into a $n=2$ stable subharmonic. This is followed by a supercritical flip from an $n=2$ to an $n=4$, and a complete period-doubling cascade leading to a chaotic attractor, which quickly becomes unstable at a boundary crisis at E leaving no attractor and an inevitable jump to escape. The unstable $n=1$ solution meanwhile continues to the fold G where it turns back to become the hill-top saddle cycle D^1 . Before doing so however it is clear that from the constraints on the eigenvalues (Thompson, 1989) that we must have a reversed flip at F, and this is indeed confirmed by our numerical results. There is indeed a complete reversed period-doubling and chaos as illustrated. The reversed flip F is, indeed very close to G so that the stable $n=1$ regime F-f-g-G is in reality very short. Path D^1 finally returns to the hill-top equilibrium D^0 . *Steady state bifurcation diagrams* in control-space, clearly summarise the parameter values at which important bifurcations take place. This is described in more detail in the next chapter.

2.4 Basins of attraction

In damped linear systems, at a fixed set of parameter values, all initial conditions eventually lead to one possible steady state motion; this can be an equilibrium point or a harmonic oscillation. However in nonlinear systems, it is possible for several attractors to co-exist at a fixed set of control parameters. This is clearly illustrated in figure 2.4 for our escape equation. Here the (x,y) phase space has two equilibria

position at $x=0$ and $x=1$. The stable state S^0 of minimum energy at $(0,0)$ corresponds to an attracting focus, while the unstable state D^0 of the maximum energy at $(1,0)$ corresponds to a saddle. The *stable manifold, or inset*, of this saddle, namely the set of all points that tend to the saddle as $t \rightarrow \infty$, defines the *basin boundary, or seperatrix*, around the basin of attraction of S^0 . Starting conditions outside this basin that lead to escape over the hill-top (with $x \rightarrow \infty$) are highlighted by the dot screen.

There are several techniques for determining basins of attraction based on the Poincaré mapping techniques that we have introduced earlier. To elaborate this, we can consider that equation (2.1) can be written as two first-order equations

$$\begin{aligned}\dot{x} &= X(x, y, t) \\ \dot{y} &= Y(x, y, t)\end{aligned}\tag{2.10}$$

where X and Y are both periodic in t , with the same period L . Suppose that $x(t)$ and $y(t)$ are the solutions, starting at a point P^0 in the (x,y) phase projection. So P^0 has the co-ordinates $x(0)$, $y(0)$. We study the Poincaré mapping, looking at the points P_m at the time $t=mL$, where $m=0,1,2 \dots$. We call the transformation $P_0 \rightarrow P_1$ the mapping, T , and write $P_1 = TP_0$. In an extension of this notation we can write

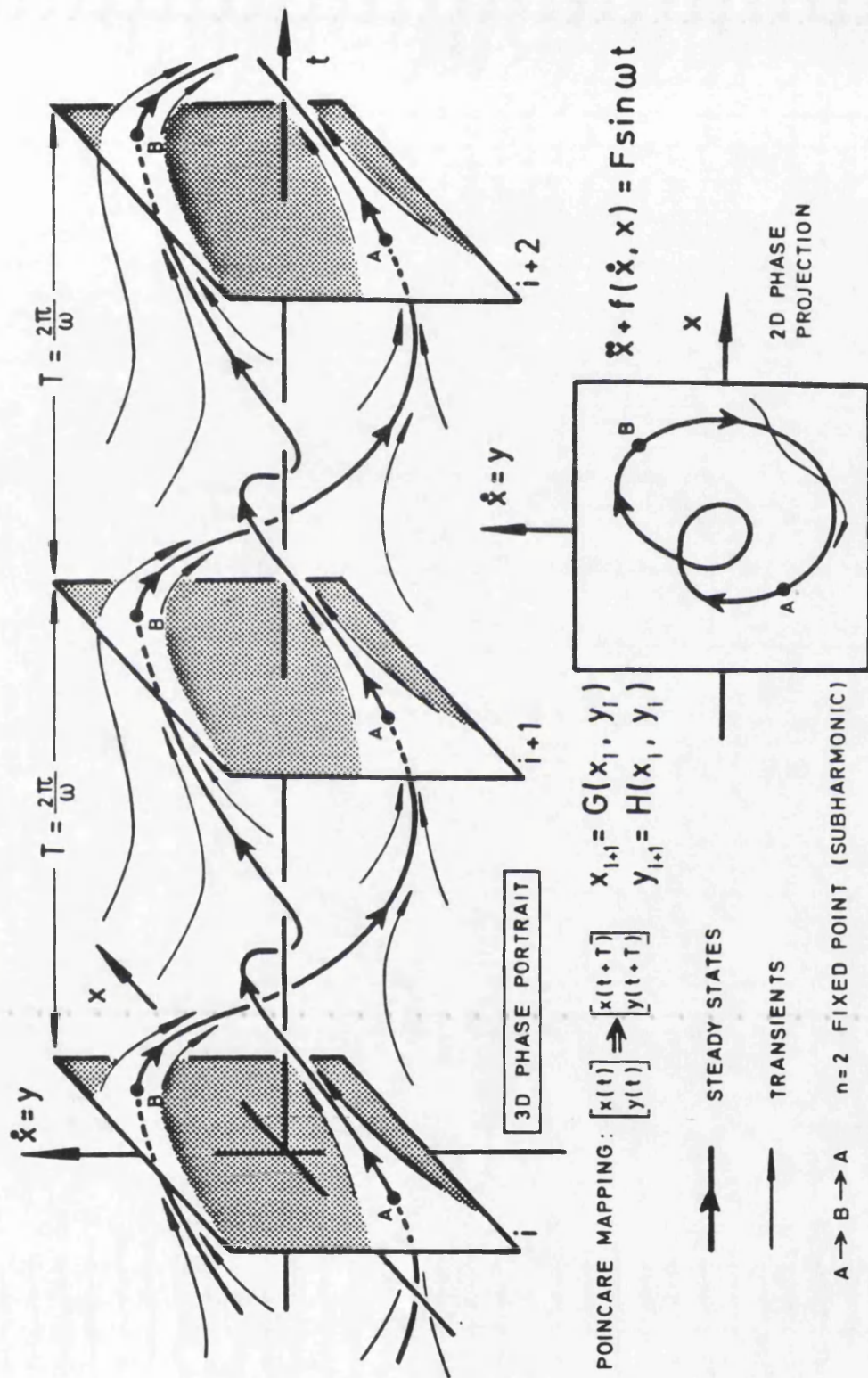
$$\begin{aligned}P_2 &= TP_1 = T^2P_0 \\ P_3 &= TP_2 = T^3P_0\end{aligned}\tag{2.11}$$

etc. We can also write the inverse mapping, $P_0 = T^{-1}P_1 = T^{-2}P_2$, etc. If a solution $x(t)$, $y(t)$ is a fundamental harmonic with the period L of the forcing, then the point P_0 is a fixed point of the mapping T . If, alternatively we have a subharmonic of order n ($=2,3,\dots$) with a minimum period of nL , the steady state mapping points

P_0, P_1, \dots, P_{n-1} are called periodic points. They are in fact all fixed points of the n^{th} iterate, T^n , of the mapping T . By studying just the mapping T of the (x, y) onto itself serves to determine the basins of attraction of our original continuous differential equation. Any initial point in the basin of a particular attractor, steps, under repeated iterations of the mapping T , to that particular attractor that is located in the interior of that basin. Numerical techniques, which obtain these basins of attraction typically include *grid of starts*, *cell-to-cell mapping* or *invariant manifold analysis* (Thompson, 1989).

As shall be discussed in subsequent chapters, basins and basin boundaries, like their attractors, change and bifurcate as system parameters are varied. It has recently been shown that in many nonlinear systems basin boundaries are *fractal*, which has fundamental implications for the behaviour of dynamical systems. This is because small changes in the initial conditions or other system parameters can lead to uncertainties in the outcome of the system. This leads to unpredictability in such systems (Grebogi et al, 1983, 1985, 1986).

Figure 2.1 Three-dimensional phase portrait of a forced mechanical oscillator, showing two-dimensional phase projection and Poincaré mapping.



STROBOSCOPIC POINCARÉ SECTIONS FOR FORCED OSCILLATORS

Figure 2.2 Stability transitions in the complex plane for flows and maps.

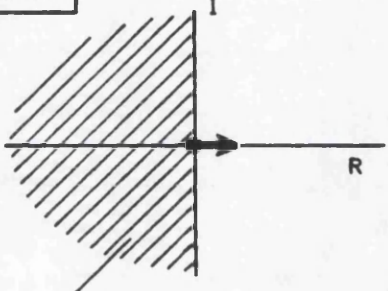
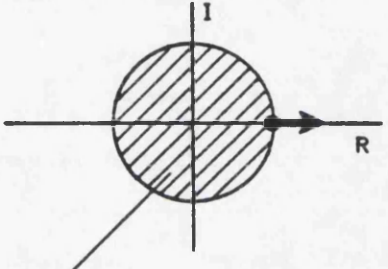
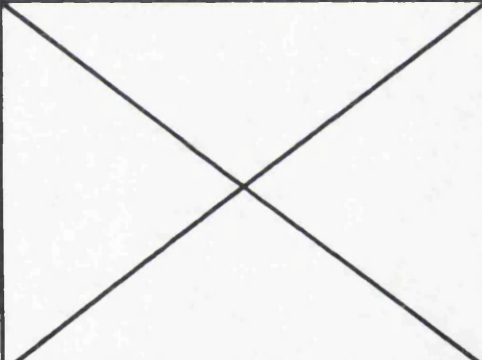
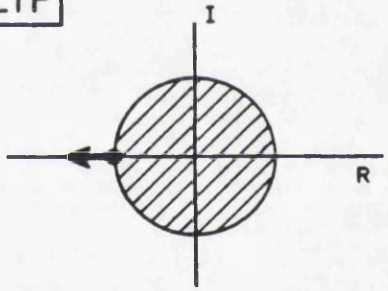
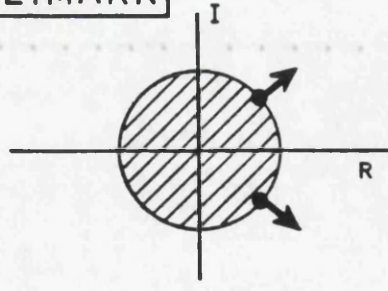
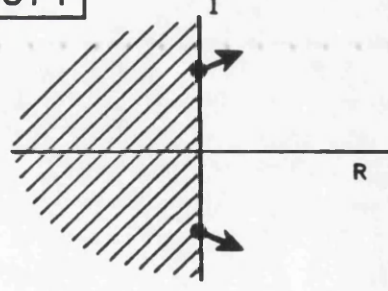
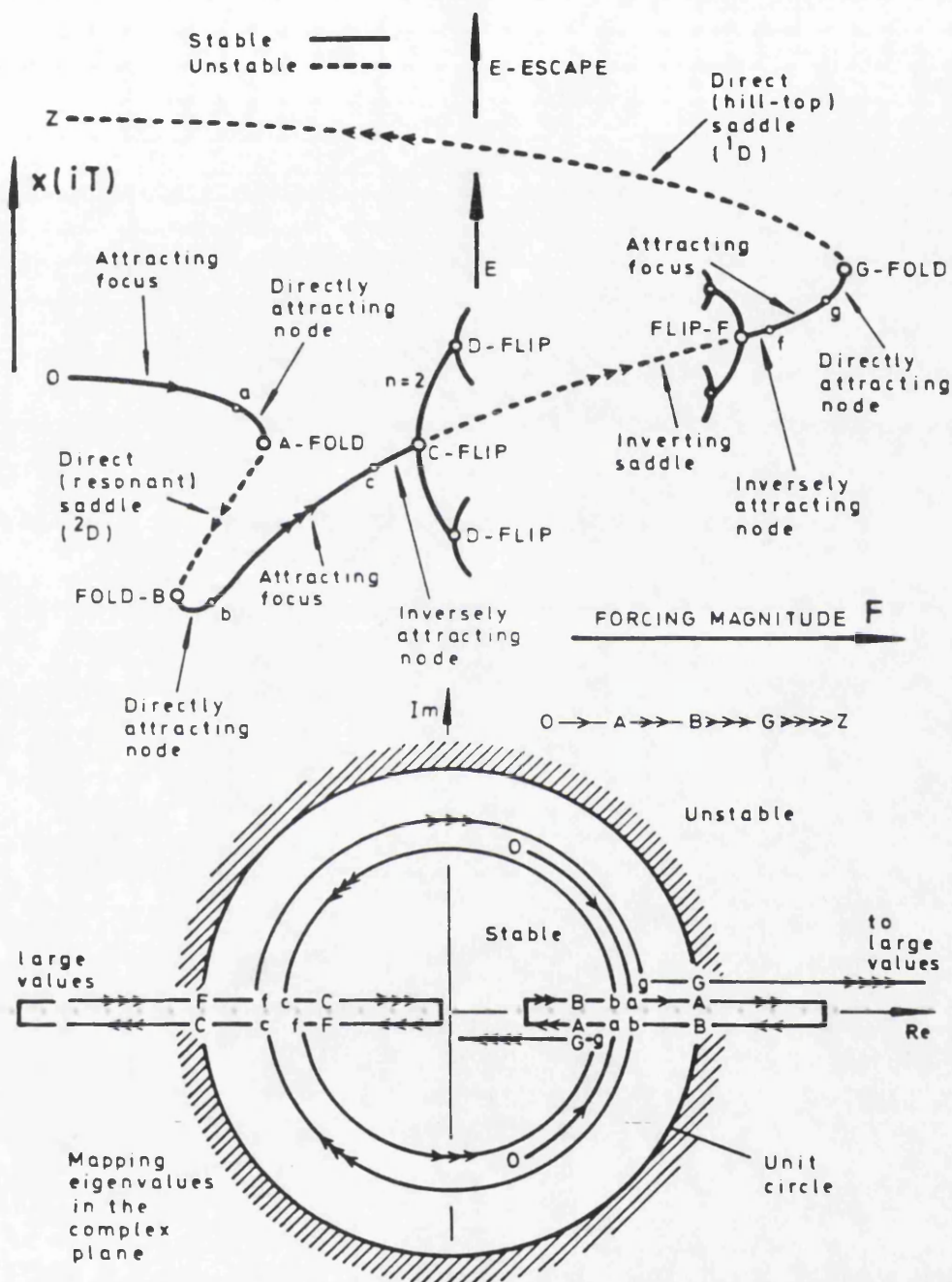
STABILITY TRANSITIONS IN THE COMPLEX PLANE	
LOSS OF STABILITY OF AN EQUILIBRIUM STATE	LOSS OF STABILITY OF A CYCLE
FOLD  Stable half-plane	CYCLIC FOLD  Stable unit disk
	FLIP 
	NEIMARK 
HOPF 	POINCARÉ CHARACTERISTIC MULTIPLIERS
LIAPUNOV CHARACTERISTIC EXPONENTS	

Figure 2.3 (a) Schematic sketch of the response curves at constant ω and constant β , showing the opposing flip cascades (b) the behaviour of the mapping eigenvalues in the complex plane.

SCHEMATIC FUNDAMENTAL ($n=1$) SOLUTION: ESCAPE EQUATION

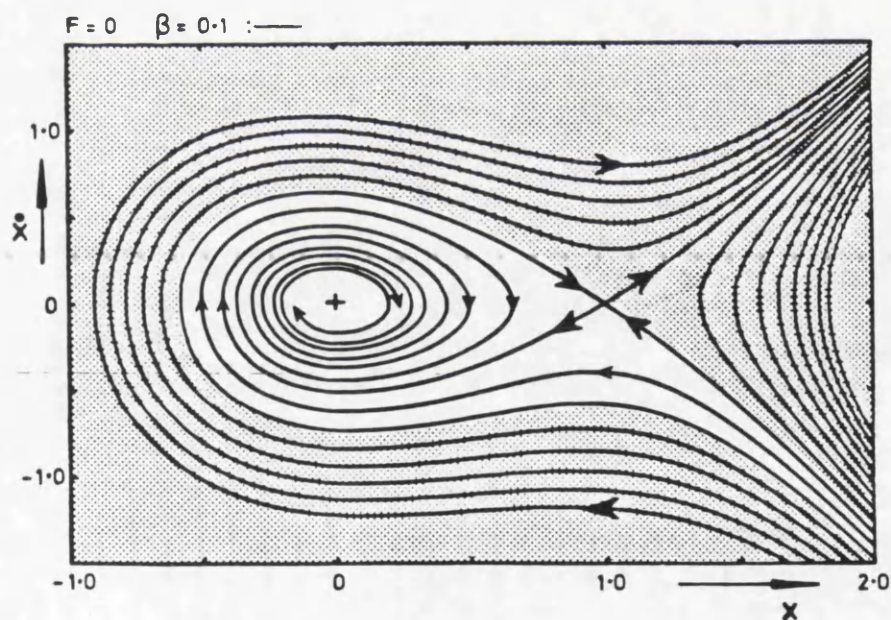
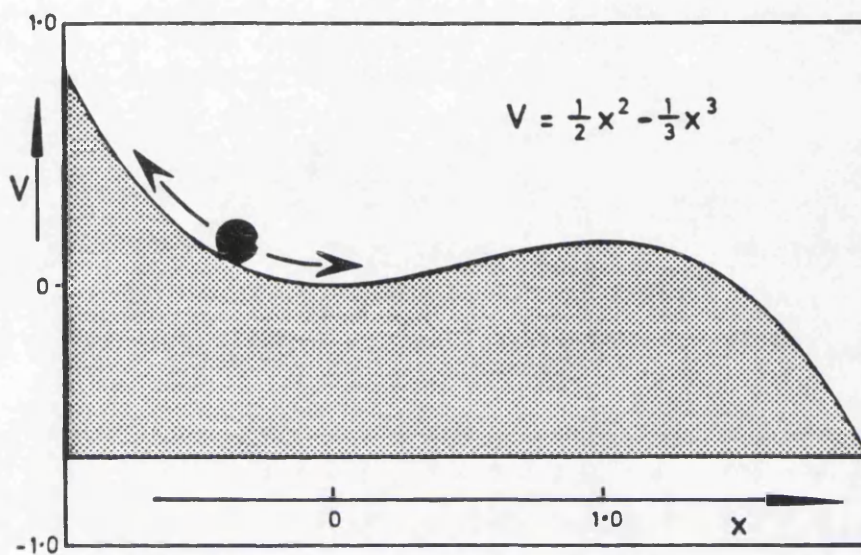


AT CONSTANT β AND ω THE PRODUCT OF THE EIGENVALUES IS CONSTANT

Figure 2.4 Two-dimensional phase portrait of the undriven autonomous system.

ESCAPE FROM A POTENTIAL WELL

$$\ddot{x} + \beta \dot{x} + x - x^2 = F \sin \omega t$$



CHAPTER 3: INTEGRITY MEASURES AND BASIN EROSION

3.1 Introduction

In this chapter we firstly consider how the basin of attraction is affected by the appearance of a homoclinic tangency (predicted by the method of Melnikov). In order to illustrate this, we shall consider the erosion of the basin of attraction of the main sequence of attractors from the fundamental state $F=x=y=0$ to the final blue sky event, at $F=F^X$, whether it be a simple cyclic fold or a boundary crisis.

Secondly the nature (smooth/fractal) of the basin of attraction will be considered and escape from a simple cyclic fold will be used to illustrate that, if the invariant manifolds of a saddle cycle have already homoclinically tangled at some value F^T , they must "detangle" before any saddle-node bifurcation that invokes this saddle cycle. In addition we emphasize that for a saddle node bifurcation the area of the absolute basin of attraction remains finite, within a specified window, at the escape value, F^X . This area will then drop to zero when the relevant attractor loses its stability catastrophically at the final bifurcation, which results in the inevitable jump to failure.

Thirdly we shall consider the transient escape behaviour. This is important because systems are not always subjected to constant forcing for long periods. This is especially true in the field of marine and naval technology where offshore structures are often subjected to a steady train of waves for relatively short periods of time, making the short term response of considerable significance. Transient basin diagrams (Pezeshki and Dowell, 1987), may be used to show how the transient basins of the attractor at infinity change as a system parameter is varied both before and after the blue sky catastrophe. Long transient behaviour is common after a saddle-node fold as examined by Van Damme & Valkering (1987).

Finally we shall consider how, if the local stability of an attractor under small-but-finite disturbances is to be examined, numerous factors other than the size and nature (smooth/fractal) of its basin of attraction must be investigated. These include how an attractor would respond to impact loading, noise, etc. We consider the sensitivity of an attractor subjected to impact loading, together with an alternative criterion of local integrity based on a suitably defined minimum distance from the attractor to the basin boundary.

3.2 Transient basins and integrity measures

In studying transient times we must acknowledge the fact that a system does not usually reach an attractor in finite time. We must therefore introduce a suitably defined neighbourhood of the attractor. For a point attractor in a Poincaré section an obvious neighbourhood would be a small disc centred on the attractor.

In this chapter we are only concerned with transients, from a local window of starts, that lead to escape from a potential well with x tending to infinity; that is to say the transients leading to the *attractor at infinity*. As our criterion of nearness to this we specify $x > 20$, based on the experience that for our equation a computer usually crashes due to overflow shortly after x passes 20.

We can therefore define a transient basin, \mathcal{A}_τ , as the set of all starting points that reach $x=20$ in $t < \tau$. It is also convenient to define the constraint basin, \mathcal{C}_τ , as the set of all points that reach $x=20$ in $t > \tau$ (or not at all). The transient boundary, \mathcal{B}_τ , between these two areas is then defined as the set of all points that reach $x=20$ in precisely time τ . The normally defined, *absolute* basin of attraction is clearly \mathcal{A}_∞ , obtained by letting τ tend to infinity.

We are not particularly concerned here with the fate of the constrained, non-escaping

trajectories. Most will be attracted to a well defined attractor (or one of a pair of attractors, in the region of hysteresis) lying on the main sequence of stable attractors (harmonic, subharmonic, and chaotic) originating from the equilibrium state $F=x=y=0$ under slowly incremented F . A small number may however be attracted to the large number of unexplored but highly localized competing attractors that are invariably encountered in problems of this type, examples being the S^3 and S^6 subharmonics associated with the saddle-node cascade scenarios (Thompson, 1989).

To quantify the erosion of the basin of constraint we introduce three measures which might serve to assess the engineering integrity of the main attractor.

The first concerns the area of C_τ within a prescribed window. Using a grid of N starts, we write the proportion that fall within C_τ as G_τ . We shall in fact measure τ in number of forcing cycles, m , and then write the proportion as G_m . This *global integrity measure* (GIM) is, conveniently, independent of the finite attractors onto which the constrained motions settle. Focusing on a given point attractor within C_∞ a useful deterministic measure of its integrity would seem to be the minimum distance, L_τ , in the (x,y) Poincaré section, from the attractor to the transient basin boundary B_τ . This gives us our second *local integrity measure* (LIM), L_m , written again in terms of forcing cycles.

Our third measure, based on the concept that a mechanical oscillator might be subjected to an impulse, in which it could be thought to experience an instantaneous step change in velocity, involves the minimum distance in the direction of $+y$ or $-y$. The minimum distance in the Poincaré section from the point attractor to the boundary B_τ in the direction of positive y is written as I^+ , and in the direction of $-y$ as I^- . With either a positive or negative sense, we thus have the *impulsive integrity measure* (IIM) denoted by I_m .

A fourth, *stochastic integrity measure* (SIM) can be defined in terms of the mean escape time when the attractor is subjected to white noise of prescribed intensity. This is investigated in detail in chapter 4.

3.3 Numerical simulations

The transient basin diagrams (Figures 3.3-3.7) were obtained by performing a fourth-order Runge Kutta numerical algorithm on equation (1). Here 100 by 100 initial conditions were chosen in the form of a grid and integrations were continued until either the escaping criterion was satisfied (arbitrarily chosen as $x > 20$), or the maximum allowable number of forcing periods was reached. For obvious reasons of computational economy, the allowable number was here taken as $m=16$. All the times to escape were stored with their corresponding initial conditions, and transient basin diagrams were plotted by assigning a different shade to assigned transient intervals. Global integrity curves, $G_m(F, \omega, \beta)$ versus F , can also be drawn from the stored data.

3.4 Choice of frequencies

In order to understand how a homoclinic tangency would affect the size of a basin of attraction several values of frequency, ω , involving different routes to escape from the $F=x=y=0$ fundamental state, were chosen and compared. The values of ω were chosen from a consideration of Figures 3.1a and 3.1b. These bifurcation diagrams were obtained by plotting curves, in (F, ω) space for fixed $\beta (=0.1)$, at which a homoclinic tangency, a period-doubling flip and a saddle-node fold bifurcation occur (Thompson, 1989).

The equation of the Melnikov homoclinic tangency line was obtained by applying the method of Melnikov (Thompson, Bishop and Leung, 1987). The condition for a homoclinic tangency between the stable and unstable manifolds of the saddle cycle close to the $x=1$ hilltop was found to be :

$$F^M = \frac{\beta \sinh(\pi\omega)}{5\pi\omega^2} \quad (3.1)$$

This is of course only an approximation to the true homoclinic tangency, F^T , and gives misleading results at large F and ω as we shall see. For this reason we have sketched a dashed line in Figure 3.1a on which we expect the actual homoclinic tangency to occur. The fold and flip bifurcation lines were obtained by using a bifurcation following routine, the flip being the first period-double from the fundamental $n=1$ to a subharmonic $n=2$ attractor. The right hand insert of Figure 3.1b shows four typical traces of the steady state responses at constant ω with F plotted against the stroboscopically sampled x .

The values of ω were chosen as follows; $\omega=3.4$ at which there exists an $n=1$ periodic attractor from the $F=0$ fundamental state all the way to the final saddle-node blue sky event: $\omega=2.4$ at which there also exists an $n=1$ periodic attractor until the final escape, however in this case a homoclinic tangency occurs at some value $F^T(\approx F^M)$: $\omega=1.0$ and 0.85 are similar in that in both cases there exists an $n=1$ periodic attractor (during which there is homoclinic tangency) which has a period doubling cascade leading to a boundary crisis; however at the latter there exists a hysteresis fold before the homoclinic tangency: $\omega=0.65$, where there exists an $n=1$ fundamental steady state in which escape occurs at a simple fold (in addition there coexists an $n=1$ periodic attractor with a period doubling cascade leading to a chaotic attractor).

3.5 Erosion of the basin of attraction

3.5.1 Results for $\omega=3.4$

The first case considered was that of $\omega=3.4$. Here there exists a monotonic trace of fundamental ($n=1$) harmonic oscillations originating at $F=x=y=0$ and terminating in a simple cyclic fold at $F^X \approx 8.11$. For the sake of this presentation it will be useful to assume that if trajectories do not escape within the maximum allowable time (16 forcing cycles) they will remain constrained, and hence that the \mathcal{B}_{16} basin boundary represents the absolute boundary between the attractor at infinity and the period-one attractor ($\mathcal{B}_{16} \approx \mathcal{B}_\infty$), and \mathcal{C}_{16} represents the corresponding absolute basin of attraction ($\mathcal{C}_{16} \approx \mathcal{C}_\infty$).

The erosion of the \mathcal{C}_{16} basin can be seen quantitatively in Figure 3.2. The proportion of initial conditions constrained decreases in a smooth manner from $F=0$ to $F=8.0$: none are constrained at $F=9.0$ as there only exists the attractor at infinity.

No homoclinic tangency was expected to occur on the basis of the Melnikov analysis (see Figure 3.1) and thus it was expected that the basin of attraction would remain smooth throughout. Indeed, as can be seen from Figure 3.3 (transient basin diagrams for $\omega=3.4$), although the \mathcal{C}_{16} basin changes in size, position and shape as F is gradually increased from $F=0$ to $F=F^X$, it seems to remain smooth. It is also important to discuss the behaviour of the transient boundaries and their corresponding transient basins. As can be seen in Figure 3.3 each different shade represents the basin of attraction for a particular transient-length interval. It must be pointed out however that the range of initial conditions were chosen such that the overall behaviour could be observed, and at the same time enough detail preserved for the purpose of this study. As can be seen each basin seems to be smooth and

once again as the value of the forcing amplitude is gradually increased the basins change in size. However unlike the C_{16} basin which vanished after F^X (≈ 8.11) the other transient basins still exist. This is perhaps most clearly illustrated by looking at the C_4 basin. At $F=8.0$ the C_4 basin is reminiscent of the C_{16} basin at lower values of F . However as F is increased to 9.0 the C_{16} basin has disappeared whereas the C_4 basin still exists in approximately the place where the C_{16} basin had resided. This can be explained by the fact that a saddle-node bifurcation is followed by long transients in the region of the extinguished basin (Van Damme and Valkeering, 1987). It must also be pointed out that this phenomenon seems not only to take place at the saddle-node bifurcation, but also when part of the C_{16} basin is eroded; here also the eroded region generates orbits with long escape times (see Figure 3.3, $F=6.0$ to 7.0). This is indeed what we would expect from the continuity of dynamical behaviour.

The sizes of the transient basins may be seen quantitatively in Figure 3.2. Each curve represents the proportion of initial conditions being constrained, G_m , for m cycles (as denoted by the specimen diagram). For low values of forcing most initial conditions are constrained within one cycle. This is partly due to the fact that all the simulations were started at phase $\phi=180^\circ$ (by replacing F by $-F$ as previously mentioned). This implies that the system is being first pushed into the potential well, tending initially to constrain the system. As one might expect, as the forcing increases a little, a greater number are constrained; as is indeed the case when practically all the initial conditions are constrained for one cycle at $F=7.0$. The proportion constrained for two cycles initially rises then falls. Here we must point out that this is true for the window of initial conditions considered and might not have been the case if a different range was chosen. From the transient basin diagrams of Figure 3 it can be seen that there is a considerable shift in the C_2 basin and this

may account for the rise and fall of G_2 . The erosion of the C_4 basin seems to follow closely the trend of the C_{16} basin. However the G_4 integrity curve, clearly illustrates there still exists the C_4 basin for $F > F^X$. It can also be seen that the G_8 , and G_{16} curves almost lie on top of one another, implying that the proportion escaping between 8 and 16 cycles is relatively small. This reinforces the view that $G_{16} \approx G_\infty$.

3.5.2 Results for $\omega=2.4$

The effect of a homoclinic tangency on the erosion of the basin of attraction will be considered for the case of $\omega=2.4$. Here a direct comparison can be made with the previous case of $\omega=3.4$, as the routes to escape were identical (i.e. an $n=1$ periodic attractor with escape from a simple fold); however here a homoclinic tangency was expected to occur (see Figure 3.1) at $F^M \approx 1.05$, well before the final blue sky event at $F^X \approx 4.13$. Indeed, as expected, the C_{16} basin of attraction seems to remain smooth below the Melnikov criterion (Figure 3.4). However once the forcing amplitude exceeds the Melnikov limit, the basins become more complex with whisker-like projections indicating fractal behaviour (McDonald, Grebogi, Ott & Yorke, 1985; Moon and Li, 1985; Moon, 1987). This smooth-fractal basin boundary metamorphosis is due to the homoclinic tangling of the stable and unstable manifolds of the saddle periodic orbit on the basin boundary as Grebogi et al (1987) have indicated. As the forcing amplitude is further increased the basin becomes more complex in appearance as new tongue-like projections gradually erode more and more of the basin. However at $F=3.5$, although a considerable part of the basin has been eroded, the structure seems to become less complex in appearance. In fact at $F=4.0$ the basin seems once again to have become smooth. This is indeed the case as we shall examine

later. Indeed, it is clear from centre manifold considerations that on approaching a saddle-node bifurcation there can be no homoclinic tangling of the saddle manifolds. So at this ω value we must have a detangling before F^X i.e. a smooth-fractal metamorphosis as well as a fractal-smooth metamorphosis must take place.

The effect of the homoclinic tangency on the size of the basin of attraction can be seen quantitatively in Figure 2. For $F < F^T (\approx F^M)$ as was seen previously, a small gradual shrinkage of the C_{16} basin takes place. After the homoclinic tangency, the catchment region is very rapidly eroded, reducing by about 50% from $F=1.0$ to $F=2.0$. Furthermore, it is important to note that for $F < F^M$ the G_{16} , G_8 , and G_4 integrity curves seem to be coincident, while after the tangency they diverge appreciably. This, as will be more clearly illustrated later on, is due to the emergence of the finger-like projections and chaotic transients.

3.5.3 Results for $\omega=1.0$ and $\omega=0.85$

In this study $\omega=1.0$ and 0.85 were also considered and the transient basin diagrams are reproduced in Figures 3.5 and 3.6. In both cases an $n=1$ periodic attractor terminates in a Feigenbaum cascade, leading to a chaotic folding band attractor, and finally escape is triggered by the blue sky disappearance of the attractor at $F^X \approx 0.220$ and $F^X \approx 0.109$ respectively. The essential difference is that the latter exhibits a region of hysteresis. In addition to seeing how the homoclinic tangency will affect the size of the basin of attraction in this particular problem, the effect of a hysteresis loop will be examined as well as the transient behaviour after a chaotic blue sky event.

It is perhaps in the case of $\omega=0.85$, from all the cases studied, that the effect of the homoclinic tangency is most clearly illustrated. This is due to the fact that there seems to

be only a small movement in the position of the basin of attraction and hence the overall picture is more easily examined. As seen in the $\omega=0.85$ global integrity curves there is little or no change in the size of the transient basins before the homoclinic tangle. It is important to point out that, apart from the G_1 curve, the curves here seem to be almost coincident implying that a relatively small proportion escape between 2-16 cycles. However as the Melnikov criterion is exceeded there is a dramatic erosion in the C_{16} basin with a not so dramatic erosion of the C_8 , C_4 , and C_2 basins, as indicated by the divergence of the integrity curves. This can be clearly observed in the transient basin diagrams of Figure 3.6; for $F=0.0$ to 0.07 there is little or no change in the transient basins; however at $F=0.07$ a small finger-like projection appears, where upon at $F=0.08$ there is a sudden shrinking of the C_{16} basin and a complete change in the appearance of the picture. It can also be noted that although the total areas of the C_8 , C_4 , and C_2 basins decrease after the homoclinic tangency, there is an increase in the proportion of initial conditions which escape between 2-4, 4-8, and 8-16 cycles. Correspondingly the C_{16} basin will depart more significantly from the C_∞ basin. This is due to the development of the homoclinic tangle and the emergence of the finger-like projections, causing chaotic transients as an escape sequence maps from one finger to the next. A detailed illustration of this mapping sequence is given by Thompson (1989). As F is increased further towards F^x , there is a continuation of the erosion, although not so dramatic, of the C_{16} , C_8 , C_4 , C_2 , and C_1 basins. At F^x (≈ 0.109) there is a boundary crisis of the chaotic attractor and an instantaneous destruction of the C_∞ basin of attraction, analogous to that elucidated by Abraham and Stewart (1986) for the Van der Pol oscillator. However there still exist well defined transient basins after the blue sky catastrophe, and on the macroscopic level there seems to be no immediate change in the C_{16} , C_8 , C_4 , C_2 , and C_1 basins. Even at $F=0.110$ there exists a C_{16} basin, as seen in the transient basin diagrams

as well as in the integrity curve, G_{16} . This transient chaotic dynamical behaviour beyond a crisis, as described by Gwinn and Westervelt (1986), is associated with the folding in the phase space. At a crisis the collision with an accessible saddle (here D^6 as demonstrated by Thompson (1989)) destroys the C^∞ basin, although the "metastable" basin remains. The scaling of chaotic transients beyond the boundary crisis is shown, to follow the exponential laws of Grebogi et al (1986).

The effect of the hysteresis can be considered by comparing the results for $\omega=0.85$ with those of $\omega=1.0$ where the diagrams (Figures 3.5 and 3.6) and integrity curves are seen to behave in a similar fashion. Looking more closely at the region of hysteresis for $\omega=0.85$, there exists a resonant hysteresis in the region between two cyclic folds at $F \approx 0.05$ and $F \approx 0.07$; F^M is at 0.065. By inspecting the $\omega=0.85$ integrity curves there seems to be little or no change in the size of the C_{16} basin (or in any of the basins) during the region of hysteresis. This implies that the total non-escaping region is unaffected by the hysteresis loop, although the size of the individual basins for the two coexisting $n=1$ attractors is continually changing over this range. This is because the size and nature of the total absolute non-escaping boundary is determined by the inset of the hilltop saddle while the separatrix between the two coexisting $n=1$ basins is determined by the resonant saddle between the coexisting attractors.

3.5.4 Results for $\omega=0.65$

The final value chosen was $\omega=0.65$. Here there exists a monotonic trace of the fundamental ($n=1$) solution terminating in escape from a simple cyclic fold at F^A . Also present though not encountered in a natural loading sequence from $F=x=y=0$ is an $n=1$ periodic attractor

created by the saddle-node at F^B which period doubles to a chaotic attractor. The range of F in which the fold B, flip C and crisis occur is extremely small and coincides roughly with the Melnikov value $F^M=0.057$. For the transient basin diagrams of $\omega=0.65$ (Figure 3.7) it can be seen that as the forcing amplitude increases from $F=0$, the C_{16} basin increases in size as well as remaining smooth until the Melnikov criterion is reached. Here a fractal appearance is observed although it is not entirely clear. As F is further increased, the gradual erosion of the C_{16} basin is, unlike the cases of $\omega=0.85$ and 1.0 , by one finger like projection, which grows in size encircling the C_{16} basin. In fact the C_{16} basin seems once again to have become smooth, and its erosion is in a similar fashion to that at $\omega=2.4$: and in both cases termination of the $n=1$ attractor is by escape from a simple fold, with long transients after the saddle node bifurcation. Here, however the saddle of the saddle-node bifurcation is not the hilltop cycle, but the resonant saddle created at fold B.

The integrity curves confirm these deductions. After a slight increase in the size of the C_{16} basin, it starts to diminish after F^M . However the G_{16} , G_8 , and G_4 curves seem to remain roughly coincident indicating the lack of the finger-like projections. This suggests that the basin of the attraction might have become smooth before the final escape. The sequence of events at $\omega=0.65$ is indeed not entirely clear, and warrants further study.

3.6 Tangling and detangling

The effect of the homoclinic tangency on the erosion of a basin of attraction has already been considered. It is also useful to know whether a basin is smooth or fractal. The analytical method of Melnikov can be used to predict, at which forcing amplitude, F^M , the appearance of a homoclinic tangency, F^T , takes place. However, as discussed in section 3.5.2, there

exists a value of forcing at which the basin seems to have become smooth, indicating a "detangling" of the stable and unstable manifolds. In this section we show that this is indeed the case; critical forcing amplitudes, in which a smooth-fractal metamorphosis or a fractal-smooth metamorphosis takes place can be defined.

As an illustration of this we shall consider the case of $\omega=2.4$ where escape occurs from a simple fold at $F^X \approx 4.13$. Here the homoclinic tangency between the stable and unstable manifolds predicted by Melnikov's method was at $F^M \approx 1.05$. We deduce that at some forcing amplitude F^D , such that $F^T < F^D < F^X$ there must be a detangling of the stable and unstable manifolds before the final saddle-node bifurcation. This must happen as just before a saddle-node bifurcation there can be no crossing of the stable and unstable manifolds as is apparent from the centre manifold concepts (Thompson and Stewart, 1986). Figure 3.8 shows the stable and unstable manifolds of the hill-top saddle cycle superimposed on the basin of attraction for several forcing amplitudes. These were obtained by plotting orbits in the Poincaré sections at phase $\phi=180^\circ$ backwards in time from a ladder of starts along the ingoing eigenvector of the saddle and forward in time from the outgoing eigenvector. The accuracy of the Melnikov criterion can be seen in Figures 3.8a and 3.8b. For $F < F^M$ the stable and unstable manifolds do not cross; as the forcing just exceeds the Melnikov criterion ($F > F^M$) the stable manifold develops a finger which crosses the unstable manifold as shown in Figure 3.8b. As F is further increased, as seen in Figure 3.4 of the transient basin diagrams for $\omega=2.4$, it can be seen that the basin becomes more complex in character until about $F=4.0$ where the basin seems to have become smooth once again. Indeed this is confirmed in Figures 3.8c and 3.8d where at $F=3.5$ there is a tangling of the manifolds and at $F=3.8$ there is not. These results imply that approximately for $0 < F < 1.1$ no tangling occurs (hence the basin is smooth), for $1.1 < F < 3.65$ a tangling occurs and the basin is

therefore fractal, and for $3.65 < F < F^X$ there is again no tangling of the manifolds (smooth basin). Figure 3.1a shows a sketched line of the form that we expect the actual homoclinic tangency line to follow. The two crosses are values at which actual homoclinic tangencies were found.

Although this would be the simplest case in which this type of behaviour would occur for our particular oscillator, for other frequencies with complicated routes to escape, this scenario would be common. For example in the case of $\omega=0.85$, in which $F^M \approx 0.065$ and escape occurs from a chaotic blue sky event at $F^X \approx 0.109$, there exists a reversed period doubling cascade and chaos at $F \approx 0.70$ leading to a second "escape" from a simple fold, and thus a "detangling" should once again occur. It can thus be deduced that although the Melnikov criterion, F^M , quite accurately predicts the homoclinic tangency, F^T , over a certain range of parameter values, there exists another critical value, F^D , in which a detangling takes place as shown in figure 3.1a. Relevant recent work on fractal distributions and the stable manifold has been done by Vazquez et al (1987).

3.7 Local integrity of the attractor

If one was to consider the "local stability" (but not infinitesimally local) of a particular attractor, numerous factors other than the size (section 3.5) and the nature (section 3.6) of its basin of attraction must be considered. These include the response to impact loading and external noise, position of the attractor within the basin, etc. Some specific examples are as follows: (a) often a system settled on a particular attractor may experience a nearly instantaneous change of velocity due to an impact loading, perhaps causing the system to jump from one attractor to another; (b) basins of attraction are often finely divided, as in

the case of a fractal, where the separation between the attractor and the boundary can be small; the addition of external noise can easily push trajectories across these boundaries as in the case discussed by Gwinn and Westervelt (1986), of noise induced intermittency of a driven damped pendulum; (c) often real dynamical systems do not settle down to "true" periodic, subharmonic or chaotic motion; this can be due to a small random disturbance (noise) of either mechanical, thermal or electrical origin. In the case of a period one oscillation the long term behaviour, viewed through Poincaré sections, would then appear to be a scatter of dots around this "attractor". This is discussed in more detail in chapter 4.

3.7.1 Local integrity measure

In this section we shall consider how close the attractor is to the basin boundary, the distance in the stroboscopically sampled ($t=2i\pi/\omega$ $i=1,2,3 \dots$) Poincaré section (x,y) offering one measure of the engineering robustness of the attractor. Local integrity curves, similar to those of the global integrity are drawn, as shown in Figure 3.9, in this case the abscissa being the distance, L_m , to the transient basin boundary, \mathcal{B}_m . They were obtained by measuring the minimum distance from the attractor to the \mathcal{B}_m basin boundary using the stored data and the co-ordinates of the main sequence attractor. From previous considerations (section 3.3) it will be useful in our discussion to speak as if $L_{16} \approx L_\infty$ i.e. the distance from the attractor to the absolute basin boundary.

On first glance the results seem to be in close agreement with the global integrity curves. As one would expect the shrinking of the basin generates a reduction in the distance between the attractor and the basin boundary. This can be clearly seen in the case of $\omega=3.4$ where as F is increased the basin shrinks resulting in the reduction of the local integrity measure,

L_{16} , between the $n=1$ periodic attractor and the \mathcal{B}_{16} basin boundary. This is also the trend for the L_8 , L_4 , L_2 , and L_1 local integrity curves.

The effect of a homoclinic tangency on the local integrity measure can be seen in the case for $\omega=2.4$. Here the homoclinic tangency causes a dramatic erosion of the \mathcal{C}_{16} basin resulting in the reduction of L_{16} . Once again (as in the case of the global integrity curves), the not so dramatic reduction of L_8 , L_4 , L_2 , and L_1 after the homoclinic tangency gives rise to a divergence of the local integrity curves.

However for $\omega=1.0$ although initially there is no erosion of the basin of attraction as seen from the global integrity curves before the Melnikov criterion, there is a continuous reduction in all the local integrity curves. This implies that as F is gradually increased, successive attractors become nearer to the various transient basin boundaries. In addition it can also be seen that the homoclinic tangency does not significantly change the trend of the local integrity curves as most of the erosion of the basin takes place outside the vicinity of the attractor. It must also be pointed out that unlike the previous cases of $\omega=3.4$ and 2.4 , where at a fixed forcing amplitude the L_{16} , L_8 , L_4 , L_2 , and L_1 integrity measures were significantly different, here they seem to be coincident; this implies that in the vicinity of the attractor the distance between \mathcal{B}_{16} and the other transient basin boundaries is extremely small, and hence a slight change in the starting conditions could mean either no escape or escape within one forcing cycle. This can be clearly seen in Figure 3.5.

In the case of $\omega=0.85$, the results are as expected; however there is a sudden reduction in the local integrity just after $F \approx 0.07$. A closer inspection reveals that this is not due to the sudden erosion of the basin, but due to the hysteresis jump in which the new attractor is considerably closer to the basin boundary. The attractor chosen in this study is always the one that would be observed physically under the slow increase of F from zero (incidentally

only $n=1$ and $n=2$ attractors were considered for the F values examined: in the latter case the minimum of two distances was chosen). Once again the homoclinic tangency does not seem to cause a dramatic change in the local integrity curves. For $\omega=0.65$, the size of the basin of attraction grows as F increases for $F < F^M$, and drops dramatically for $F > F^M$. This also seems to be the trend of the local integrity curves.

3.7.2 Impact loading

In this section we will consider the response of a system subjected to an instantaneous change of velocity. Figures 3.10 and 3.11 show how large a positive or negative impact, measured here by Δy , would be needed before the various transient basin boundaries are reached. These were obtained by performing a line of starts in the $(+/-) \hat{x}$ direction from the relevant attractor. The required impact, I_m , to cause the attractor to cross the \mathcal{B}_m basin could thus be obtained.

For $\omega=3.4$ and fixed F , the required impact to cross successive transient basin boundaries increases; the I_1^+ and I_1^- are not shown as the impact required to cross \mathcal{B}_1 were larger than those considered in this study. As F is increased the required impact (both positive and negative) to cause the attractor to escape reduces in magnitude (where $I_{16} \approx I_\infty$); this is due to the erosion of the basin of attraction as seen in Figure 3.2. Just before the saddle-node fold, the value of I_m^\pm , is relatively small; indicating that the attractor is extremely sensitive at such loading.

In the case of $\omega=2.4$ the effect of a homoclinic tangency on the impulsive integrity measure was found to follow a similar trend to those of the local and global integrity curves. After the tangency there is a sudden reduction in I_{16}^\pm as well as a not so dramatic reduction of

Γ_8^+ , Γ_4^+ , Γ_2^+ , and Γ_1^+ as indicated by the divergence of the impulsive integrity curves. This is due to the appearance of the whisker-like projections making the attractor more sensitive to such loading.

For $\omega=1.0$ as F is increased successive attractors get closer and closer to the "northern" basin boundary. This has the effect of reducing the required positive impact to reach failure but increasing the magnitude of negative impact required to cause the stable attractor to escape. However as the Melnikov criterion is exceeded, as well as there being a sudden reduction in the size of the basins, there is a dramatic reduction of Γ_m but hardly any change in Γ_m^+ . This can be explained by the fact that most of the erosion takes place in the negative \dot{x} direction from the attractor.

For $\omega=0.85$, a hysteresis jump causes the relevant attractor to become much closer to the basin boundary; resulting in the positive impact to cause failure to be significantly reduced with a slight increase in the negative impact required. The curves seem to be unaffected by the homoclinic tangency ($F^T=0.065$). In fact there seems to be a critical value ($F\approx 0.08$) at which a sudden drop in Γ_m occurs, and it can thus be deduced that the erosion of the basin by the finger-like projections has taken place in the vicinity of the attractor and caused it to be considerably more sensitive to such an impact. These observations also hold for the case of $\omega=0.65$.

3.8 Summary of the chapter

In this chapter we have investigated how on the macroscopic level, the size and nature (smooth/fractal) of basins of attraction change as a system parameter is varied, namely as

the forcing amplitude of our driven oscillator is increased from the $F=0$ fundamental state to and beyond a bifurcation or a crisis. Our main conclusions are as follows:

- (a) The erosion of the basin of attraction until its final destruction at F^X , exhibits no discontinuous jump in size except at the final bifurcation. However the appearance of a homoclinic tangency of the stable and unstable manifolds resulting in a fractal basin dramatically enhances the erosion of the basin. In addition, the erosion of both smooth and fractal basins resulted in a region (residue) of long transient orbits; trajectories initialized in the vicinity of the attractor, but not in its basin, would remain near it for long periods.
- (b) The size of the basin at F^X , although finite, was extremely small for damping level $\beta=0.1$. Beyond a crisis this basin was destroyed and long transient behaviour was observed. At a saddle-node bifurcation the transient behaviour was roughly periodic, and at a boundary crisis the transients were chaotic. However on the macroscopic level, no significant change in the transient basins was observed just before and beyond a crisis, where there exists a "metastable" basin of attraction.
- (c) A region of hysteresis does not effect the erosion of the total non-escaping basin of attraction, although the size of the competing basins are changing continuously (Thompson and Ueda, 1989).
- (d) The Melnikov criterion, F^M , accurately predicted the appearance of a homoclinic tangency, F^T , for a certain range of frequencies. However for forcing levels above this criterion a "detangling" at F^D was observed. Hence a more realistic representation of regimes where the basin was smooth or fractal could be defined as seen in Figure 3.1a.
- (e) Global integrity curves are a useful tool when investigating basin boundary metamorphoses: however it must be pointed out that the size of a basin is just one of the

numerous factors which must be considered when analysing the finite stability of an attractor. For example whether the basin is smooth or fractal, and the position of the attractor within the basin must be considered.

Impulsive and local integrity curves can be used, together with global integrity curves to give an indication of the local stability of an attractor, and hence an estimation of its response to external forces such as an impact loading:

(1) A hysteresis jump or rapid movement of the attractor as a system parameter is varied, can cause the attractor to move much closer to the boundary without any change in the size of the basin; this can result in a greatly reduced impulsive and local integrity measure.

(2) Attractors lying in fractal basins of attraction can be extremely sensitive to impact loading or noise which can cause a trajectory to move from one attractor to another.

(3) On approaching a boundary crisis or a saddle-node fold, the attractor was extremely sensitive to impact loading as its basin of attraction was often very small. We should notice here, that, unlike the global integrity measure G^∞ , the local integrity measure, L^∞ , drops smoothly to zero at a saddle-node bifurcation.

Figure 3.1a Bifurcation diagram for $\beta=0.1$ showing the saddle-node fold G and flip C (first period-double from the fundamental $n=1$ solution) curves, as well as the Melnikov line in the (F, ω) control space. Also shown is a sketched line showing the form that we expect the actual homoclinic tangency line to follow. The vertical dashed lines indicate the frequency values examined in this report.

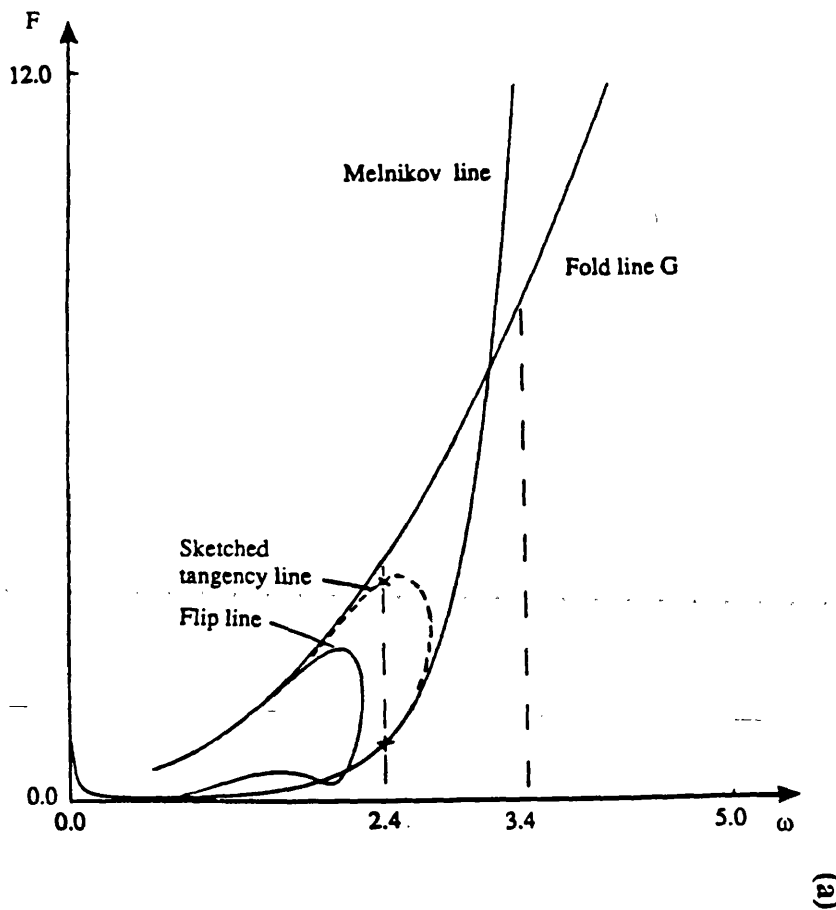
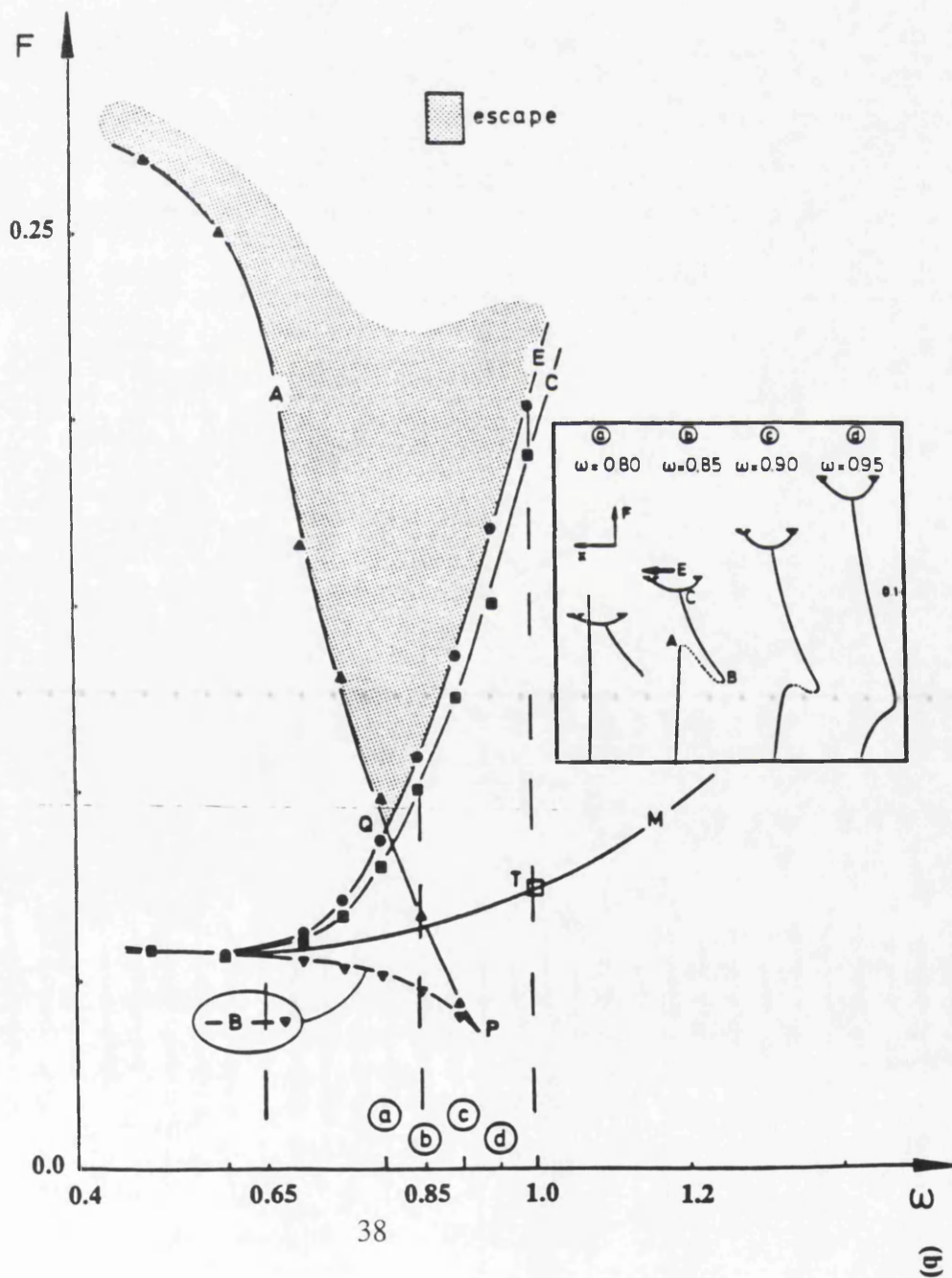


Figure 3.1b Blow-up of Figure 1a. Inset are four typical traces of the steady state responses at constant ω , with F plotted against x as sampled stroboscopically at phase $\phi=0$. The vertical dashed lines indicate the frequency values examined in this report.



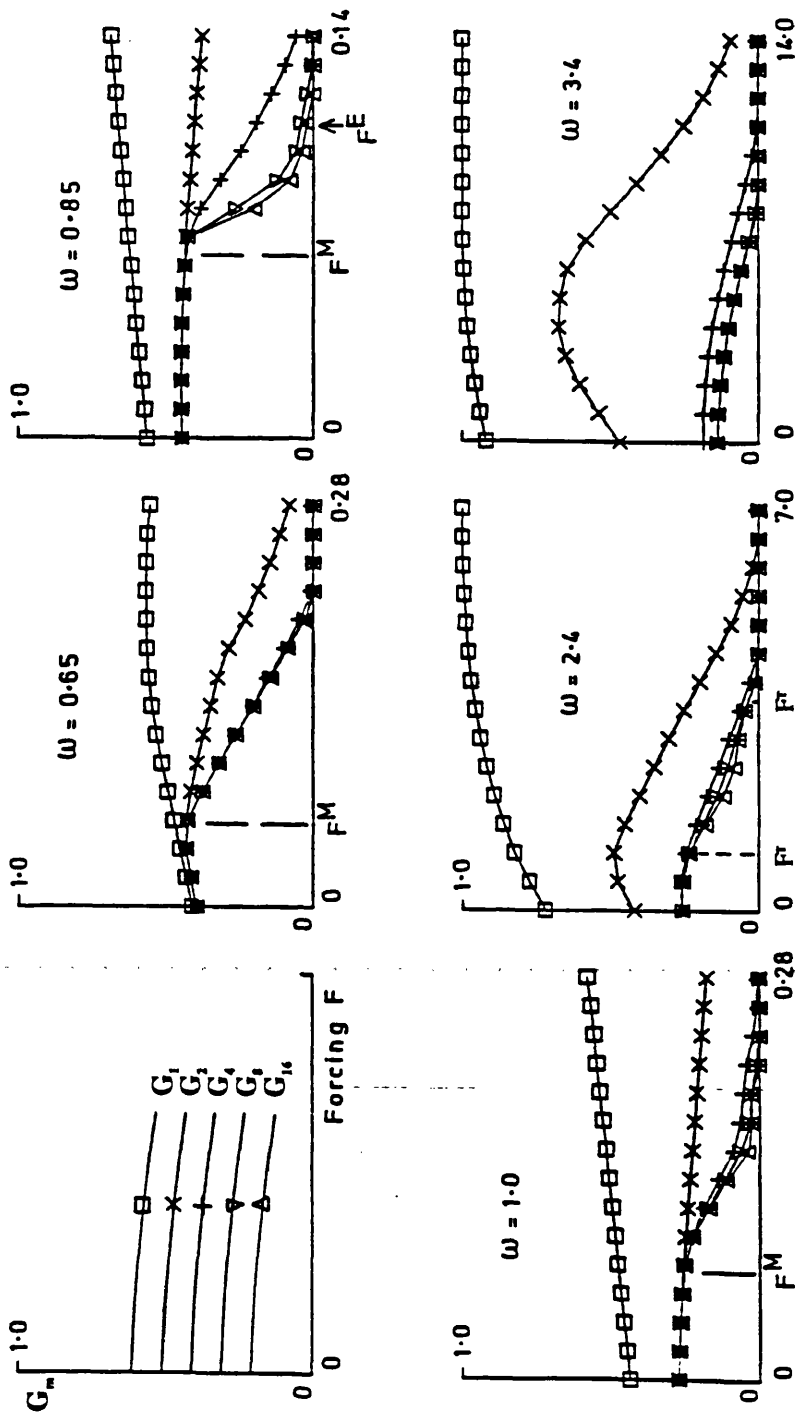


Figure 3.2 Global Integrity Measure curves for the given frequencies.

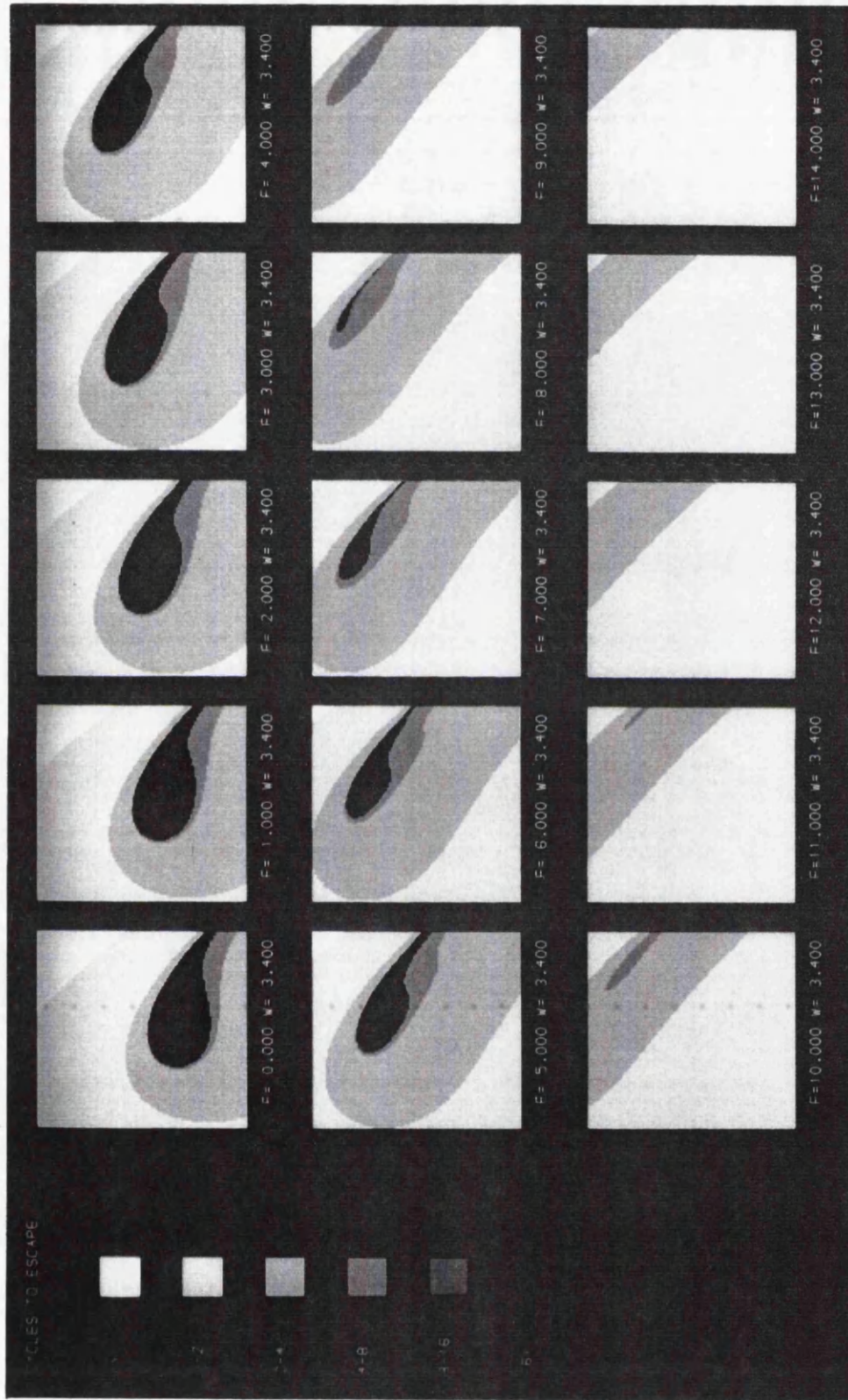


Figure 3.3

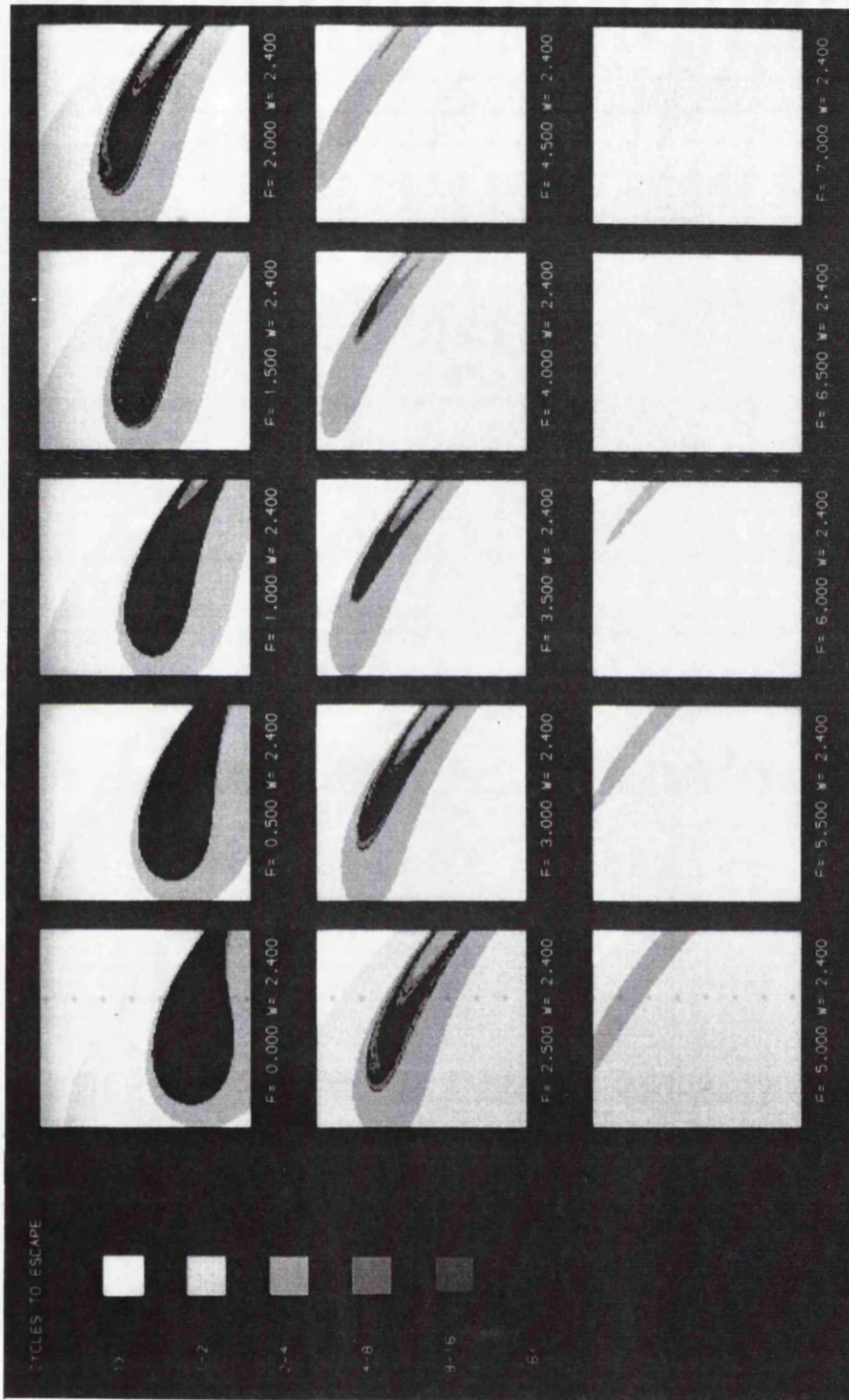


Figure 3.4

Figure 3.4 $\omega=2.4$ in the window: $-0.8 < x < 1.2$ $-1.5 < y < 3.0$

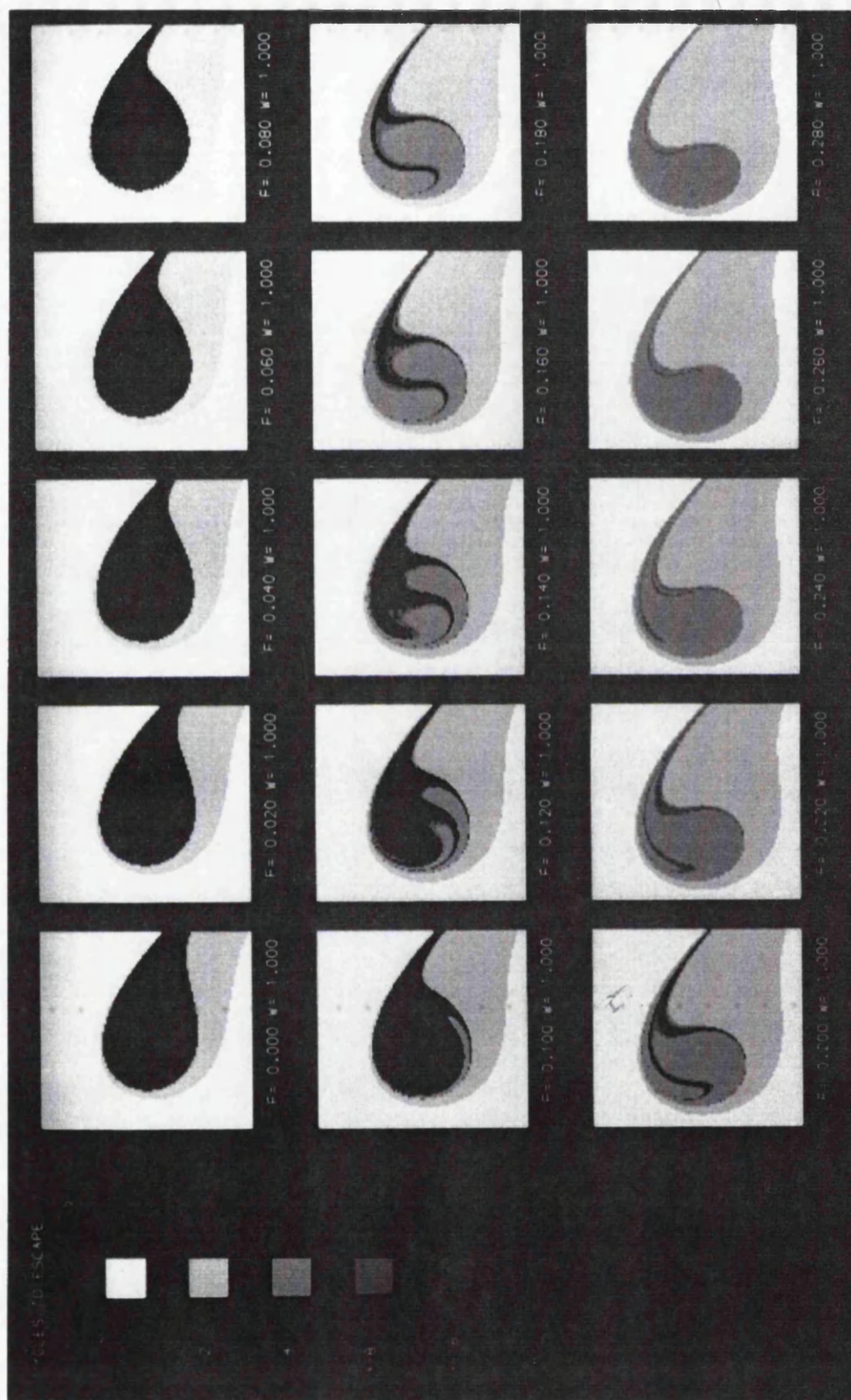


Figure 3.5

Figure 3.5 $\omega=1.0$ in the window: $-1.0 < x < 1.2$ $-1.5 < y < 1.5$



Figure 3.6

$\omega=0.85$ in the window: $-0.8 < x < 1.2$ $-1.0 < y < 1.0$

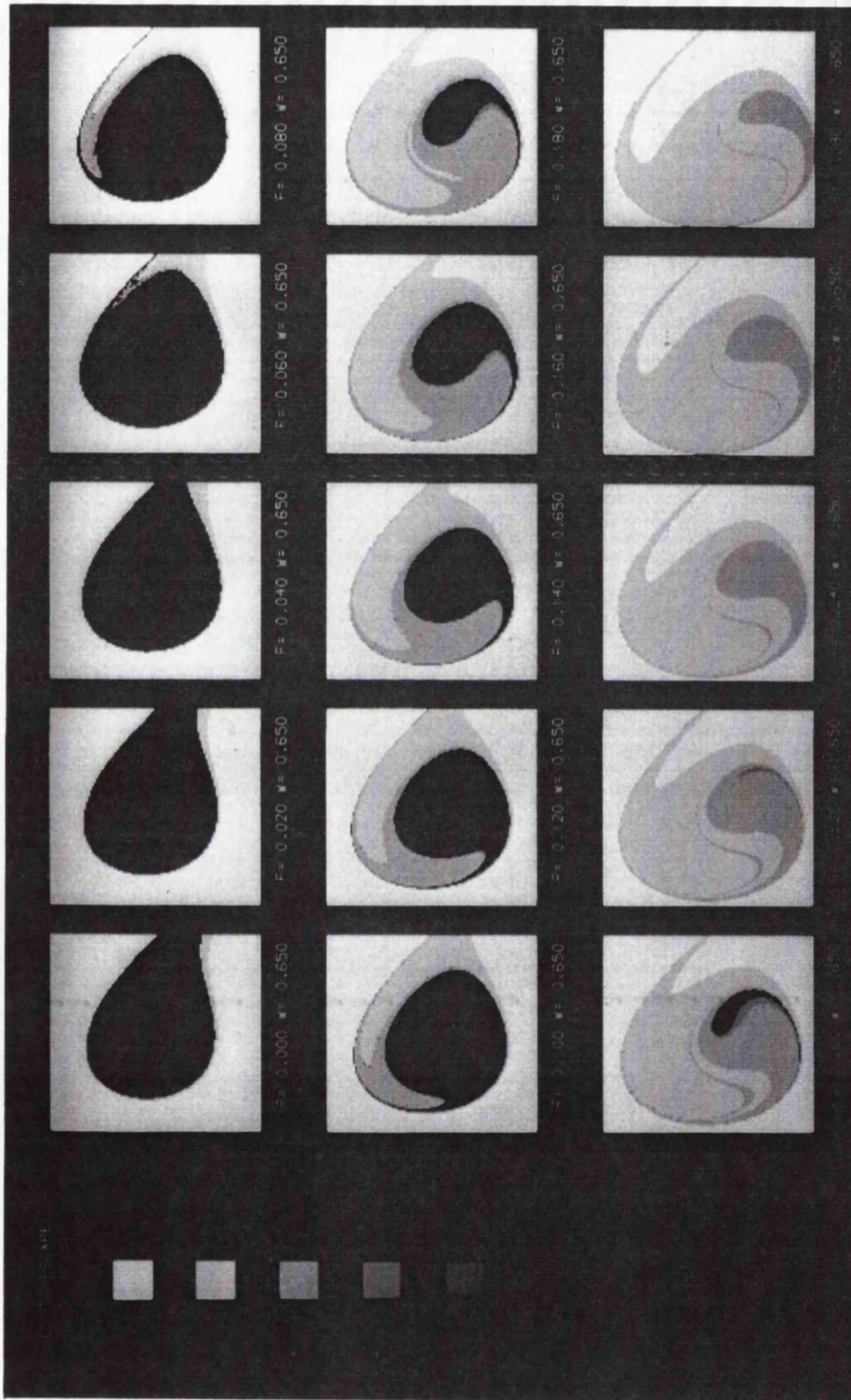


Figure 3.7

Figure 3.7 $\omega=0.65$ in the window: $-0.9 < x < 1.1$ $-1.2 < y < 1.0$

Figure 3.8a $F < F^T$ $F=1.0$ in the window $-1.0 < x < 1.5$ $-1.5 < y < 1.5$

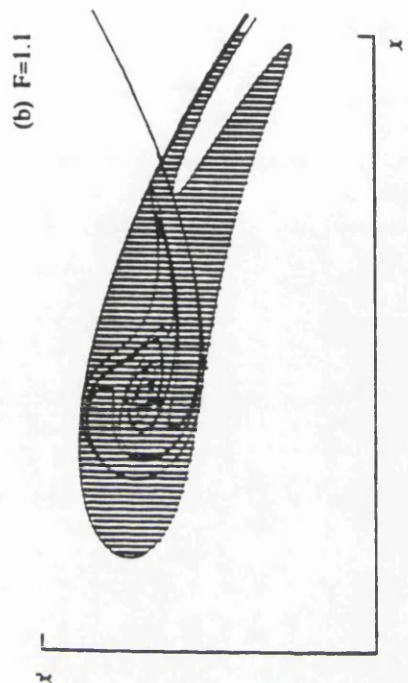
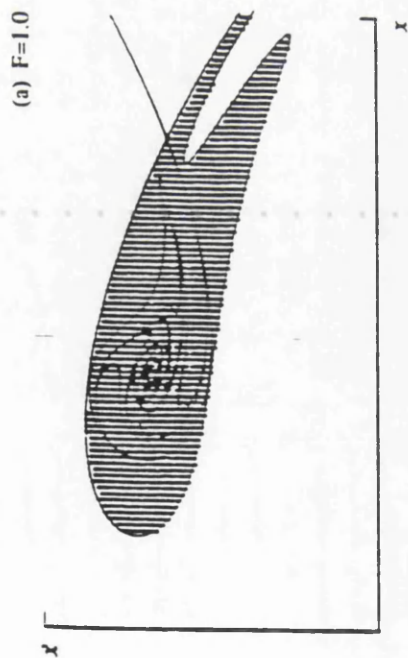


Figure 3.8b $F > F^T$ $F=1.1$

Figure 3.8c $F < F^D$ $F=3.5$ in the window $-0.2 < x < 1.3$ $0.5 < y < 2.5$

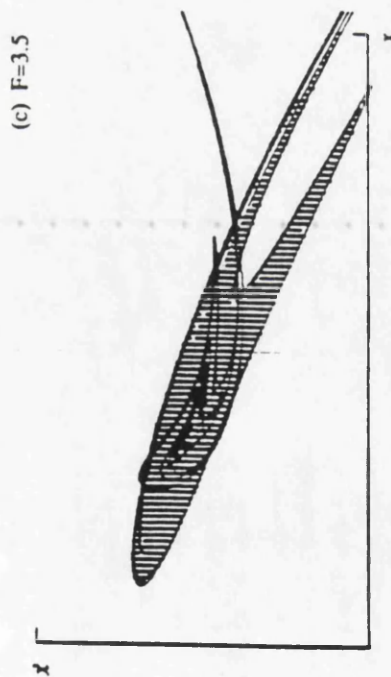


Figure 3.8d $F > F^D$ $F=3.8$

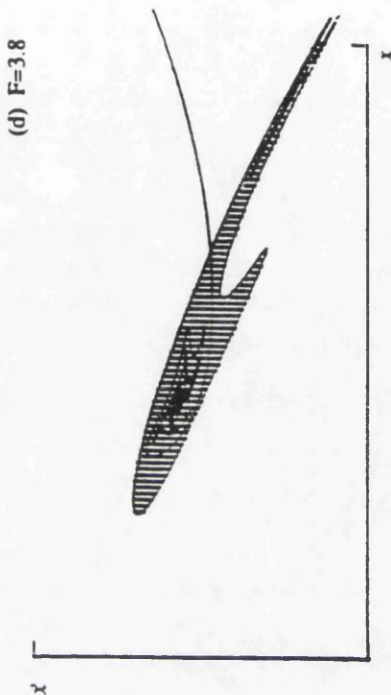


Figure 3.8 Tangling and detangling of the invariant manifold of the hill-top saddle cycle. (1) invariant manifold analysis (curved lines) and (2) grid of starts for the basin of attraction (dots forming vertical hatching). $\beta = 0.1$, $\phi = 180^\circ$, $\omega = 2.4$

Figure 3.9 Local Integrity Measure curves for the given frequencies.

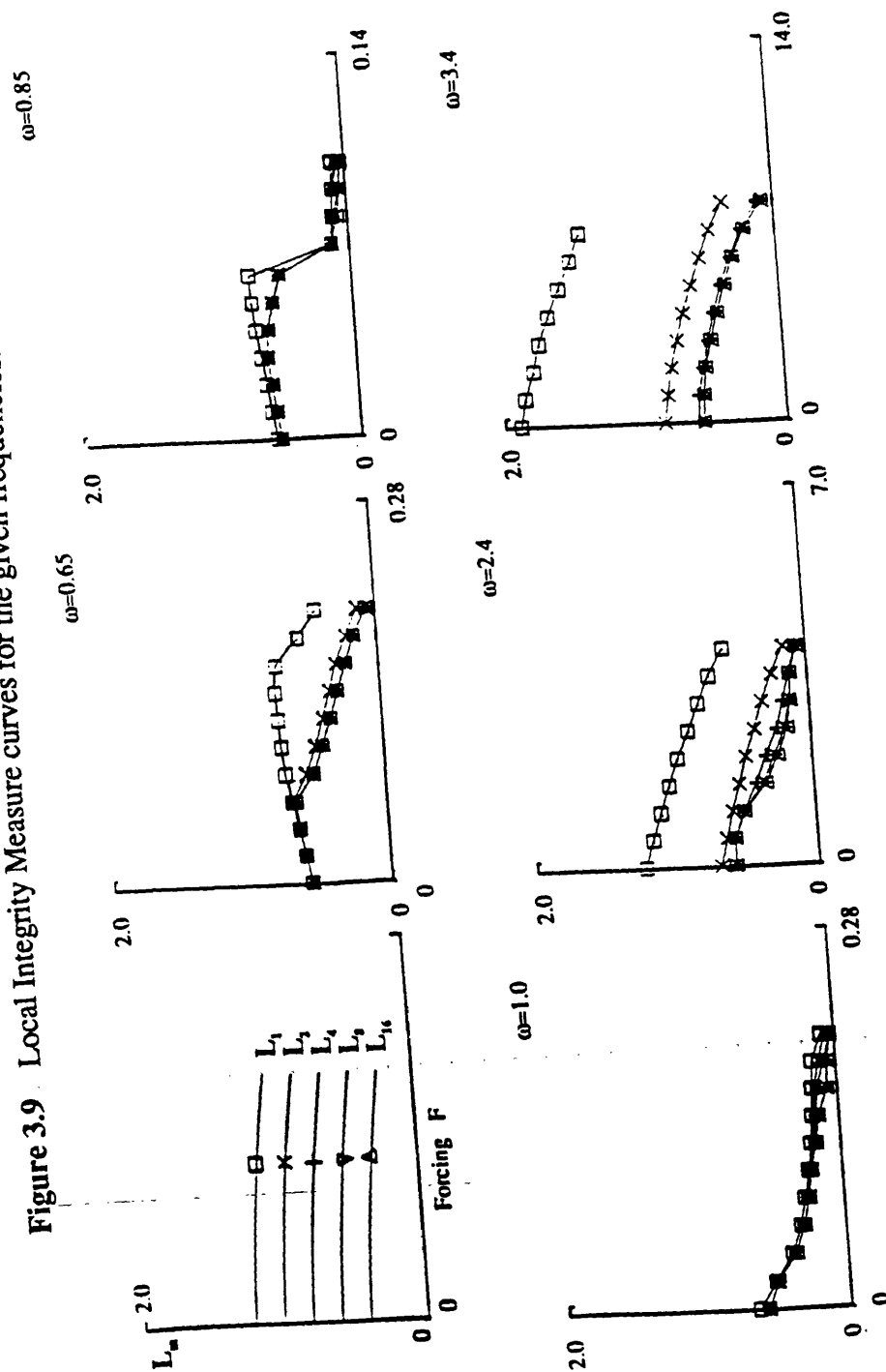


Figure 3.10 Impulsive Integrity Measure curves for the given frequencies (positive impact).

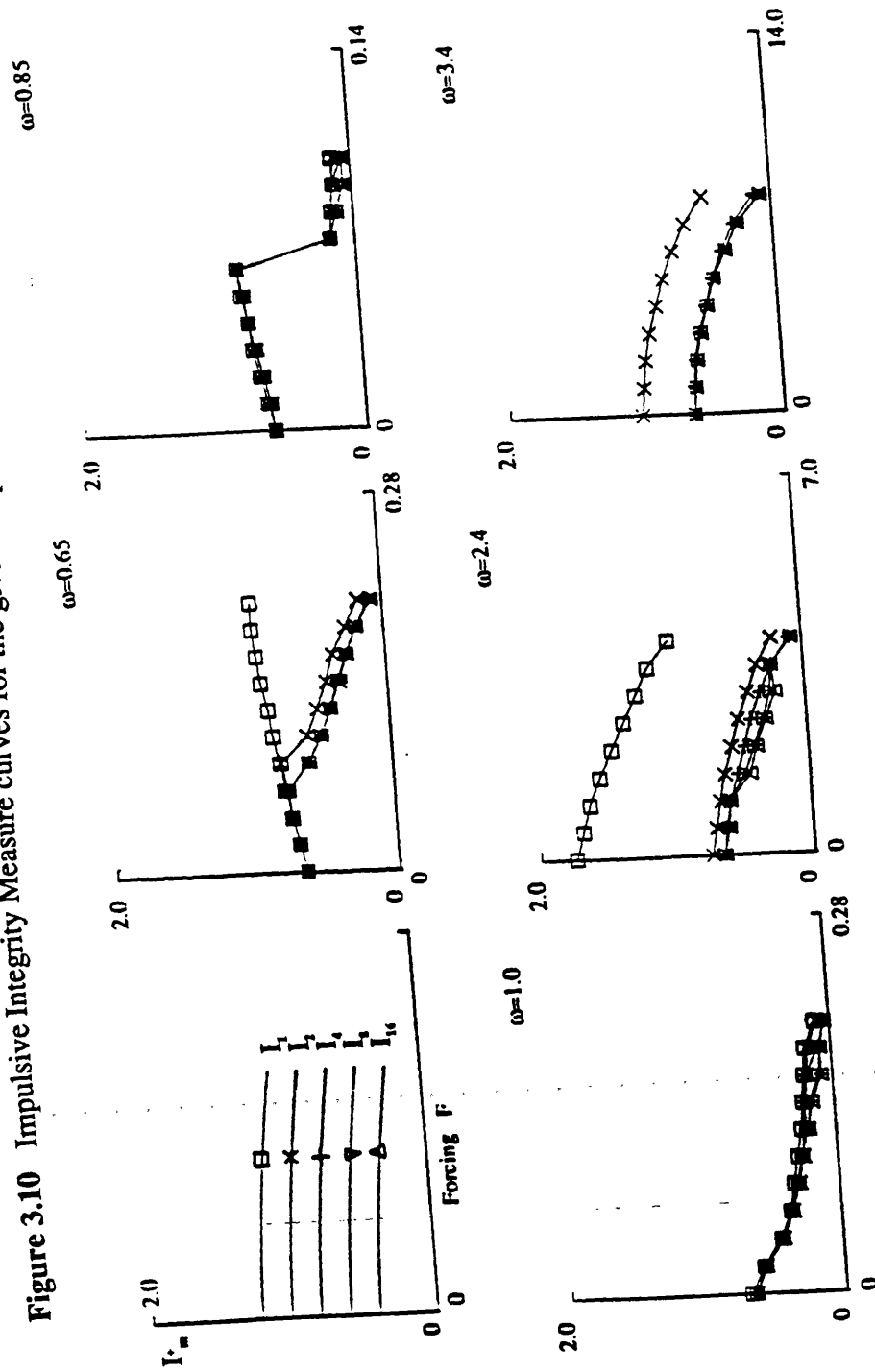
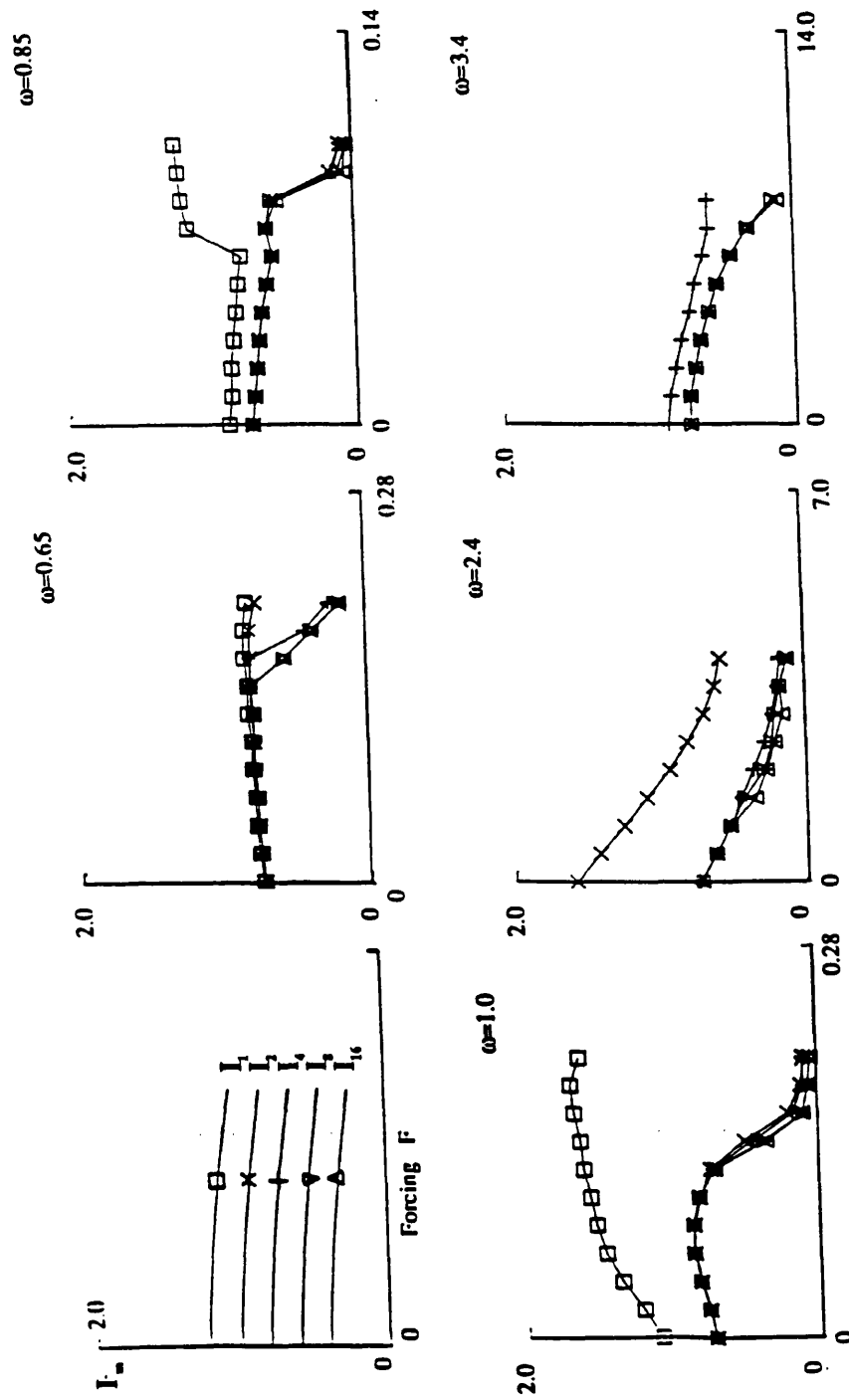


Figure 3.11 Impulsive Integrity Measure curves for the given frequencies (negative impact)



CHAPTER 4: STOCHASTIC ANALYSIS

In chapter 3 it was shown that basins of attraction can change dramatically in size, shape and position under small variations in parameter values. In this chapter we investigate the dynamical response of attractors subjected to external fluctuations (Moss & McClintock, 1989). The role of basins of attraction and the boundaries that separate them will also be considered, such that a correlation between the sensitivity of attractors to noise and their noise-free basins of attraction can be assessed.

We thus consider the mechanical oscillator, described by equation 3.1, with the additional excitation term such that

$$\ddot{x} + \beta\dot{x} + x - x^2 = F \sin \omega t + \xi(t) \quad (4.1)$$

where $\xi(t)$ is an optional noise term which is zero unless otherwise stated. We define $\dot{x} \equiv y$ and we focus attention throughout on phase, $\phi = 180^\circ, \beta = 0.1, \omega = 0.85$. The detailed response of this oscillator has been mapped out by Thompson (1989).

Firstly, the effect of external noise on a steady state attractor is investigated using a suitably defined stochastic integrity measure which will indicate for a given noise intensity the sensitivity of an attractor to such excitation. In the absence of noise the lifetimes of stable running modes of driven damped oscillators are infinite; however in any real physical system, external noise is present, and will eventually cause transitions between previously stable attractors. Although the input excitation and the output response are then not deterministic, the statistics of such dynamic response (or input) quantities can be simply converted into statistics on the sensitivity of an attractor to stochastic loading. Many engineering

problems experience the type of loading considered in this paper where mechanisms are governed by a vibrational environment (often by a sinusoidal forcing) but effected also by a noisy environment which can be mechanical, thermal or electrical in origin. By observing the stochastic integrity measure as a control parameter is varied the relative sensitivity of attractors for a given noise level may be seen. At a fixed control parameter the stochastic integrity measure may be used to determine at which noise intensities the attractor becomes appreciably sensitive to noise.

Secondly we shall assess the relationship between the response of the attractor to external fluctuations and its basin of attraction. Local, global and stochastic integrity measures may be used to indicate if such a correlation exists, and how they may be used in conjunction with one another to give an overall view of the robustness of the attractor. Figure 4.1 shows the basin of attractions and theirs coresponding attractors for $\omega=0.85$. Figures 4.2a and 4.2b show the local and global integrity curves as described in chapter 3.

4.1 Stochastic integrity measures

In this section we shall propose a way of determining the sensitivity of an attractor to external loading if $\xi(t) \neq 0$ in eqn (4.1). We shall consider the input excitation, $\xi(t)$, to be that of white noise with a prescribed intensity and with a Gaussian distribution, such that

$$\langle \xi(t)\xi(t') \rangle = 2D \delta(t - t') \quad (4.2)$$

$$\langle \xi(t) \rangle = 0$$

The reason for choosing Gaussian white noise, aside from all the analytical advantages and available literature, is that the Gaussian process has a great importance as a model for real physical processes. Many random processes in nature which play the role of excitation to vibratory systems are approximately Gaussian, and some are typically wide-band such as the pressure fluctuations on the surface of a rocket missile due to acoustically transmitted noise, or due to supersonic boundary layer turbulence (Crandall and Mark, 1963).

As the excitation in eqn (4.1) is random if $\xi(t) \neq 0$, we must consider the statistical behaviour of the response of the attractor to external noise for a large number of trials, N . One way of quantifying the sensitivity of an attractor to noise is the stochastic integrity measure S_m , defined as the proportion of trials that are constrained for time τ , and with τ measured in forcing cycles m ,

$$S_m = \lim_{N \rightarrow \infty} N_m / N \quad (4.3)$$

where N_m is the number of trials constrained for at least m forcing cycles in N trials. This measure is chosen for its comparability with the global and local integrity measures described earlier. An alternative way of describing the sensitivity of the attractor to external noise would be using the *mean escape time* and its standard deviation (which we shall show results for later on). Another approach would be to fit a Normal probability distribution response curve to the results data, (as the input excitation is Gaussian, we might hope that the response will also be approximately Gaussian). This probability distribution function would then

completely describe the response of the system to external loading (mean escape time, standard deviation and proportion constrained within m cycles) although it might prove ineffective for studying these quantities with any precision. The stochastic integrity measure as well as the mean escape time are easy to calculate and have analogues to well known engineering "fatigue/failure" problems. The problem considered in this paper does of course fall under the category of a "first passage problem" where escape can be considered as the failure criterion (Arecchi *et al*, 1984)

4.2 NUMERICAL SIMULATIONS

4.2.1 Stochastic integrity

After the system is settled on the noise-free attractor, and a few hundred cycles added to ensure that the motion is completely stable with no transients, noise is applied by adding a Gaussian random number to the right hand side of eqn (4.1), with zero mean and standard deviation σ , at the start of each Runge Kutta time-step. The time to escape was recorded and the process repeated ($N=300$) until we have built a well defined distribution of escape times. The noise intensity (strength), D , can be approximated by

$$\sigma^2 = 2D \Delta t \quad \text{as } \Delta t \rightarrow 0 \quad (4.4)$$

where Δt is the Runge Kutta time-step. In our case we chose $\Delta t = (1/40) \times$ (forcing period). Several smaller time-steps were tested with the same noise intensity, and approximately the same mean escape time was observed, indicating that for

the purpose of this study Δt was sufficiently small.

The stochastic integrity measure, for a given noise intensity D , could thus be calculated from eqn (4.3). Stochastic integrity curves of S_m versus forcing amplitude, indicating the relative sensitivity of successive attractors to a fixed noise intensity, D , could thus be drawn. Results showing the sensitivity of an attractor to different noise levels are also drawn by plotting stochastic integrity (and mean escape time) versus noise intensity. Upper bound limits of the noise intensity which would cause "failure" (in the engineering sense that "failure" occurs when a certain proportion of trials reach the failure criterion in a specified time) of an attractor could thus be determined.

4.2.2 Noise modelling

Given that we have already made deterministic escape-time studies in chapter 3 from a grid of starts in our basin investigations, it is perhaps worth enquiring how we could use this data to assess the pattern of mean escape times and stochastic integrity that we have just examined under *real* stochastic loading. We consider figures 4.1, 4.2a and 4.2b which summarise the relevant results found in chapter 3.

Suppose that under random noise fluctuations the stochastic phase portrait (in a two dimensional Poincaré section, say) has the rotationally symmetric probability function $p(r)$, where r is the distance from the attractor to a point in the Poincaré section. [Rotational symmetry is of course quite a heavy assumption, but in the present context might not be too drastic.] Imagined as a large number of required starting points, N , for our deterministic runs distributed over a large

area A we have,

$$\int_A p(r) dA = 1$$

$$\text{No. of required points within } \delta A = N p(r) \delta A$$

We want to make a series of *deterministic* runs from such a distribution of starts.

We use our previous fine grid of N points distributed uniformly over an area A so that

$$\text{No. of real grid points in } \delta A = N \delta A / A$$

To make this correspond to the required distribution we introduce the *weighting function* $W(r)$, such that

$$\text{No. of imagined points in } \delta A = N W(r) \delta A / A$$

We normalise $W(r)$ so that

$$\int_A W(r) dA = A$$

making the total number of imagined points also equal to N . Equating the required and imagined distributions we have

$$W(r) = A p(r)$$

Suppose a typical grid point, i , has escape time t_i , and radius r_i . Then the required mean escape time is

$$MEAN = (1/N) \sum t_i W(r_i) = (1/n) \sum t_i p(r_i)$$

where n is the number of real grid points per unit area.

Introducing for every grid point i an index Γ_i designated so that $\Gamma_i = 1$ if the trial is constrained for m forcing cycles and $\Gamma_i = 0$ if the trial escapes within m forcing cycles, we can define the stochastic integrity as

$$STOCHASTIC\ INTEGRITY = S_\tau = \sum \Gamma_i W(r_i) / \sum W(r_i)$$

As we have already considered the effect of real noise applied in a Gaussian form it would be reasonable to take a Gaussian form for the probability density function. So in terms of the *normal Gaussian* function

$$p(x) = \frac{\exp(-x^2/2\sigma^2)}{\sigma\sqrt{2\pi}}$$

we write

$$p(r) = p(x, y) = p(x)p(y) \text{ with } r^2 = x^2 + y^2 \quad \leftarrow$$

to give

$$p(r) = \frac{\exp(-r^2/2\sigma^2)}{2\pi\sigma^2}$$

with

$$\int_0^\infty p(r) 2\pi r dr = 1$$

4.3 Noise sensitivity of attractors

4.3.1 Varying Noise Intensity

In this section we consider the effect of noise on the main sequence of stable attractors which include period-one, subharmonic and chaotic attractors (Thompson and Stewart, 1986).

In the absence of noise the lifetimes of these attractors are infinite, but in noisy environments there is always a finite probability of escape within any time τ . Different attractors respond differently to the same noise levels and the same attractor can behave differently to varying noise levels. This is clearly seen in figure 4.3 where the *stochastic integrity measure* S_{16} is plotted versus noise intensity for two period-one attractors. In reality this type of variation occurs quite frequently, where noise levels on one particular attractor can change, due for example to a temperature change. In the noise-free environment with $D=0$, we have $S_{16}=1.0$. This is of course as expected, since all the trials are constrained with trajectories remaining perfectly on the attractor.

For $F=0.01$ the stochastic integrity remains at 1.0 for low noise levels, indicating that all the trials were constrained. This was indeed the case for $m=16$ but would not have been the case if m was infinitely large since $S_{\infty}=0$ and all the trials would escape. But as this paper is predominantly concerned with transient behaviour, which is more relevant to real situations, there is no real paradox here.

These results suggest that the attractor, at $F=0.01$, although changed in appearance remains relatively unaffected by low noise levels.

For $F=0.07$, the picture is quite different. As the noise level is slightly increased from $D=0$, the stochastic integrity reduces quite rapidly, indicating that a much

higher proportion of trials escape. These results imply that this attractor is much more sensitive to noise induced failure, as we would expect.

Viewed through Poincaré sections the sequence of events is as follows. In the noise-free environment the period-one attractor would be seen as a dot. The addition of a small amount of noise causes a broadening of the attractor, but remaining well within its basin for the finite times under consideration here. The increasing noise level greatly broadens the attractor asymmetrically along the direction for which attraction is weakest (in some cases producing a noise-broadened attractor which resembles a chaotic one, as shown later on). Techniques such as using the Liapunov exponents which can be used to distinguish between chaotic and periodic orbits are no longer as straight forward as in the noise-free deterministic limit (Crutchfield *et al*, 1982). The broadening of the attractor makes trajectories more susceptible to hopping into other basins, specifically the one of the attractor at infinity. This process is clearly enhanced by increasing the noise level as seen in fig 3 where the proportion of trials escaping increases with noise intensity. It is perhaps convenient to point out, that in the presence of noise, trajectories with certain initial conditions, are attracted towards the vicinity of the noise-free attractor and remain there for some time. We can speak of *noisy attractors*. It is important to point out, however, that the addition of noise will cause all trajectories to escape as time tends to infinity; but as we are considering only reasonably short transient behaviour the above term seems justified.

4.3.2 Comparison with analogue simulations

Our colleagues at Lancaster University (U.K.) have also made some *analogue* simulations of the escape from our metastable well in the case of strong sinusoidal forcing and weak additive noise (Dykman *et al*, 1989).

Their experimental procedure is as follows. The system is set on the attractor (noise-free) and allowed a few hundred orbits to ensure the motion is completely stable; then the noise is applied, and simultaneously, the data processor is triggered; a sweep of $x(t)$ is recorded; the time at which escape occurs is measured and stored in a separate memory block. The process repeats, again and again, until a well-defined distribution of escape times has been determined. As can be seen in Figure 4.4a the distributions consist of a series of separate maxima, reflecting the fact that escape is most likely to occur in a particular region of the orbit. Figure 4.4b shows a three-dimensional stochastic portrait of the escape process. Here a snap-shot of the probability distribution, $P(x, \dot{x})$, is shown a short time after the application of noise.

Dykman *et al* have measured a large number of such distributions and averaged each of them to find the corresponding *mean escape time* as a function of noise intensity. As discussed earlier the mean escape time is one useful measure of the "robustness" of the attractor in question. Several different attractors were chosen, and the analogue and numerical simulations are compared in Figures 4.5a and 4.5b.

Both sets of results clearly show that by increasing the noise level attractors become less robust as indicated by the reduced mean escape time. It can also be seen that attractors closer to the chaotic attractor at $F=0.109$ are much more sensitive to noise. This is due to the changing geometry of their respective basins of attraction and will be discussed in greater detail in the following sections. Figure 4.5c shows the comparison of the analogue and numerical simulations.

As can be seen there is a good comparison between both sets of results. However it must be pointed out that noise was applied to the attractor at a phase of 0° in the analogue simulations and at 180° in the numerical simulations. This, assuming that the numerical and experimental inaccuracies encountered were negligible, clearly accounts for the discrepancies at higher noise intensity where the system becomes much more sensitive to the phase at which noise is applied.

4.3.3 Stochastic integrity curves

In Figure 4.2c we have plotted *stochastic integrity curves* for fixed noise intensity $D=0.0004$. This diagram represents how S_m varies for the different attractors which exist at different forcing amplitudes, F . The sequence of attractors chosen is that considered in the analysis of the local integrity.

On first glance the curves seem qualitatively the same as those of the local and global integrity curves, but a closer inspection reveals both similarities and discrepancies between them. However it would be useful to understand the stochastic integrity curves, in terms of noise-free basins of attraction and in the context of the local and global integrity measures.

For forcing levels below $F=0.06$ the basins are smooth, and of approximately the same size; and the position of the attractor remains relatively unchanged. For the noise intensity considered, $D=0.0004$, the stochastic integrity measure S_{16} remains at 1.0, up to $F=0.05$, indicating that all the trials are constrained and hence that the noisy attractors are sufficiently robust to resist appreciable noise-induced failure by the external stochastic noise source. However between $F=0.06$ and $F=0.07$, there is a dramatic drop in S_{16} to about 33% of its previous

value. The explanation is quite simple. At $F=0.069$ there is a hysteresis jump to a new attractor significantly closer to the basin boundary, as exemplified by the local integrity curves. However it must be pointed out that the basin has also become fractal and this may be a contributory, but not a major factor, in the dramatic loss of stochastic integrity between $F=0.06$ and $F=0.07$. Indeed the fractal basin, as well as the fact that the attractor is much closer to the basin boundary, can account for the longer chaotic transients at $F=0.07$ as indicated by the divergence of the S_{16}, S_8, S_4, S_2 and S_1 integrity curves. The effect of the fractal structure is more clearly seen as the forcing amplitude is further increased. This can be seen at $F=0.08$ where, in the noise-free state, the transient time map is very complex indicating that the basin boundary is highly fractal with a fractal dimension of approximately 1.85 (Thompson and Soliman, 1990a). This implies that the system has a high sensitivity to initial conditions and, going one step further, a high sensitivity to noise. The addition of a small amount of noise in these circumstances can easily push trajectories across the boundaries, causing escape. As can be seen in Figure 4.6, when the dimension of the boundary is close to two and the separation between the attractor and its basin boundary is small, the addition of low noise can cause external intermittency. Here a $n=2$ subharmonic attractor at $F=0.107$ becomes practically identical to the chaotic attractor at $F=0.109$, due to the addition of a small amount of noise. Inter-twining basins as those seen in the case of fractals can cause longer chaotic transients as trajectories in an escape sequence map from one finger to the next, and in the presence of noise from one basin to the next.

Another major factor contributing to the reduced stochastic integrity for $F>0.07$ is the continual destruction of the basin. For the noise level considered there is a correlation between the noise sensitivity and the geometry of the basin as we

shall discuss in the next section. The reduction in the size of the basin causes a greater likelihood that the attractor escapes. This process continues until the final destruction of the attractor at a crisis when $F=0.109$.

4.3.4. Correlation between stochastic integrity and the basin of attraction

In this section we examine the stochastic integrity curves in more detail to see if, under increasing noise intensity, there still exists a well defined relationship between the noisy attractor and its noise-free basin of attraction (Gwinn and Westervelt, 1986a, 1986b). Considering firstly the condition $D=0$, all trajectories lying within the basin converge towards the attractor and once there remain for infinite time. The basin in effect plays no further role in the stability of its attractor. This is clearly seen in Figure 4.7 where obviously all the trials are constrained for $D=0$. As the noise is increased very slightly to $D=0.00001$, the noisy attractors (at low forcing amplitudes) lying within smooth, large basins ($F<0.07$) tend to be relatively unaffected by the external noise, whereas attractors lying close or within fractal boundaries (which tend to be sensitive to initial conditions in the noise-free state anyway) are a little more sensitive. There is no dramatic drop in the stochastic integrity curve. Here, although the noise affects the local stability properties of *all* the attractors, the global stability remains relatively unchanged for most of them. For the sake of this presentation, as we are considering reasonably short transient behaviour, we can consider that noisy attractors lie within *noisy basins* and their robustness depends upon the geometrical properties of these basins.

Increasing the noise level to $D=0.0004$ has a similar effect on the attractor. However attractors closer to the basin boundary (from the effect of the hysteresis jump) are significantly more sensitive to this noise level. The same is true for $D=0.0008$ but here attractors lying within a resonant hysteresis are more sensitive to the increased noise level. The reason for this is that although the attractor considered lies well within the constraint basin boundary, it is relatively close to the boundary that separates it from its co-existing attractor. The addition of noise may generally not be enough to cause this attractor to escape directly but can push it across the boundary to its co-existing attractor which is significantly closer to the escape basin boundary and hence much more sensitive to noise-induced failure.

It can now be said that for the small noise levels considered so far ($D < 0.0008$) the stability of the noisy attractors can be put in the context of their original noise-free basins of attraction, and correlated with the local and global integrity curves. Attractors lying close to their basin boundary are inherently more sensitive to noise-induced hopping.

However at higher noise levels, although there is hardly any change in the size or nature of the noise-free basins of attraction, or in the position of the attractors within them (as indicated by the transient time maps, local and global integrity curves) for $F < 0.05$, there is an instantaneous fall of the stochastic integrity measure. The reason for this is that both the noisy attractor and its noisy basin are qualitatively different from their original geometry, and hence the noisy attractor bears no correlation to its original basin of attraction.

4.3.5 Noise Modelling

Figure 4.8 shows the results obtained using the noise modelling technique outlined in section 4.3.3. The results are qualitatively similar to those obtained by adding *real* noise to the system as seen by the stochastic integrity curves of figure 4.2c. There is a sharp drop in the stochastic modelling integrity curves just after the hysteresis jump, although not of the same magnitude as that of the stochastic integrity curves. There are several reasons for this. Firstly we have assumed rotational symmetry in the stochastic response of the attractor which is obviously not the case: as we have seen, the attractor broadens along the axis of weakest compression. Secondly we have assumed that there is no change in the geometry of the transient basins after the application of noise. Obviously this is not the case as shown in section 4.3.3. Thirdly the relationship between the input noise intensity in the *real* case and the output response distribution in the *modelling* case is not clearly established.

4.4 Summary of chapter

We have analyzed the effect of an external noise in a driven damped oscillator for varying forcing amplitudes. Stochastic integrity measures have been used to describe the sensitivity of an attractor to noise-induced jumping. Global and local integrity curves have been used to describe changes in the geometry of its corresponding basin of attraction. Our studies have lead to several conclusions:

(1) *Global integrity curves* clearly indicate basin boundary changes in terms of the size of the basin of attraction. A homoclinic tangency of the stable and unstable

manifolds, resulting in a fractal basin, dramatically enhances the erosion of the basin of attraction.

(2) A hysteresis jump or movement of the attractor as a system parameter is varied can cause the attractor to move much closer to the basin boundary without any change in the size of the basin of attraction. This is clearly indicated by the *local integrity curves*.

(3) The addition of noise can cause qualitative changes in the appearance of an attractor. Increasing the noise intensity increases the sensitivity of attractors to noise-induced hopping (in our case usually causing trajectories to escape). The stochastic integrity measure clearly quantifies such behaviour as well as the relative response of different attractors subjected to the same noise level.

(4) *Stochastic integrity curves* give the relative response of a naturally occurring sequence of attractors subjected to a fixed noise intensity. It was found that

(a) At extremely low noise intensities, attractors lying within fractal basin boundaries were much more sensitive to noise-induced failure than their smooth-basin counterparts.

(b) At slightly higher noise intensity a hysteresis jump causes the system to become considerably more sensitive to noise. Attractors lying within the region of resonant hysteresis were hardly affected at all. However increasing the noise level further often *indirectly* caused the attractor lying within the resonant hysteresis to escape. The reason is that although the attractor lies well within the constraint boundary, it is relatively close to the boundary that separates it from its coexisting attractor. The

addition of noise might not cause the attractor to escape directly, but could push it over to its coexisting attractor, which is significantly closer to the basin boundary and hence more sensitive to noise-induced failure at a later time.

(5) The global stability and escape statistics of a noisy attractor can be assessed in terms of its noise-free basin of attraction for low noise levels. However at higher noise levels this ceases to be the case. These deductions are clearly established by the stochastic, global and local integrity curves.

Figure 4.1 Basins of attraction where

black represents no escape within 16 cycles

white represents escape within 16 cycles

For each figure $\omega = 0.85$, $\beta = 0.1$, $\phi = 180^\circ$ in the window: $-0.8 < x < 1.2$ $-1.0 < y < 1.0$

A triangle represents the position of the main sequence attractor.

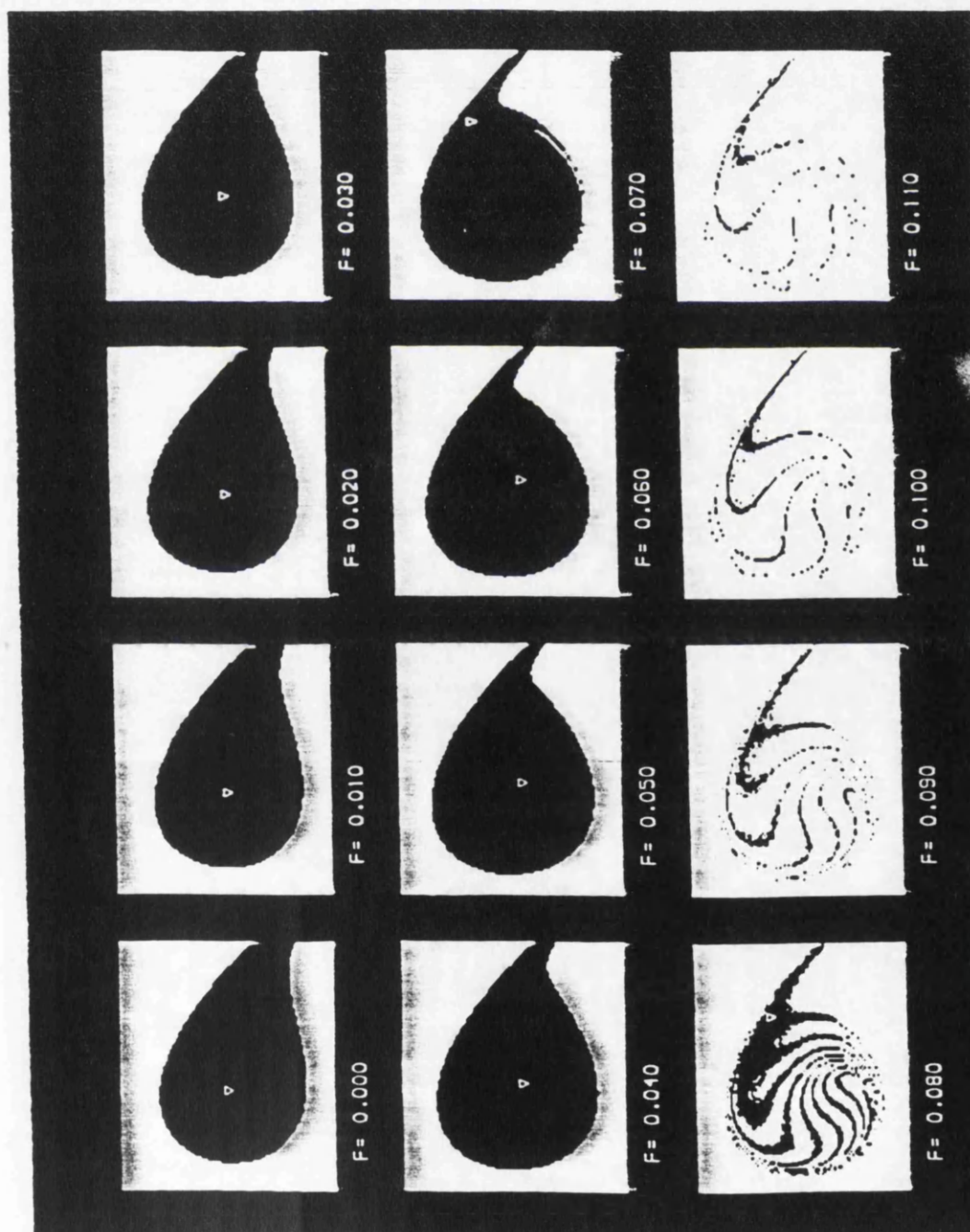


Figure 4.2 Loss of engineering integrity under increasing F .

(a) Global integrity curves

(b) Local integrity curves

(c) Stochastic integrity curves

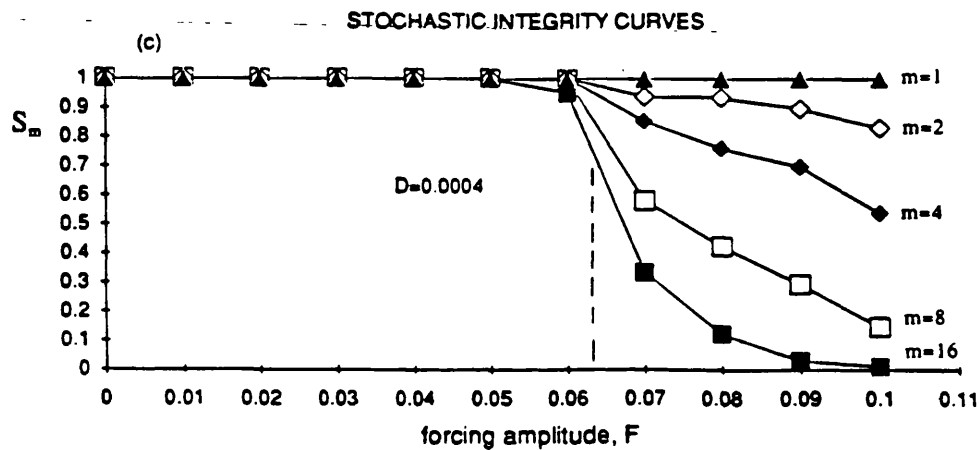
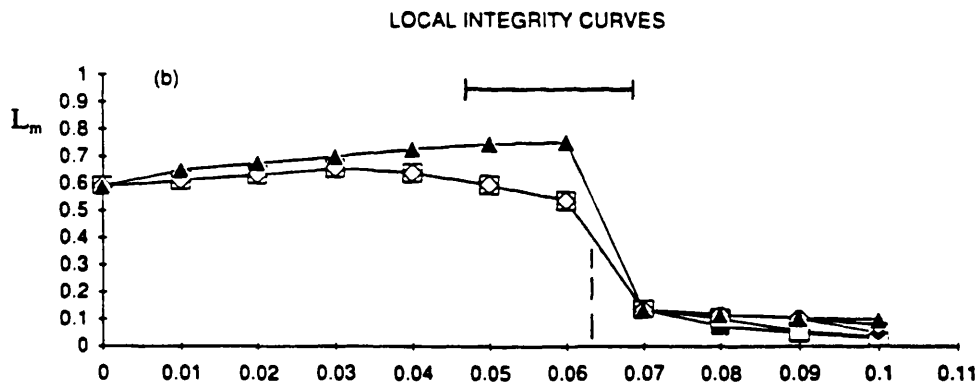
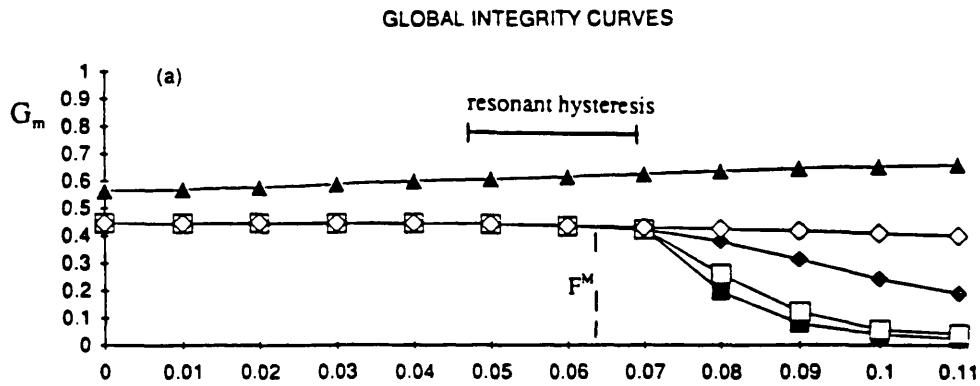


Figure 4.3 Stochastic integrity measure, S_{16} , versus noise intensity, D .
Attractors chosen are at $F=0.01$ and $F=0.07$.

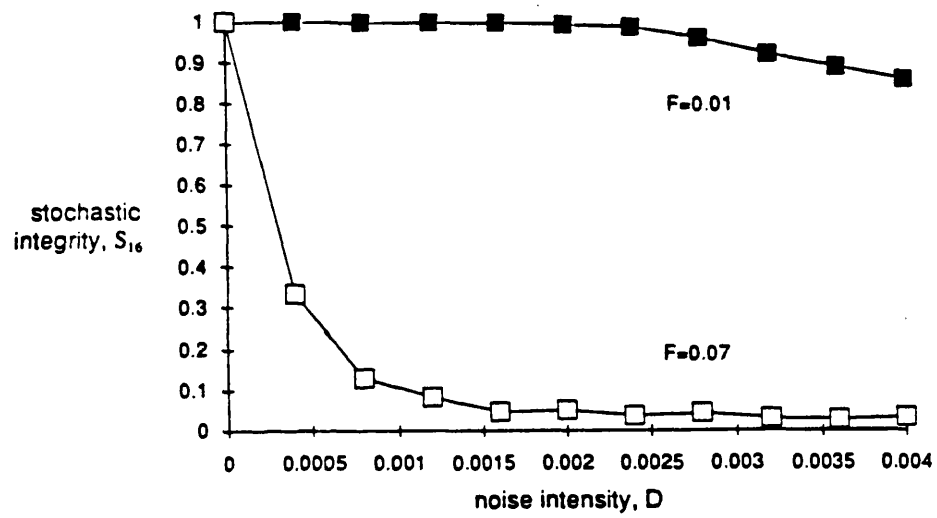


Figure 4.4 Analogue simulations by Lancaster group (Dykman, *et al*, 1989) using an electronic model.

(a) A stochastic phase portrait with

$$\beta = 0.1, \omega = 0.85, F = 0.109, D = 9.5 \times 10^{-6}$$

$$-1.07 < x < 2.14, -0.83 < \dot{x} < 0.83$$

(b) Probability distribution $P(t)$ of the escape times from the main sequence period-one attractor at $F=0.099$ ($\beta = 0.1, \omega = 0.85, D = 8.7 \times 10^{-5}$)

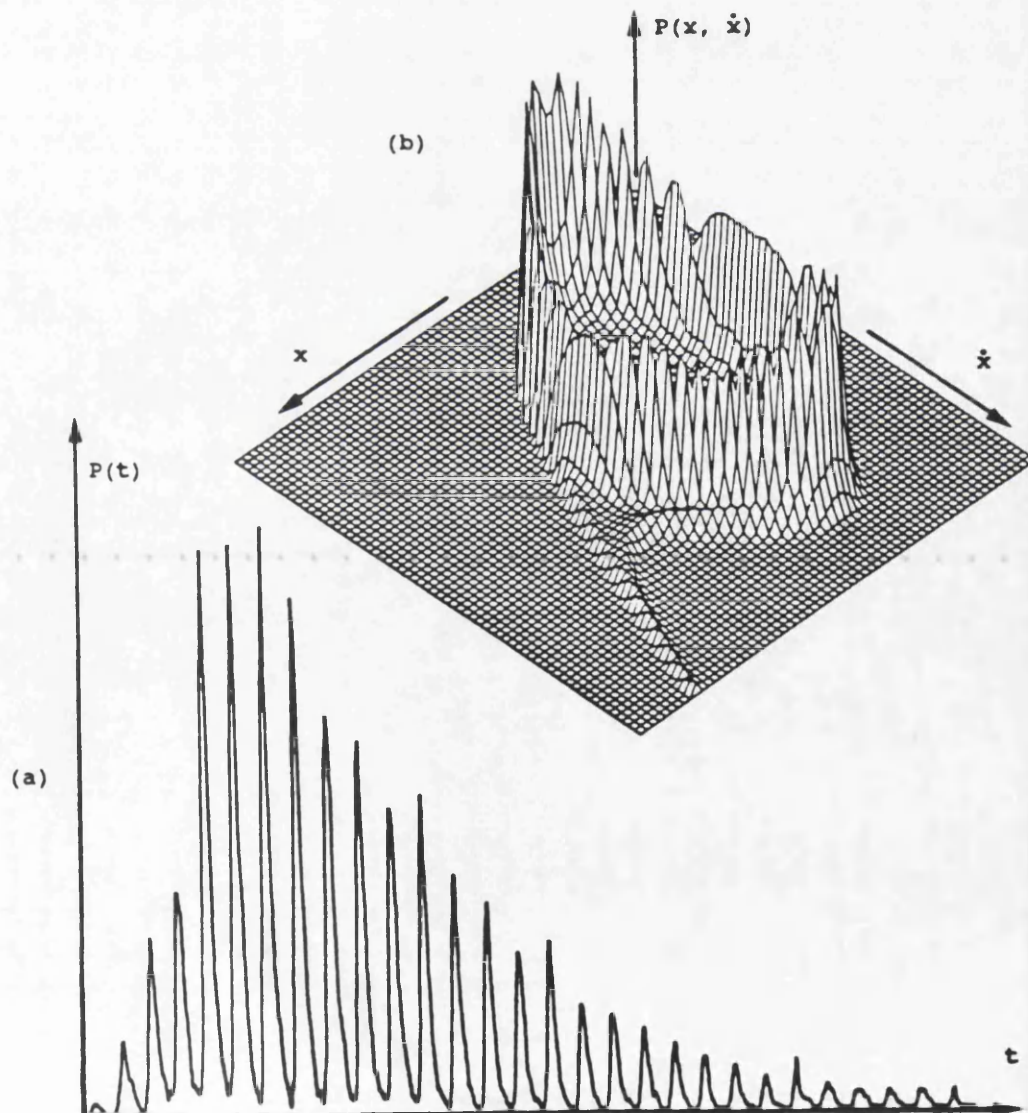


Figure 4.5

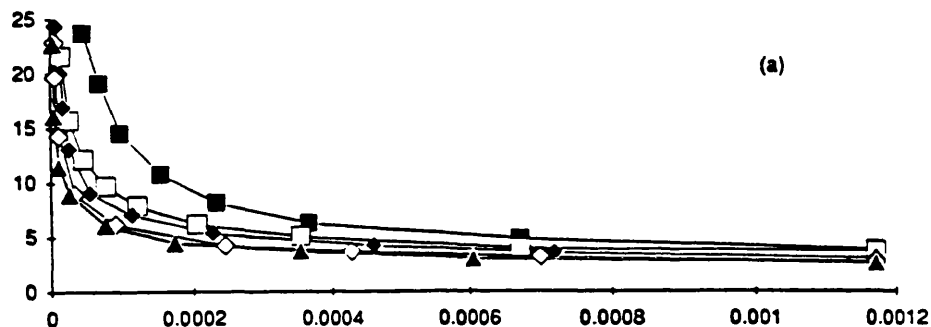
(a) Mean escape time (forcing cycles) versus noise intensity, D , using analogue computer.

Attractors considered are at $F=0.089$ (black square, $n=1$), $F=0.099$ (white square, $n=1$); $F=0.102$ (black diamond, $n=2$), $F=0.107$ (white diamond, $n=2$); $F=0.109$ just below F^E (black triangle, chaotic attractor).

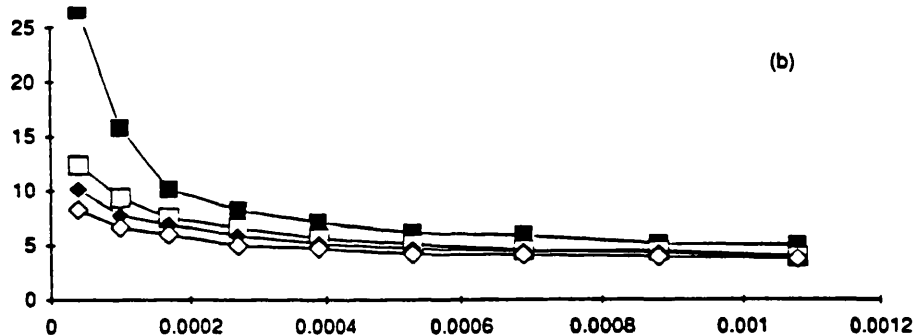
(b) As 5a but using numerical technique.

(c) Comparison of 5a and 5b for attractor at $F=0.089$.

ANALOGUE COMPUTER RESULTS



NUMERICAL RESULTS



COMPARISON OF NUMERICAL AND ANALOGUE SIMULATIONS

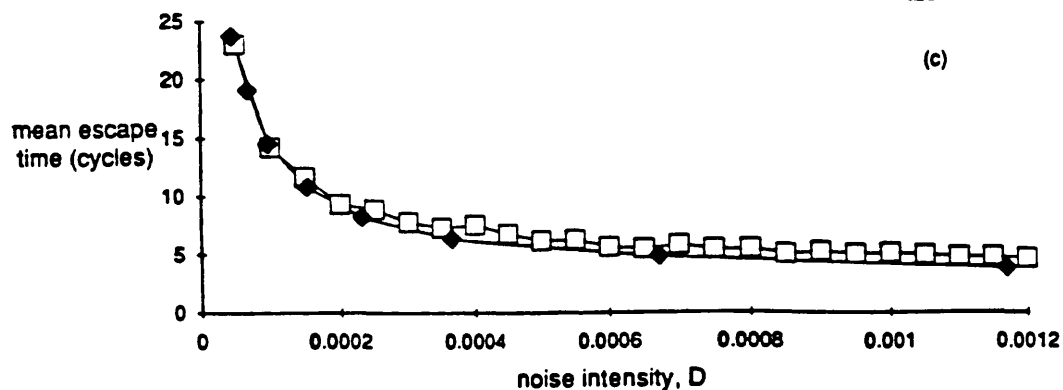


Figure 4.6 Addition of external noise to the $n=2$ attractor at $F=0.107$ produces a 'noisy attractor' visually similar to the main sequence chaotic attractor at $F=0.109$.

- (a) Chaotic attractor at $F=0.109$
- (b) Period $n=2$ attractor at $F=0.107$
- (c) Noisy attractor at $F=0.107$, $D=0.0001$
- (d) Noisy attractor at $F=0.107$, $D=0.0002$

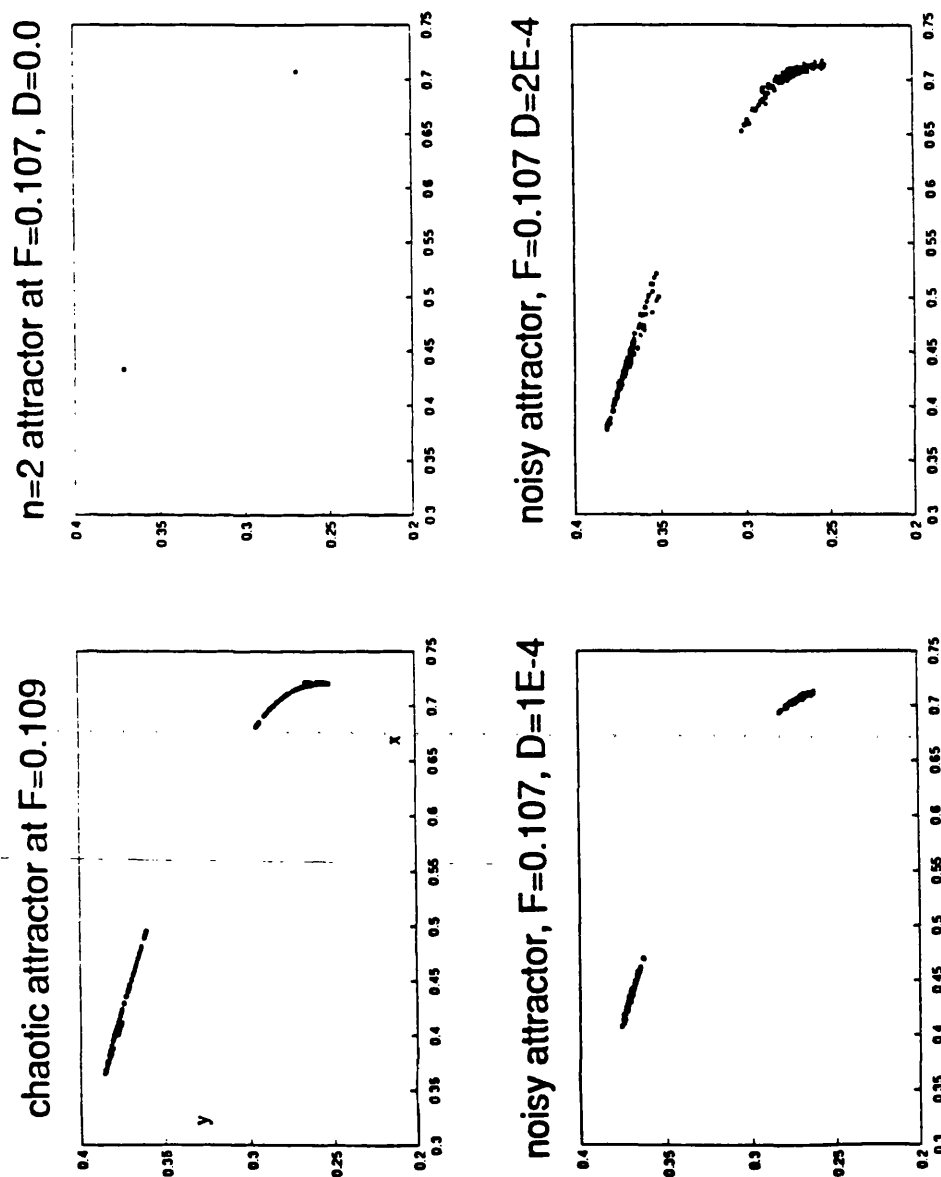


Figure 4.7 Stochastic integrity measure, S_{16} , versus forcing amplitude for different noise intensities, D .

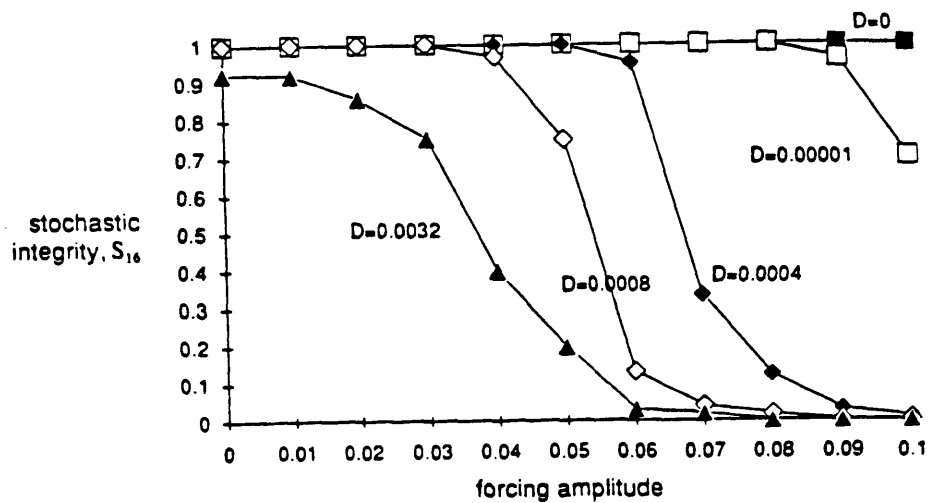
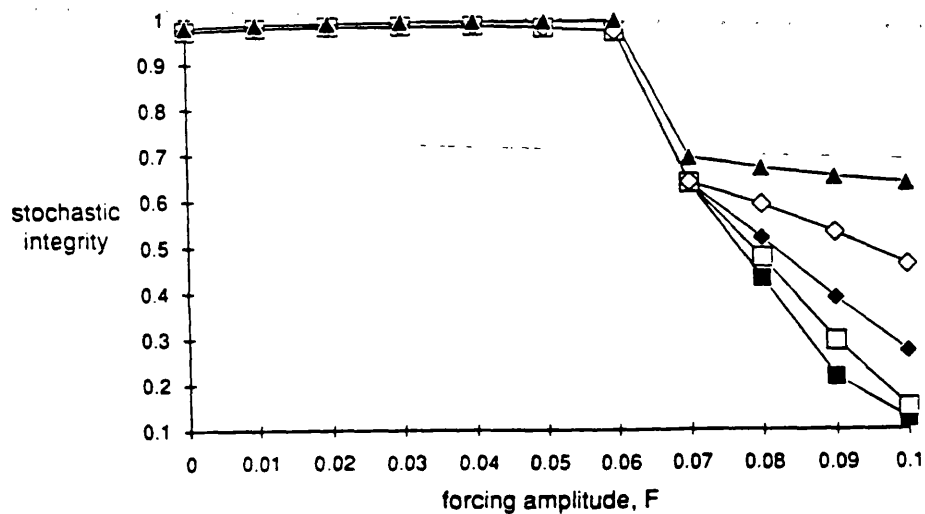


Figure 4.8

Figure 4.8 Stochastic integrity measure versus forcing amplitude using noise modelling technique.



CHAPTER 5: ENGINEERING RELEVANCE OF BASIN EROSION AND CHAOTIC TRANSIENTS

5.1 Introduction

In assessing the engineering significance of chapters 3 and 4, especially in relation to ship capsize, we have concluded that rather than analysing the intricate patterns of bifurcating steady states, it is both simpler and more relevant to focus attention on (transient) basin boundaries. The exploration of these using a grid of starts in the space of the starting conditions is a conceptually simple and easily automated approach, suitable for routine design studies; and due to the rapid erosion of the safe basin long before the final extinction of the last stable attracting solution, the transient basin approach is much more relevant to engineering systems in noisy or ill-defined systems. This conclusion is reinforced by the fact that basin boundaries become fractal, adding a new degree of uncertainty to the response.

The engineer ultimately needs design data in the space of the system parameters (control space), and one diagram that has both scientific and practical interest is the safe basin locus in parameter space corresponding to motions from the ambient resting state of zero displacement and zero velocity. This might correspond to a structural component subjected to a sudden earthquake tremor, or to a boat experiencing a worst case resonant excitation from a short train of regular waves. This control space diagram will reflect the fractal character of the phase-space basins, and due to the rapid erosion and fragmentation of the latter, it can be expected to give a good guide to the safe parameter

regime.

5.2 Fractal boundaries in control space

When a metastable, damped, oscillator is driven by strong periodic forcing, the catchment basin of constrained finite motions in the phase space of the starting condition $\{x(0) = \dot{x}(0) = 0\}$ is known to develop a fractal boundary associated with a homoclinic tangling of the governing invariant manifolds. The four dimensional basin in the phase control space spanned by $\{x, \dot{x}, F, \omega\}$ where F is the magnitude and ω is the frequency of the periodic excitation, will like-wise acquire a fractal boundary, and we here explore the engineering significance of the control space cross-section for example to $x(0) = \dot{x}(0) = 0$. The fractal boundary of this section is a locus for a mechanical or electrical system subjected, while resting in its ambient equilibrium state, to a sudden pulse or train of steady periodic excitation. We assess here the relative magnitude of the uncertainties implied by this fractal structure for the optimal escape from a universal cubic potential well. Both absolute and transient basins are examined, giving control-space maps analogous to the familiar pictures of the Mandelbrot set.

Indeed although almost totally unknown in an engineering context, this concept of a fractal control boundary in control space is well known to mathematicians which are clearly illustrated in the classical pictures of Mandelbrot (Mandelbrot, 1977). Here the escape to infinity of the complex iterated map $z \Rightarrow z+c$ from the fixed starting condition $z=0$ serves to locate the Mandelbrot set (defined in terms of the connected Julia sets)

in the real two-dimensional space associated with the complex control c . This follows from the results of Julia and Fatou which show that the Julia set is connected if and only if $z=0$ lies outside the domain of attraction of the attractor at infinity. Meanwhile, contour colouring of the iteration-time to escape beyond some arbitrary remote boundary yields the classical pictures exemplified by Peitgen and Richter (1986).

Corresponding transient-time maps in control space for periodically driven oscillators governed by differential equations of the form

$$\ddot{x} + f(x, \dot{x}) = F p(t) \quad (5.1)$$

(where a dot denotes differentiation with respect to time t) may be of interest for the more practical reason that a mechanical or electrical system in its ambient equilibrium state might be required to resist pulse of excitation of magnitude F and frequency ω . The set (F, ω) values that can sustain such a pulse is here the set of absolute constraint, C_∞ , corresponding to the Mandelbrot set : while the control parameters that prevent escape within a time define a set of *transient constraint*, C_τ , which can be conveniently colour coded in a map of the (F, ω) space.

5.3 Four dimensional phase-control space

In this section we formally define the phase-control space we shall be considering, and outline the numerical techniques used in obtaining our results. We shall present computer studies of the escape equation (3.1) keeping β constant at 0.1. By using a

fourth order Runge Kutta numerical time integrations from a simple grid of starts, typically 100 by 100. Each integration is continued until x exceeded 20, at which point the system is deemed to have escaped, or the maximum allowable number of forcing cycles, M , (typically 16 or 32) is reached. In this way the set of points in the four dimensional phase-control space spanned by $\{x(0) = \dot{x}(0), F, \omega\}$ that do not escape within m forcing cycles defines a *transient* safe basin, C_m , the basin for $m=M$ hopefully giving a good approximation to the *absolute* safe basin, C_∞ . Specifying the controls (F, ω) and taking a grid in the $\{x(0) = \dot{x}(0)\}$ plane allows us to draw the conventional cross-sections of C_m in the phase-space of the starting conditions: while specifying $\{x(0) = \dot{x}(0)\}$, say equal to $(0,0)$, and taking a grid in the (F, ω) plane allows us to draw the cross-sections of C_m in the two dimensional control space.

Notice that in keeping with our earlier philosophy, we are throughout this study making no note of the attractors, be they harmonic, subharmonic or chaotic, onto which the non-escaping motions might settle. At many control settings there are of course competing attractors within the well, some with exceedingly small domains of attraction.

5.4 Control space basins and the escape boundary

Starting all time integrations at $x(0) = \dot{x}(0) = 0$ and using a grid in the control space gives the (F, ω) cross-sections of the safe basins in Figures 5.1 and 5.2.

The top left-hand picture of Figure 5.1 shows the various bifurcation curves, while the remaining three pictures, in which the region of greatest interest is progressively

enlarged, shows the boundaries of C_4 and C_M . Regions that give no escape in M forcing cycles are indicated in black: regions that lead to escape in between 4 and M cycles are indicated by the grey dotted area: regions that lead to escape in less than 4 forcing cycles are represented by white. The values of M (16 or 32) are indicated in the caption. More detailed coloured versions, one of which is shown in Figure 5.2, confirm the boundary of C_{16} is for practical purposes a very good approximation to the boundary of C_∞ .

The curve A rising sharply to the left from the cusp point P is the saddle-node fold locus located by a numerical bifurcation-following routine. It represents the final resonant jump out of the potential well for the approximate frequency range $0.6 < \omega < 0.8$, there being no attractor within the well at values of F just above this curve. The curve C rising steeply to the right is the period-doubling flip bifurcation, from harmonic to subharmonic of order two, that signals the start of a short period-doubling cascade to chaos and escape. So for the approximate range $0.8 < \omega < 1.0$ the ultimate escape locus, beyond which there is no attractor in the well, is given by a boundary crisis line running just above this flip locus as indicated in the first diagram of Figure 5.1 by the white line, E , between the hatched and dotted regions: more details can be seen in Figure 3.1. At $\omega=0.85$ this boundary crisis is at $F=0.109$ as we have previously indicated. The other locus of interest is the Melnikov curve, M , rising slowly to the right, which in this region of control space is an accurate approximation to the curve of homoclinic tangency at which the phase-space basin becomes fractal.

The *escape boundary* beyond which there are no available attractors in the well is thus given by the fold curve and the crisis curve, the condition of optimal escape, Q , being where these curves intersect at $\omega=0.80$. The boundary of C_∞ must of course fall below this escape locus, and the boundary of C_{16} falls predominantly below the drawn flip and

fold lines. Notice however that for $\omega > 0.8$ the boundary of C_{16} is quite substantially lower than the escape boundary, corresponding to the substantial erosion of the phase-space basin at these forcing frequencies.

The fractal structure of the control space cross-section becomes increasingly clear in the lower enlargements of Figure 5.1, and is seen to the best advantage in the colour picture of Figure 5.2 for which $M=32$. Here we can see that at $\omega=0.85$ thin fingers penetrate into C_{32} to the values of the forcing magnitude of $F=0.0725$. This is about 70 per cent of the crisis value of $F=0.109$, but correlates well with the rapid erosion of the phase space basin that we observed in Figures 3.2 and 3.6.

The fingers of the control-space pictures of Figure 5.1, are of course different cross-sectional representation of the fractal structure of C_∞ in the four dimensional phase-control space. The fractal boundary thus implies an extreme *final state sensitivity to both the starting conditions and the parameter values*.

5.5 Fractal Dimension

The data from the grid of starts, used to produce the transient time maps, can be used to estimate the fractal dimensions of the phase and control boundaries, using a similar technique to Grebogi et al (1983) in their study of final state sensitivity. For each grid point in turn, we inspect expanding circuits of adjacent grid points and record which circuit number, or tolerance, ϵ , that first gives a change of basin. We then determine the fraction of grid points, $f(\epsilon)$, that are uncertain for tolerance ϵ , and use the relation

$$f(\epsilon) = K\epsilon^{D-d} \quad (5.2)$$

where K is a constant, D is the dimension of the cross-section (in our case 2), and d is the required *fractal dimension of the basin boundary*. Plotting $\ln f(\epsilon)$ versus $\ln \epsilon$, for several values of ϵ , and using a least squares fit to calculate the slope and hence d .

Figure 5.3 shows the fractal dimension of the basin boundary in phase space where F and ω are fixed. For Figure 5.3a, $\omega=0.85$, $F=0.05$ (i.e. $F < F^M$) and for figure 5.3b, $\omega=0.85$ and $F=0.08$ ($F > F^M$). From these sample plots, it can be seen that linear dependence of $\ln f$ with $\ln \epsilon$ is evident, indicating a power law dependence as in equation 5.2. We find that for $F=0.05$ that $d=1.03$, indicating a good approximation to the value of unity that we expect for a smooth, non-fractal boundary before the homoclinic tangency. At $F=0.08$ we have a slight curve, and taking the slope at the right hand end, which corresponds to the smallest ϵ values and will therefore give the best estimate for the dimension, we obtain $d=1.805$. This is then the fractal dimension of the phase-space boundary just beyond the homoclinic tangency.

The variation of the phase space dimension with F is shown in figure 5.4 where the correspondence with the engineering integrity curve is clearly seen. Within the accuracy of our results, we see that the dimension d remains at unity corresponding to a smooth boundary up to the homoclinic tangency at F^M when it jumps to a high, non-integer value characteristic of a fractal boundary. The subsequent fall back towards unity may well be due to the coarseness of our grid, which cannot deal adequately with the increasingly fine fractal structure.

The log-log plot for our analysis of the $x(0) = \dot{x}(0) = 0$ control- space boundary of $C_{32} \approx C_\infty$ is shown in Figure 5.5. Here we have a good straight line, yielding the estimate

$d=1.38$ for the fractal dimension.

5.6 Transient basins as a new approach to ship capsize

To illustrate the potential relevance of the current study to wider problems of engineering analysis and design, we give appraisal of the ship capsize problem that has attracted a lot of attention in recent years (Bird & Morall, 1986; Miller *et al*, 1986; Virgin, 1987). The ideas that we outline here are developed in more detail in the next chapter.

5.6.1 Ship capsize as the escape from a potential well

A boat that can capsize corresponds to a damped mechanical oscillator whose underlying total potential energy has a minimum in the upright state and a saddle point (a maximum in the simplest one-degree of freedom idealization) beyond which the system can escape to a capsized equilibrium state. The problem of capsize is therefore a straight-forward example of an escape from a potential well.

In beam seas, a *worst-case excitation scenario* would seem to correspond to a short train of regular waves, reducing the capsize problem to that of escape, in a finite time, from a potential well under a pulse of periodic forcing. The starting conditions of a boat are essentially unknown, but might be close to the ambient floating state in still water.

5.6.2 Relevance of the current study

Our work on the escape from a cubic potential well is a thorough scientific study of a specific, carefully chosen archetypal equation, highlighting phenomena that are likely to be typical of the wide class of capsizing problems of concern to the naval architect. Additional features of more realistic capsizing models that in no way should invalidate any of our general overall conclusions are: added hydrodynamic mass; complex nonlinear damping functions; periodic but non-sinusoidal forcing; more complex forms of the potential function, including in particular the symmetric or near symmetric potentials typical of an unbiased boat that could capsize either way; more than one degree-of-freedom, allowing for example, the coupled heaving and rolling motions of a boat to be considered; and a periodic component in the stiffness function, allowing a consideration of Mathieu phenomena in the heave motions. Indeed, in the next chapter we make a detailed analysis of ship roll motion which includes some of the features outlined above.

5.6.3 Computer time integrations must replace analysis

We feel that in the future, theoretical studies should be predominantly based on computer time integrations of the modelled nonlinear equation of motion. *Nonlinear analysis*, using for example averaging or perturbation techniques, can give some rough idea of the response in restricted parameter regimes, but cannot begin to unravel the intricate harmonic, subharmonic and chaotic solutions and their bifurcations that govern the escape process (Thompson, 1989). Moreover the thrust

of our argument is that attention should be focussed on basins of attraction, and here nonlinear analysis is even less of an option: Liapunov methods are likely to be hopelessly arbitrary and conservative, while the validity of Melnikov's perturbation analysis, which is the only technique for predicting the onset of the fractal structure that concerns us here, is restricted to small parameter regimes (it is moreover too complex for routine application by naval architects to realistic potential functions). We therefore conclude that the only sensible procedure is to use the *great computing power and excellent-time integration algorithms* now widely available to simply solve the governing nonlinear equations numerically to find the real solution from a given starting condition, structuring the investigation from an ensemble of starts in the light of the powerful new phase space concepts of dynamical systems theory (Thompson & Stewart, 1986).

5.6.4 Complexity and irrelevance of the steady states

The problem with any driven nonlinear oscillator is that it is likely to have a large number of alternative steady state post-transient solutions including harmonic oscillations at the driving period, subharmonics at the driving period, and chaotic non-repeatable motions. Analysis and supercomputers can be equally helpless in locating all the steady states, although computers programmed to search for the stable solutions can be expected to pick up all those with a sizeable attracting basin. Rather than search for all the attractors, it is indeed conventional to follow the continuous trace of solutions as one of the control parameters, say F or ω , is slowly

varied. Thus in our own studies we have kept ω constant and slowly increased F from zero. At $\omega=0.85$, for example, this yields a path of harmonic oscillations, involving a jump to resonance within the potential well, followed by an infinite cascade of period-doubling flip bifurcations running through subharmonics of order 2, 4, 8, 16, ... ∞ which generates a chaotic attractor. This stable attracting solution of steady-state chaos finally loses its stability at F^E . Repeating this study at different ω values allows us to build up the bifurcation diagram in the (F, ω) parameter space, and in particular determine the escape boundary as in the first picture of Figure 5.1.

This complex and time-consuming numerical investigation is clearly out of the question for the naval architect, and it is our thesis that it is for him both unnecessary and irrelevant. The steady states, beloved by the perturbation analyst, are only approached after perhaps fifty forcing cycles, so for a realistic assessment of vessel safety we are obliged to pay more attention to the transient responses, which are governed by the basins of attraction. Doing this not only gives us an easier investigation, but the results show that by assuming a boat is safe so long it has a stable mode of oscillation, with $F < F^E$, is extremely dangerous because the basin of attraction is very rapidly eroded at a value just above F^M , which can be quite a small fraction of F^E . So we feel that preference should be given to our transient basin approach which is *both easier and more relevant* than the conventional emphasis on infinitesimally-stable attracting steady states.

5.6.5 Transient basins and engineering integrity curves

Running integrations from a grid of starts in the space of the starting conditions, we can readily map out the basin of non-capsizing starts in the space of the initial conditions. In the case of a one-degree-of-freedom model this is particularly easy, because the space is two-dimensional spanned by $x(0)$ and $\dot{x}(0)$. We can then conveniently quantify the size of the safe basin, within the window represented by our grid, by recording the proportion of starts, P_m , that do not lead to capsize within m wave periods. We need moreover only let the system run for only say $M=8$ forcing periods, since our results show that if the boat does not capsize within 8 wave periods it is unlikely to capsize at all.

We can see that this is a very simple procedure, both conceptually and computationally, requiring essentially no knowledge of advanced dynamics, and suitable for routine design studies: and yet we feel is in fact more relevant than more sophisticated approaches.

Transient basins, and the *integrity measures*, P_m , which give us the probability of survival of the boat in a given sea state, are thus readily determined at any desired value of forcing magnitude, F , and frequency, ω . Fixing one of these, ω , we can then plot P_m against F for various appropriate m values to give us what we have called an *engineering integrity diagram*, as shown in figure 5.4. It is the dramatic reduction of engineering integrity at a value of F well below F^E that we must now address.

5.6.6 Dramatic and dangerous erosion of the safe basin

Our findings as summarised by Figure 5.4a are of considerable interest from both a theoretical and practical point of view. Here the case of $\omega=0.85$ is of considerable interest as it is close to the *worst wave frequency* that gives, due to the softening of the nonlinear resonance characteristic, capsizes under the minimum forcing magnitude. We see that the safe basin (for $m=8$ or 16 , say) undergoes very little change of shape or area up to a value of $f \equiv F/F^E \approx 0.58$, and shortly after which it is rapidly eroded by the incursion of finger-like striations which cover the entire basin. By $f=0.0725$, over half the basin area has been lost, and the integrity of the boat would be in serious doubt, especially as the basin is no longer a simple shape, but infinitely striated as a result of the homoclinic tangency. This tangency, predictable for a restricted parameter range, by Melnikov's perturbation analysis, is known to be a feature of all escape situations. This phenomena that we are outlining here is therefore a feature of all capsize problems and not just a peculiarity of our simple, archetypal equation. This is confirmed in the next chapter. X

As a consequence of this tangling, the basin above F^M becomes fractal with an infinite number of thin fingers protruding into the safe basin. This in itself might not be too serious, but as we have shown, these whiskers rapidly grow into thick fingers that penetrate the bulk of the basin, giving us a rapid erosion that we have just described.

An important observation is that upto F^M the integrity measures $P_2, P_4, P_8, P_{16} (\approx P_\infty)$ are almost coincident, so that if a boat does not capsize within 2 wave periods it is unlikely to capsize at all. However when P_m decreases dramatically just after F^M there is a notable splitting of the integrity curves, so the above rule ceases to hold,

due to what are called *chaotic transient motion*. From a practical point of view, however, the dramatic erosion of the safe basin can be detected quite adequately by the P_8 curve, so computer runs from a grid of starts need be pursued for only 8 forcing cycles.

5.6.7 Control space basin as a transient capsize diagram

Because the phase-space basin is so swiftly eroded across its entire central region, the sudden loss of integrity at $f \approx 0.7$ could be detected by time integrations from a small number of starting conditions. Indeed for many practical purposes an adequate assessment could be made by observing the behaviour from one central start from $x(0) = \dot{x}(0) = 0$. Our control-space cross-sections of figure 5.1 thus take the role of *transient capsize diagrams* showing the safe and unsafe parameter regimes of wave period (corresponding to ω) and wave magnitude (corresponding to F).

The direct determination of this, involving just a grid in (F, ω) space with all runs from the ambient state, is a highly economical yet relevant procedure, which again has the merit of being suitable for use in routine design studies.

5.6.8 Implications for experimental wave-tank simulations

All that has been said about computer simulations applies with equal force to laboratory experiments on model vessels (Rainey & Thompson, 1990) where it is equally important to try to assess the safe basin in the space of the starting conditions.

Clearly the number of different starts that can be made in a given wave excitation will be even less than can be contemplated in computer studies, so the idea of a single transient test from the ambient still-water state is even more appealing.

5.7 Design against earthquake damage

An earthquake shock can for some purposes be regarded as precisely the pulse of periodic loading that we have envisaged in this chapter, exciting a structure resting in its equilibrium ambient state. The trace of the Mexican earthquake was, for example, remarkably sinusoidal in form: an even if the ground motion is itself not sinusoidal, the excitation reaching a structural component will have a greatly enhanced sinusoidal component at the natural frequency of the main structure due to the filtering action. These considerations, together with the fact that our metastable cubic potential is just the form that would be exhibited by a component with an explosive, shell-like post-buckling characteristic, make our present fractal control-space basin of some immediate relevance to earthquake engineering.

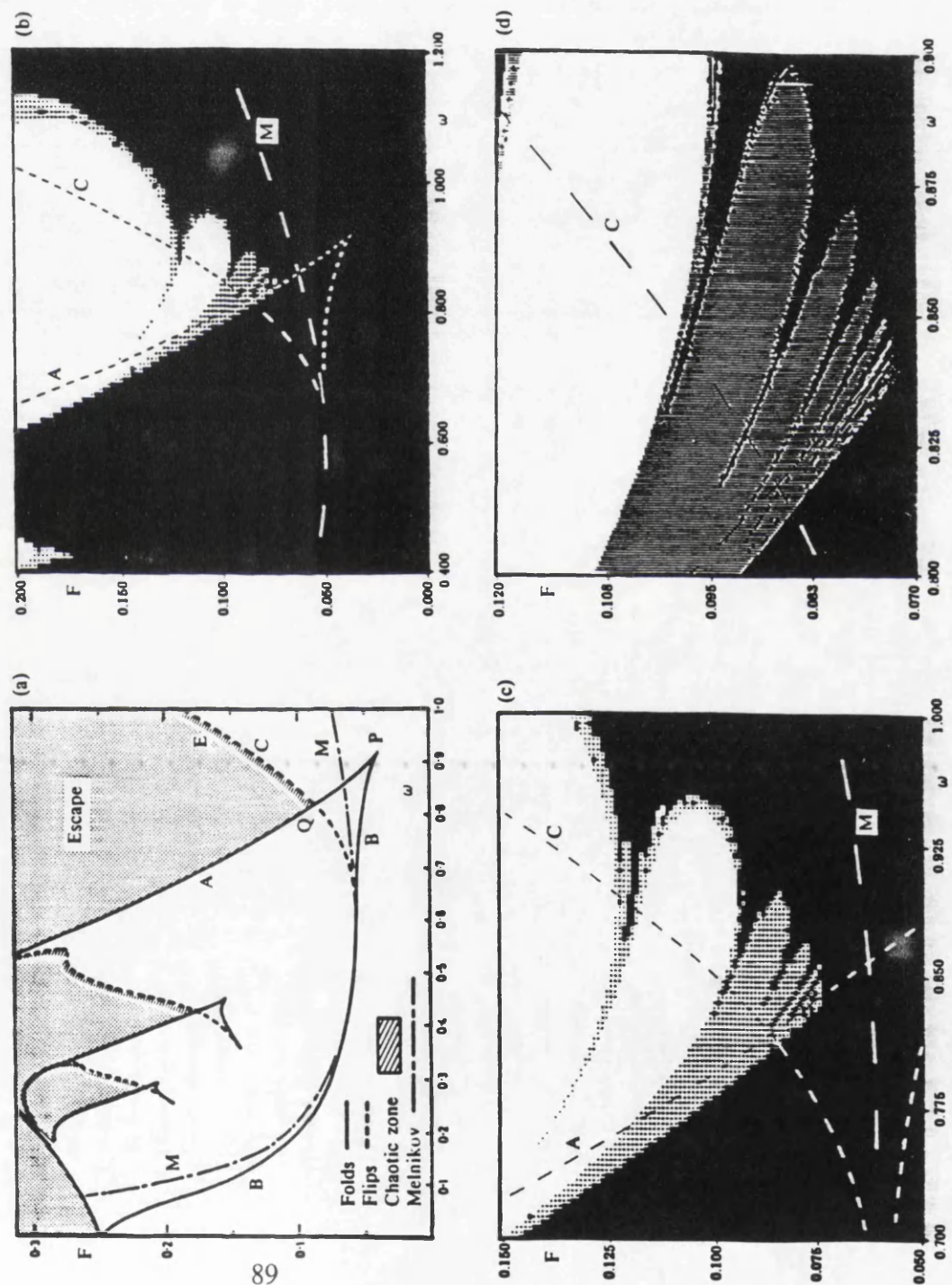
5.8 Summary of chapter

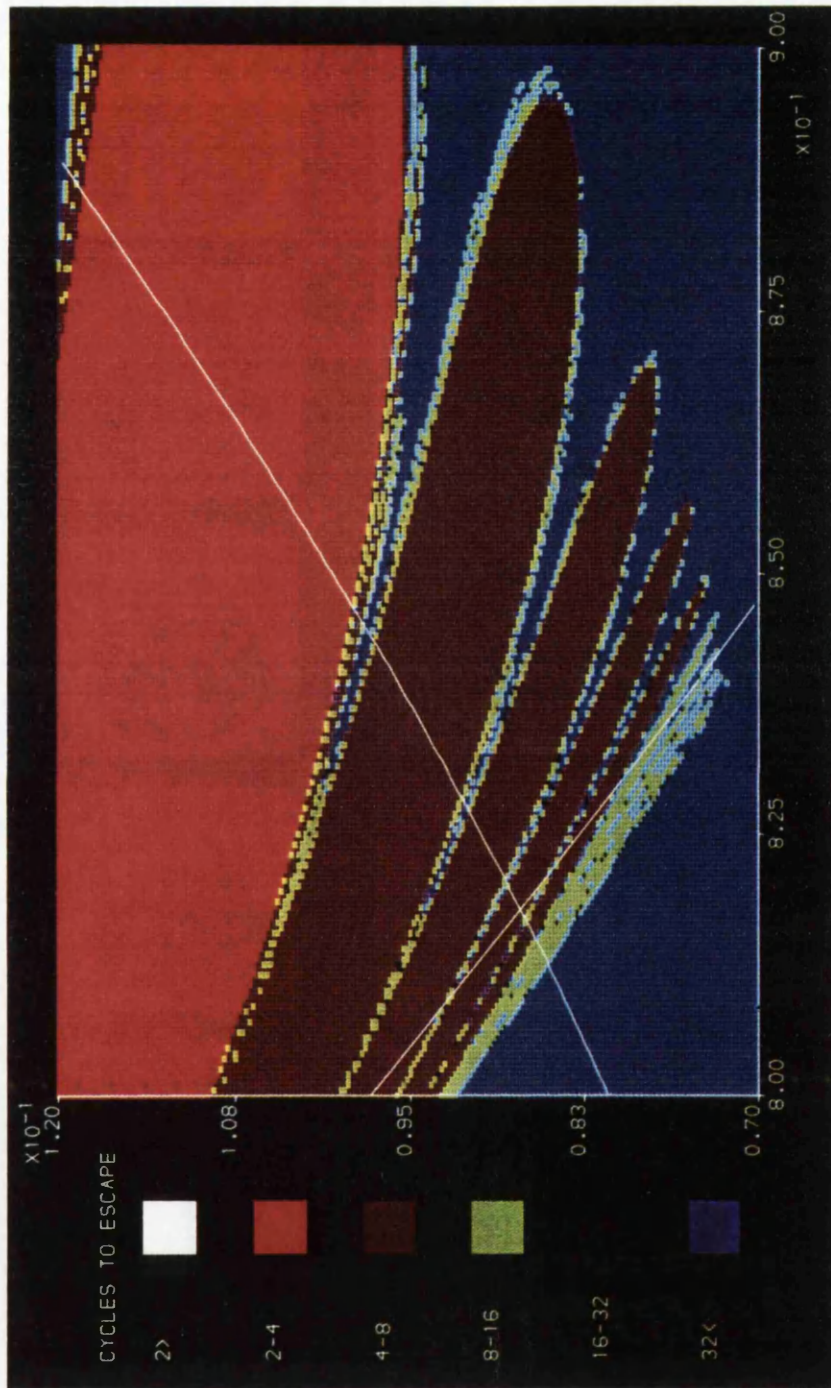
We have seen that our results may have considerable relevance both to ship capsizing in ocean waves, and to building collapse under earthquake loading. In these fields the

phenomena that we have outlined give a qualitative guide to behaviour, rather than specific quantitative results. This is done in the next chapter.

The fine details of the fractal structure are indeed unlikely to be important in an engineering context, especially since they will vary with the starting phase, all our present results having been done at a phase of 180 degrees as we have described. Rather it is the rapid erosion of the bulk of the phase-space basin (a feature that is independent of the starting phase) that we feel is of vital concern to engineers designing systems subjected to periodic or near periodic forcing.

Figure 5.1 Fractal basin boundaries in the (F, ω) control-space corresponding to runs from the ambient state $x(0) = \dot{x}(0) = 0$. Diagram (a) shows the corresponding bifurcation curves. Diagrams (b) to (d) show the progressive enlargements of the control basin with black denoting no escape within M forcing cycles, grey denoting escape between 4 and M forcing cycles, and white denoting escape within 4 cycles: (b) grid is 100 by 100, $M=16$; (c) grid is 100 by 100, $M=32$; (d) grid is 200 by 200, $M=32$.





Fractal basin boundary in the (F, ω) control space, colour coded to show the number of forcing cycles sustained before escape from the ambient state $x(0) = \dot{x}(0) = 0$. Grid is 200 by 200.

Figure 5.3 Log-log plots to estimate the *fractal dimension* of the phase-space boundary above and below the homoclinic tangency ($\omega=0.85$).

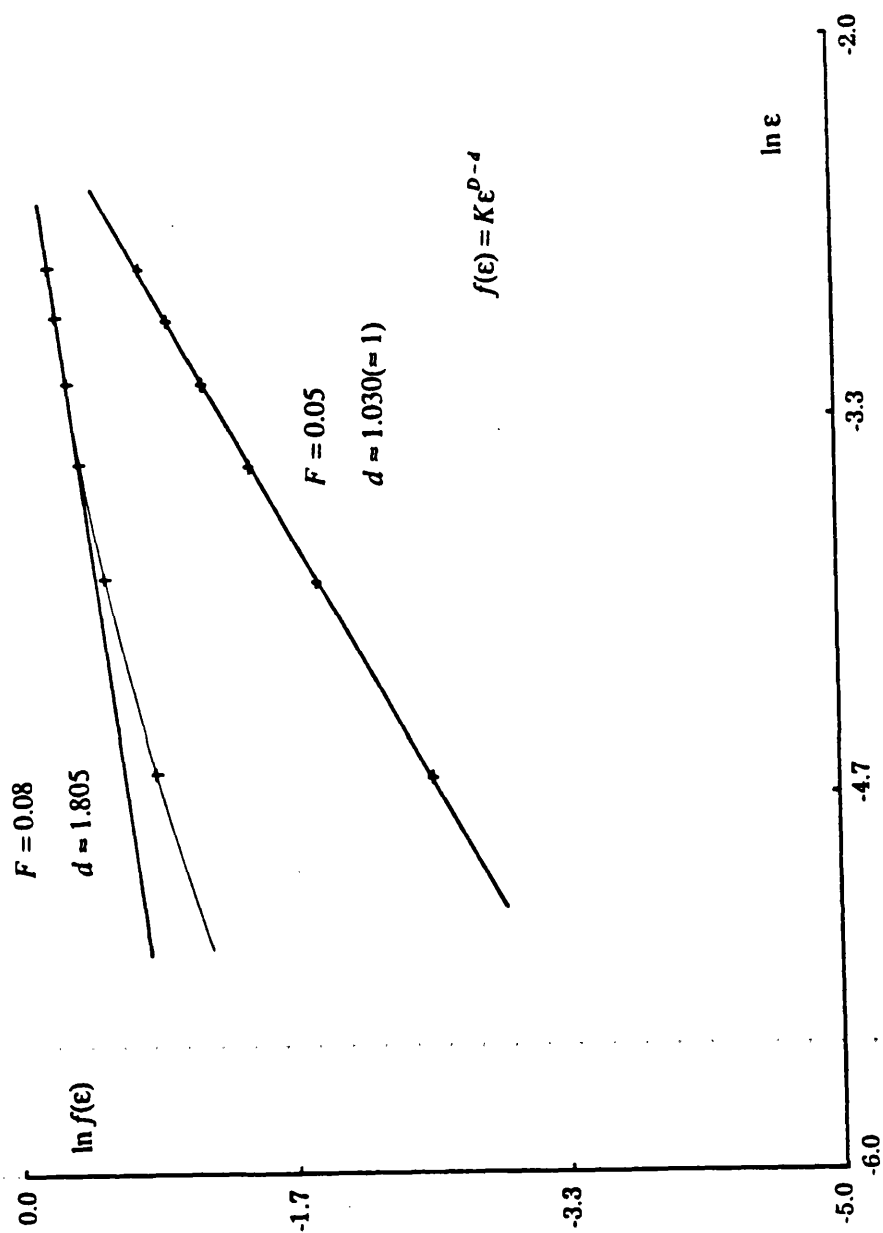


Figure 5.4 Variation of the engineering integrity (a) and the fractal dimension of the phase-space boundary (b) with the intensity of the forcing, F . In (a) the integrity measures P_m represent the fraction of grid points that do not escape within m forcing cycles.

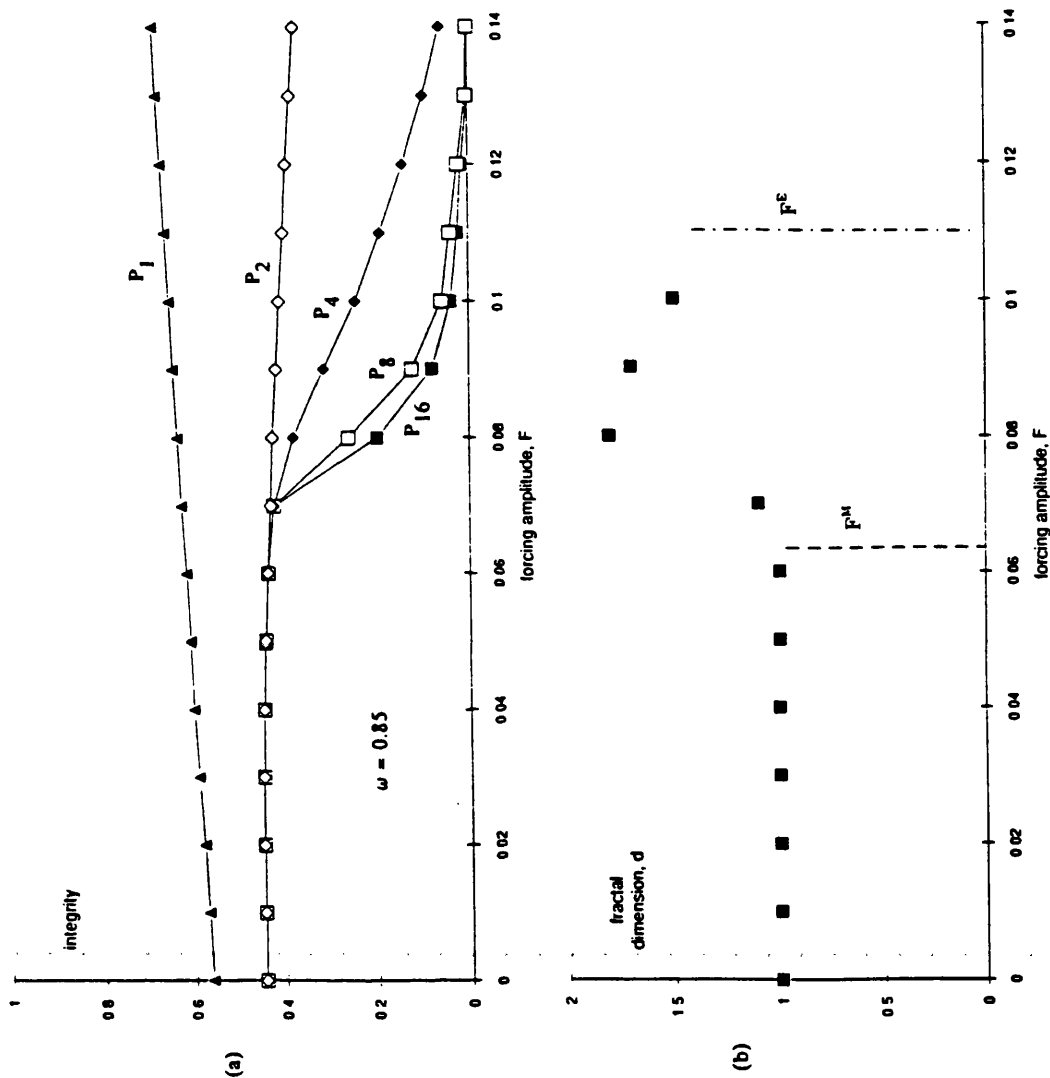
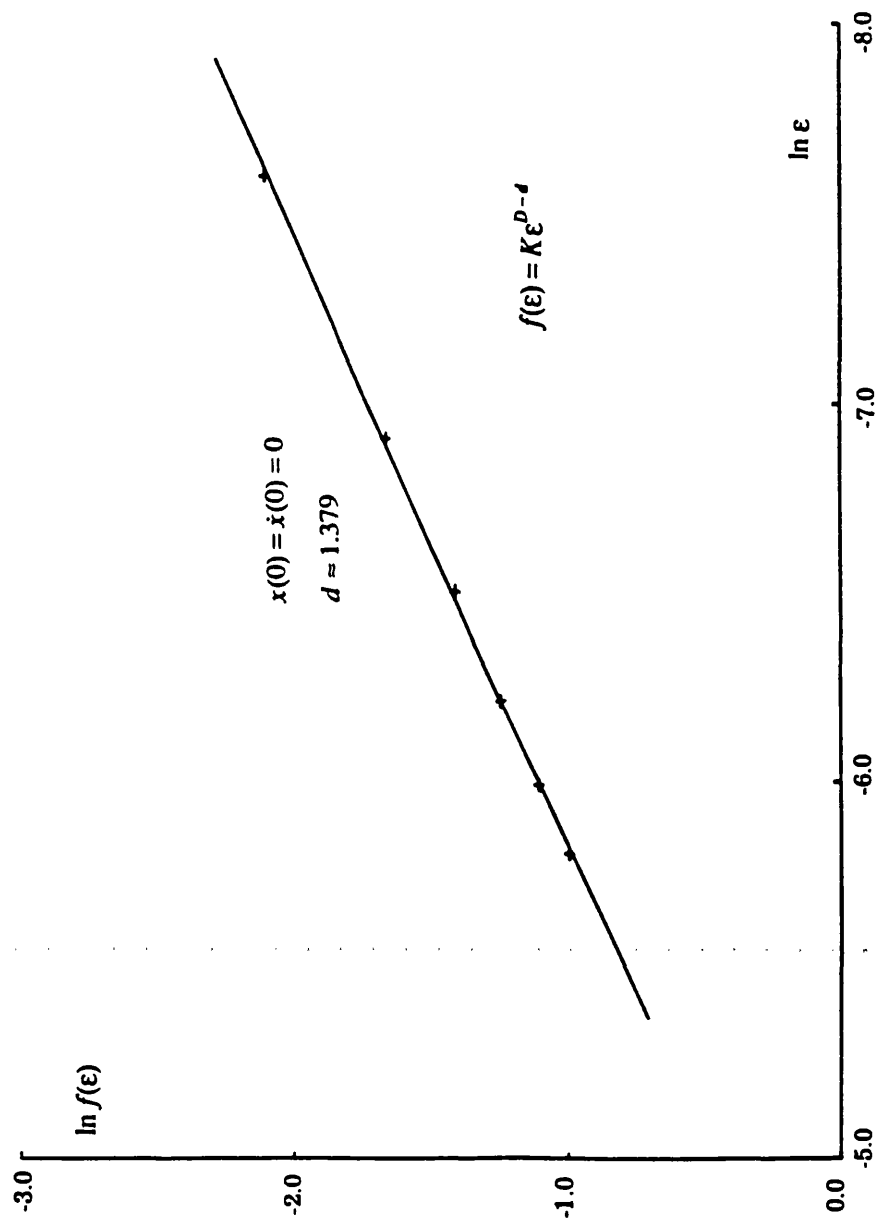


Figure 5.5 Log-log plot to estimate the *fractal dimension* of the control-space boundary.



CHAPTER 6: APPLICATION TO SHIP CAPSIZE

6.1 Introduction

Ships are subjected to a variety of environmental forces arising for example from sea waves, wind, formation of ice on the hull, as well as on-board changes such as a shift in cargo or passengers, damage or flooding. One or a combination of these factors may cause large amplitude motions which may be a threat to both the safety of the ship and those on board. They can result in structural failure, loss of control or capsize.

Although capsizing is often a very complicated event, in which a variety of sources can take an active part, the ability to predict and understand the mechanisms of large amplitude motion or capsize is of great practical importance. Existing stability criteria, are expressed in terms of minimum values for certain key features of the righting arm or the GZ curve. Static stability standards based on statistical and other analyses of the intact static stability criteria, serve a useful purpose in that under certain conditions they will be sufficient, and can give a qualitative understanding for the naval architect. However as many authors have shown, when the external dynamic influences are severe in relation to ship safety, it is no longer adequate to rely on the righting arm alone but rather on the dynamics of the ship in its environment (Bishop and Price, 1974; Wright and Marshfield, 1980; Nayfeh, 1988). The environmental conditions which have been found to be the main causes of extreme rolling are sea waves, but wind also plays a key role, and the worst conditions assumed in the design of a ship are usually specified in terms of a combination of these (Lloyd, 1989).

Although sea states are essentially random processes (but not necessarily stationary ones), a short train or *pulse* of regular waves that can excite resonant motions, can usefully be viewed as a worst-case scenario when considering capsize. For practical

purposes a long train of regular waves can be considered to have a probability of zero. Despite this, most researchers in the extensive literature on ship capsize under regular forcing, focus on just the single predominant *steady state* motion, be it harmonic, subharmonic or even chaotic. In this, they follow the tradition of classical analysis, despite the fact that for a boat, with its relatively light damping, regular waves will manifestly never persist long enough for transients to decay substantially. Not only is steady state analysis inapplicable, for this reason, but we show that it is also grossly non-conservative.

In this chapter we focus attention on the transient motions of a ship which we investigate against the background of the steady-state behaviour. Firstly, we present a steady state bifurcation diagram, in the control space of a wave height parameter, H , against wave frequency, ω , at which distinct local bifurcational phenomena take place. These typically include a jump to resonance at a cyclic fold bifurcation (saddle-node); a build-up of subharmonic oscillations at a flip bifurcation, as well as a stability boundary of capsize conditions.

Secondly, we consider the transient motions of a ship subjected to a short pulse of regular waves: and since starting conditions of a ship at the beginning of a pulse may vary widely, and in any event are unknown, we look at *all* possible transient motions. The simplest and most direct way to do this is to take a grid in the starting conditions of roll angle, θ_0 , and angular roll velocity, $\dot{\theta}_0$. Running simulations from each grid point, we can easily map out the *safe basin* from which transient motions do not lead to capsize within the specified duration of the pulse. Now as Soliman and Thompson (1989) have identified and quantified for an archetypal driven oscillator there can arise a loss of engineering integrity accompanying the rapid erosion and stratification of the safe basin as a control parameter is varied. We show here that this behaviour does indeed take place in the analytical models of two real ships giving a critical

wave height, H' , at which the ship loses the bulk of its calm water stability. We use *engineering integrity curves* and *transient capsize diagrams* to quantify this behaviour.

6.2 Mathematical modelling and the general roll equation

In order to begin a scientific investigation into ship motion and capsize a mathematical model which represents the essential aspects of the vessel and sufficiently describes the relevant dynamics of the system must be obtained. The formulation of such a model begins with approximations and assumptions, based on experiment and observation, that are necessary to simplify the almost infinite complexity of a real ship in a real environment. The solution of the problem and interpretation of the mathematical results in the context of practical experience can then lead to a revised and improved model leading to a more realistic correlation between the observed and predicted results, as well as a greater understanding of the diverse mechanisms of ship motions such as capsize.

To analyze the dynamics of a ship it is convenient to define the ship motion from a fixed co-ordinate system with the origin at the centre of mass of the ship. To completely define the motions of the ship all six-degrees of freedom must be considered; pitch, surge, heave, roll, yaw and sway (Rawson & Tupper, 1968). The first three are often referred to as symmetrical motions and are usually considered to be uncoupled from the other three which are referred to as unsymmetrical motions. The rolling motion is the most difficult to model mathematically but as many authors have shown it is often possible to de-couple the equation for roll motion from the other equations of motion by a suitable choice of co-ordinates. Numerical as well as

experimental observations have shown that at least in beam seas this is a reasonable approximation.

We consider then, in common with many authors, that the roll motion of a ship, when subjected to wave and wind moments, can be modelled by the non-linear differential equation

$$I\ddot{\theta} + B(\dot{\theta}) + C(\theta) = M(t) + W_M(\theta, t) \quad (6.1)$$

where I is the roll inertia (included added hydrodynamic inertia), θ is the roll angle ($\dot{\theta}, \ddot{\theta}$ being the angular roll velocity and acceleration respectively), $B(\dot{\theta})$ is the non-linear damping moment and $C(\theta)$ is the non-linear restoring moment.

The left hand side of the equation represents the stabilizing moments; the inertia moment is proportional to the angular acceleration of the motion. The damping moment originates from non-potential flow effects, vortex shedding around the hull, etc. A linear-plus-quadratic form of the damping moment, originally proposed by Froude, has been shown to give a very good fit to free decay experimental results from ship models, and has been supported by theoretical analyses (Gawthrop, Kounteris & Roberts, 1988). The restoring moment is created by the weight and buoyancy forces. It can be approximated by curve fitting to an experimentally obtained righting arm curve.

On the right hand side of the equation are the disturbing (de-stabilizing) moments; the wind moment, $W_M(\theta, t)$, can arise from a steady wind or a gust or a combination of both. The wave moment, $M(t)$, arises from the inclining moment whose value varies, in regular seas, harmonically according to the different positions of the ship in the travelling wave. Both these moments occur randomly in real seas but from the sake of simplicity, and for a worst case scenario, they can be considered to be deterministic quantities.

In order to illustrate the ideas presented in this chapter we have considered two different ships which have been well documented and researched following their capsizes. Both have the following specific equation of motion:

$$\ddot{\theta} + b_1 \dot{\theta} + b_2 |\dot{\theta}| + c_1 \theta + c_2 |\theta| + c_3 \theta^3 + c_4 |\theta| \theta^3 + c_5 \theta^5 = \frac{M(t)}{I} + \frac{W_M}{I} \quad (6.2)$$

The first is the *Gaul* (Morrall, 1980), with a GZ curve and damping characteristics (taken from Cadwell and Yang, 1986) as shown in figure 6.1. (Here $b_1 = 0.0555, b_2 = 0.1659, c_1 = 0.2227, c_2 = 0.0, c_3 = -0.0694, c_4 = 0.0, c_5 = -0.0131, I = 64489$). The second is the *Edith Terkol* (Kure and Bang, 1975). Here $b_1 = 0.0043, b_2 = 0.0225, c_1 = 0.385, c_2 = 0.1300, c_3 = 1.0395, c_4 = -4.070, c_5 = 2.4117, I = 1174$ (taken from Odabassi, 1976). We have approximated from these that their linear natural frequencies, ω_n , are 0.47 and 0.62 radians per second respectively and their equivalent linear damping ratios, ζ , are 0.075 and 0.01. We have assumed in common with other authors that

$$M(t) = A \sin \omega_E t \quad (6.3)$$

where ω_E is the wave frequency and A is the amplitude of the wave moment which in general will be a function both of the wave frequency and height. We have also assumed for the sake of simplicity that the wind moment is a constant value independent of roll angle and time: it is zero unless otherwise stated. We refer to the ratio of the forcing frequency to the linear natural frequency as $\bar{\omega}$, such that $\bar{\omega} = \frac{\omega_E}{\omega_n}$ and refer to a wave height parameter H, such that $H = \frac{A}{I \omega_n^2}$.

6.3 Background theory

Before summarizing the results, a brief review of the dynamics theory, mapping techniques and terms employed is appropriate (Thompson and Stewart, 1986).

Considering the single-degree-of-freedom system (6.1) it is well known that to completely define the motion of a ship under given environmental conditions (such as wave height, period, etc) and from certain initial conditions (roll angle and angular velocity), the three dimensional trajectory in $(\theta, \dot{\theta}, t)$ phase-space must be determined. Trajectories which do not lead to capsize, will eventually settle down to a bounded stable motion (for example periodic or subharmonic oscillations). Such stable steady state motion is called an *attractor*. All starting conditions which generate trajectories that tend towards an attractor, thus define its *safe basin or domain of attraction*. There may be alternative co-existing attractors, depending on the starting conditions, but we shall define the *union* of the basins of all the non-capsizing attractors as the *safe basin*.

In the case of a ship rolling in regular waves, the concept of phase space is extended by the Poincaré map, for which the continuous trajectory is replaced by a succession of points obtained by stroboscopically sampling the motion of the ship at the wave period. This sampling technique produces a sequence of points (Poincaré points) in the $(\theta, \dot{\theta})$ plane which may converge to a fixed point corresponding to a stable periodic state, converge to alternating points for subharmonic motion (a period N attractor with N points visited in sequence) or possibly to a chaotic attractor. Such sampling techniques have been employed extensively in the field of non-linear dynamics for their obvious advantages of summarizing the motion in a relatively simple fashion. For example they are very convenient for testing the stability of a given steady state as we shall show later in this chapter.

6.4 Steady State Behaviour

6.4.1 Steady state roll response

A ship can often be subjected to a train of regular waves with a given height and frequency. Often one (or both) of these parameters may gradually increase or decrease in magnitude, corresponding to a *slowly evolving* sea state. Such excitation can lead to resonance or large amplitude rolling as shown, in figure 6.2a, by the typical resonance curve for the Gaul. As we slowly vary the frequency, so that transients have always effectively decayed, we see that the roll response is a smooth function of ω at all but two values. At $\omega=0.77$ there exists a dangerous but not fatal *jump to resonance*, in the sense that the ship restabilizes at a greater amplitude of oscillation. At $\omega = 0.70$ there is a *jump from* resonance. The dashed line shows the *unstable* steady state solutions, and although they are not physically realizable, and indeed will not appear in the direct time domain simulations, they provide useful information about the global behaviour and for example play a key role in determining domains of attraction (Alexander, 1989). Figure 6.2b shows a typical resonance curve for the Edith Terkol. Here we observe four discontinuities in the stable steady state response. This higher degree of complexity is due to the local changes in stiffness (initial hardening then softening) of the GZ curve. However in both resonance curves it is observed that due to the *overall* softening nature of the restoring moment curve the peak amplitude of oscillation occurs below the linear natural frequency. Such observations clearly illustrate that resonant frequencies should be avoided, as apart from anti-rolling devices, there is little possibility of roll reduction in beam seas once the ship has been built. Such resonant behaviour can also be observed by gradually increasing the wave height from the fundamental $H = \theta = \dot{\theta} = 0$ state until the ship capsizes for a fixed value of wave

frequency. Complex bifurcations of the steady states were observed as shown in Table 1. For example at $\omega=0.80$ there is a jump to resonance at $H^A=0.21$ and then a flip to an $n=2$ subharmonic at $H^C=0.44$. A further increase in H results in a period-doubling cascade and chaotic motion leading to capsize at $H^S=0.45$. It can be seen that the optimal capsize condition, corresponding to capsize under a minimum H , occurs at about $\omega=0.70$ as indicated by the bold figures.

Table 1 : Steady state bifurcation values for the Gaul

$\omega = \frac{\omega_E}{\omega_n}$	H^A (jump to resonance)	angle of restabilization(degrees)	H^C (flip to $n=2$ subharmonic)	H^S (final Steady state capsize)
0.60	0.41	capsize	-	0.41
0.65	0.35	capsize	-	0.35
0.70	0.31	47	0.32	0.32
0.75	0.37	71	0.37	0.38
0.80	0.21	60	0.44	0.45
0.85	-	-	0.53	0.54
0.90	-	-	0.63	0.63
0.95	-	-	0.74	0.75
1.00	-	-	0.85	0.86

Having outlined that steady states can undergo various complicated bifurcations including folds, flips and ultimate capsize, we show, using a refined technique, how the ship motion in a slowly evolving sea state may be summarised using a

steady state bifurcation diagram. Such an analysis may help in predicting instabilities and capsize. Regions showing when and how the ship capsizes may be determined. Dangerous and fatal jumps to resonance, subharmonic oscillations and chaotic behaviour may be determined, all of which can add to the overall understanding of ship behaviour and capsize phenomena. We give a brief review of the analysis used, using the sampling techniques described in section 6.3.

6.4.2 Steady state Bifurcation Diagram

The relationship between two consecutive Poincaré points in the Poincaré map will be governed by a complex non-linear relationship, but close to a fixed point (whether it be periodic or subharmonic) we may approximate the Poincaré map by a 2-dimensional linear map in the form

$$\theta_{i+1} = a\theta_i + b\dot{\theta}_i$$

$$\dot{\theta}_{i+1} = c\theta_i + d\dot{\theta}_i$$

in which $\theta_{i+1}, \dot{\theta}_{i+1}$ can be evaluated numerically for any $(\theta_i, \dot{\theta}_i)$ by making a numerical time integration through one forcing period. The nature of the stability of the system may be determined by calculating the eigenvalues, λ_1, λ_2 , of the Jacobian matrix

$$\begin{bmatrix} a & b \\ c & d \end{bmatrix}$$

For stability both of these must be less than one in modulus. The stability can be characterized by the position of the eigenvalues in the complex plane (Thompson

and Stewart, 1986).

In a changing sea-state both the fixed point and the coefficients of the linear map will vary so that the eigenvalues will describe a path in the complex plane. If the eigenvalues are real one of them can cross the stability boundary at $+1$, a *cyclic fold (a saddle-node bifurcation)*, or at -1 producing a *flip bifurcation* (a transition to resonance of order $n=2$). These events are clearly of interest to the naval architect (Bishop, Leung & Virgin, 1986). The fold point (points A and B in figure 6.2a) corresponds to a resonant hysteresis jump which may cause the ship to capsize if the resulting transients are large enough to carry the ship beyond its righting moment limit, or may cause the ship to oscillate at a different (and often considerably larger) amplitude. The crossing at -1 results in the ship oscillating in a $n=2$ subharmonic manner. This, as has been shown, is often the precursor of chaotic oscillations and hence capsize (Virgin, 1987).

Using such stability properties we have drawn a *steady state bifurcation diagram* which summaries the bifurcational behaviour of the ship over a whole range of frequencies and wave heights. We focus most attention just below $\omega=1$ as resonant phenomena will normally govern ship safety. Figure 6.3a shows the bifurcation diagram for the Gaul such that $W_M=0$. Bifurcations such as those shown in table 1 can easily be seen from this diagram; at $\omega = 0.75$ the ship initially oscillates in a periodic manner, but as H is increased the ship makes a *dangerous but not fatal* jump to resonance at A_1 in which the ship starts to oscillate at an increased amplitude. A reduction of H at this stage would cause a jump from resonance at B_1 , giving rise to a region of resonant hysteresis as typically shown in figure 6.2a. A further increase of H beyond A_1 results in a flip bifurcation at C and as can be seen the ship capsizes shortly afterwards at $H^S=0.38$. By keeping H constant and varying the frequency also allows us to determine the regions of resonant hysteresis

in the frequency plane. Indeed in real situations *both* the wave frequency and height change simultaneously and such behaviour can be interpreted by this diagram. The *steady state stability boundary*, (H^S, ω) indicates the region of inevitable capsize. Figure 6.3b shows the bifurcation diagram for the same ship subjected to a steady wind moment by incorporating a static bias term in eqn (1). Fig 4 shows the effect of this on the potential energy content of the ship. The ship can be thought of as a ball rolling in the potential well defined by the potential energy curve. It can be seen that this asymmetry increases the likelihood of capsize by lowering the steady state stability boundary. At $\omega = 0.85$, $H^S = 0.26$ for the biased system, whereas $H^S = 0.54$ for the unbiased case.

6.5 Transient Behaviour

6.5.1 Safe basins

As has been shown in the previous sections, a ship subjected to a train of regular waves can exhibit a multitude of modes of capsize (Kuo & Odabassi, 1975) as well as having various types of stable steady states. Indeed these steady states can undergo intricate bifurcating patterns until they reach the point of capsize (Thompson, 1989).

In this section we consider the *transient motions* of a ship subjected to a short pulse of waves, by making *safe basin* studies, as they are both easier to perform, and at the same time more relevant to ship capsize than the steady state analyses. There are several reasons for this.

Firstly, for a ship with its relatively light damping, regular waves will evidently

never persist long enough for transients to have decayed substantially for steady state behaviour to take place. A short pulse of regular waves can thus be viewed not only as a worst-case scenario, but as a more realistic representation of a sea state than a long train of regular waves.

Secondly since the starting conditions of a ship at the beginning of a pulse may vary widely, and are indeed unknown, we must look at *all* motions rather than focus obsessively on one predominant steady state.

Finally we show that by making such a transient analysis the area of the safe basin, $A(H, \omega)$, can fall dramatically at a steep cliff at H^t , which can often be at a small fraction of H^s , the wave height at which the final attracting steady state loses its stability.

By acknowledging that a ship from $\theta_0, \dot{\theta}_0$ can experience various combinations of wave height, wave frequency and wind moments, we can say that the five dimensional *phase-control space* spanned by $(\theta_0, \dot{\theta}_0, H, \omega, W_M)$ defines the ensuing motion. (Poincaré phase space has already been defined as $\theta, \dot{\theta}$ space while control space refers to the external environmental parameters such as H, ω or W_M). To determine a safe basin, we use fourth order Runge Kutta numerical time-integrations from a simple grid of starts, typically 100 by 100. Each integration is continued until either the roll angle *exceeds* a capsizing criterion, θ_c , at which point the ship is deemed to have capsized, or the maximum allowable number of cycles, $m(=16)$, is reached, in which case it is assumed that the ship will remain upright under these conditions (Rainey & Thompson, 1990). In this way we can define a set of points in the five dimensional space that do not capsize in m cycles and hence define a transient safe basin (Thompson & Soliman, 1990). In this study we have chosen $\theta_c = \pi$ for the Gaul and $\theta_c = \theta_v = 0.88$ for the Edith Terkol.

Specifying the controls and taking a grid in the $(\theta_0, \dot{\theta}_0)$ plane allows us to draw the

conventional cross-sections in the phase-space of the starting conditions: while specifying $\theta_0, \dot{\theta}_0$ (say (0,0) in the case of the ship starting originally in its equilibrium position in calm water) and taking a grid in (H, ω) plane allows us to draw the cross-section of the transient basins in the two-dimensional control space.

In contrast to the steady state analysis, we are making no note of the final steady state motion (attractor) of the ship to which the non-capsizing motions might settle, whether it is harmonic, subharmonic, small amplitude, large amplitude or chaotic oscillations. At many control settings there can be of course many competing attractors, as in a region of resonant hysteresis, some with exceedingly small regions of attraction.

6.5.2 Erosion of the safe basins

Keeping $\omega=0.85$, a value of the forcing frequency that is of considerable interest because it is close to the optimal capsize condition for the Gaul, the safe basins are shown in phase-space (figure 6.5a) for fifteen equally spaced values of the normalised wave height parameter, $h(=\frac{H}{H^s})$. It can be seen that there little change in size or position of the transient basins up to $h \approx 0.60$. However after that the basin boundary becomes fractal (infinitely textured) due to a *homoclinic tangling* at H^M in the underlying dynamics (Grebogi, Ott & Yorke, 1987). Starts within this fractal zone lead to *chaotic transients* which oscillate hesitatingly for an arbitrary length of time before the ship either capsizes or settles to a safe steady state harmonic rolling. Moreover, fractal zones are particularly sensitive to initial conditions; external forces such as an impact load or random noise can often push trajectories across basin boundaries and thus cause a ship oscillating originally in a safe basin to oscillate in an unsafe basin and hence cause capsize (Gwinn & Westervelt, 1986,

Soliman & Thompson, 1990). This phenomena is not serious in itself, provided that the fractal zone to which it is confined remains as a thin layer around the edge of the boundary, as it does for H just above H^M . However as H is further increased the fractal boundary soon becomes incursive with thick finger-like striations penetrating into the very heart of the central zone resulting in a dramatic erosion of the safe basin. Here we can quantify the size of the basin, A , within the window represented by our grid, by recording the proportion of starts that do not capsize within m wave periods. As can be seen from the integrity curves (figure 6.6a) the ship retains practically all of its still water stability up to a critical value H^I (≈ 0.32), and thereafter loses almost all of it. Here we loosely define H^I as the largest wave height in which the ship retains its calm water stability. In the next section we make a more formal definition of H^I .

This behaviour clearly illustrates how the steady state analysis that predicts the final capsize at H^S (≈ 0.54) dangerously over-estimates the overall stability of the ship. Such results clearly display, for a designer, that H^I should be adopted in preference to H^S in defining the operational locus in the (H, ω) domain.

Similar studies were made for the biased system as shown in figures 6.5b and 6b. The effect, as expected is to reduce the value of H^I as exemplified by the integrity curves. We have also made a safe basin study for the Edith Terkol (figures 6.5c, 6.6c). Here we observe that unlike the previous cases considered, the erosion of the safe basin is both less dramatic and starts to take place at a relatively small value of H . The reasons for such behaviour are discussed later on.

6.5.3 Transient capsizing Diagram

Figure 6.7 shows the safe domain in control space assuming that the ship was originally in its equilibrium position, $\theta_0 = \dot{\theta}_0 = 0$. As can be seen the minimum H required to cause the ship to capsize occurs around the resonant frequencies. The combination of a steady wind moment is to further destabilize the ship, in that the basin boundary seems to become lower. Such diagrams clearly summarise the type of environmental conditions a calm ship subjected to a train of regular waves and wind can sustain.

Indeed by choosing $\theta_0 = \dot{\theta}_0 = 0$ gives us an approximate locus for the (H^t, ω) curve. As shown from the previous section, the phase-space basin is often swiftly eroded across its entire central region resulting in a well defined loss of area at H^t . To pin-point the latter we do not need to employ a massive grid of starts but can make just a small number of trial simulations (or model tests) in which a relatively calm ship is suddenly subjected to a short pulse of regular waves. Indeed a trial simulation from the ambient state at the origin might be adequate to locate the cliff at H^t with sufficient precision for practical purposes.

However, as shown earlier the value of H^t in which the ship loses *most* of its calm water stability is sometimes not so well defined. It is thus more convenient to plot in the (H, ω) plane, contours of (H_p^t, ω) where we define H_p^t as the value of wave height in which the ship has lost $P\%$ of its calm water stability. Indeed, the three-dimensional (A, H, ω) surface completely defines the area of the safe basin for any given H and ω . By fixing ω , and taking a cross-section in the (A, H) plane gives us the typical integrity curves, whereas fixing A we may obtain a contour of transient stability (H_p^t, ω) . (H_{100}^t, ω) then represents the contour in which the ship has lost all of its calm water stability i.e. H just above H^S , whereas (H_0^t, ω) represents

the contour in which the ship retains all of its calm water stability. These two contours represent upper and lower bounds on the transient stability; (H', ω) can then be chosen for the required margin of safety. Figure 6.3a shows several transient contours. It can be seen that steepest *cliff* occurs at about $\omega=0.70$.

6.6 Roll Damping

As is to be expected, both the steady state and transient behaviour of the *Gaul* and the *Edith Terkol* were different, as each was designed to withstand different environmental conditions. However by examining the the *normalised* integrity curves of each ship we may make a relative, if not completely justified, comparison. As can be seen the *Edith Terkol* loses its stability at a much lower value of H/H^S than the *Gaul*. We believe, that this feature is mainly due to the fact that the *Edith Terkol* was much more lightly damped than the *Gaul*.

Indeed making numerical simulations of an archetypal capsizing model with both linear and nonlinear stiffnesses and linear damping ratios of $\zeta=0.005, 0.025, 0.05$ and 0.15 reveals that the damping level determines the process of the erosion of the safe basin (see figure 6.8) and hence the transient capsizing diagram. This study uses the canonical escape equation of Thompson (1989) both with and without the stiffness nonlinearity, the linearized system being deemed to fail if the displacement x exceeds unity: more details of this comparative analysis will be given in a forthcoming paper (Thompson, Rainey & Soliman, 1990). This type of behaviour, although difficult to analyze practically due to the nonlinear damping effects, can help the naval architect in his design. Bilge keels can be designed such that a *minimum* damping level can be

achieved for a given ship.

6.7 Conclusions

(a) Using steady state analysis, we have drawn an (H, ω) bifurcation diagram. We have defined regions of inevitable capsizing; dangerous and fatal jumps to resonance as characterised by a fold point; and subharmonic instabilities as characterised by a flip bifurcation. The optimal capsizing wave height occurs at about 70% of the linear natural frequency and obviously that frequency should be avoided. This behaviour is obviously very important to the naval architect and such a diagram would obviously be helpful to his dynamic analyses of ship stability.

(b) We have used a simple and direct method for finding the critical wave height by analysing the transient basins and engineering integrity curves. We have shown that using this method several important deductions can be made.

Roll stability analysis using the classical methods, such as harmonic balance, which locates the main attractor, tests its stability (using a perturbation or Liapunov analysis) and then follows the evolution of daughter attractors, abandoning each in turn as it becomes unstable, is both a daunting, if not impossible prospect (strictly impossible in detail due to the inevitable appearance of subharmonics of infinitely higher order). We have used numerical path following routines to overcome this problem. However whichever technique is used the results can be misleading in terms of ship stability. We have shown that the ship up to H^t retains all its calm water stability, and thereafter loses almost all of it, as exemplified by the integrity curves. Classical methods would

find the ship stable up to H^S which is obviously, for practical purposes, grossly non-conservative. Using Liapunov functions, in estimating the domains of attraction, would also be quite impossible due to the homoclinic tangencies and hence the extremely complex shape of the safe basins.

(c) By plotting (H'_p, ω) contours we can make a critical judgement for the safe operational locus (H', ω) of a ship subjected to a short pulse of regular waves. The sudden loss of safe basin does moreover suggest that a transient capsize diagram can offer a useful and repeatable index of capsizability, that might have important implications for naval architects (Rainey & Thompson, 1990).

(d) We have also summarized the behaviour of the ship in parameter space. We found that when a ship is subjected to a train of regular waves, from its equilibrium position, safe and capsizing combinations of wave height and frequency may be specified. It was observed that resonant frequencies were particularly dangerous as small wave heights were required to cause capsize.

(e) The roll damping plays a most critical part in the erosion of the safe basins. This was illustrated by making a safe basin study on both *linear and nonlinear* archetypal capsize models. Such behaviour demonstrates, that as well as designing a ship with a minimum criterion for certain characteristics of its righting lever arm, a *minimum damping level* should be included to ensure greater stability.

(f) The stability analysis considered using both phase space and parameter space diagrams can equally be applied for non-capsizing but dangerous motions. For example we have considered that the Edith Terkol loses its stability at the angle of

vanishing stability ($\theta_v \approx 46^\circ$): however for practical purposes motions can become dangerous to both the passengers and the structure of the ship when the ship executes large amplitudes. So for a more reasonable analysis the ship can be deemed dangerous once the motion exceeds a given angle of roll (such as 25°) and that angle rather than the angle of vanishing stability can be chosen as a limiting criterion. Indeed by comparing a realistic approach with the extreme limiting condition gives a feel for the *margin of safety* made in this transient analysis; analogues to elastic and plastic design in the field of structural engineering can be observed here.

(g) Several ship phenomena such as the capsize mode can be understood in terms of the advances made in recent research in the field of nonlinear dynamics

Figure 6.1 Details of the ship characteristics for the Gaul.

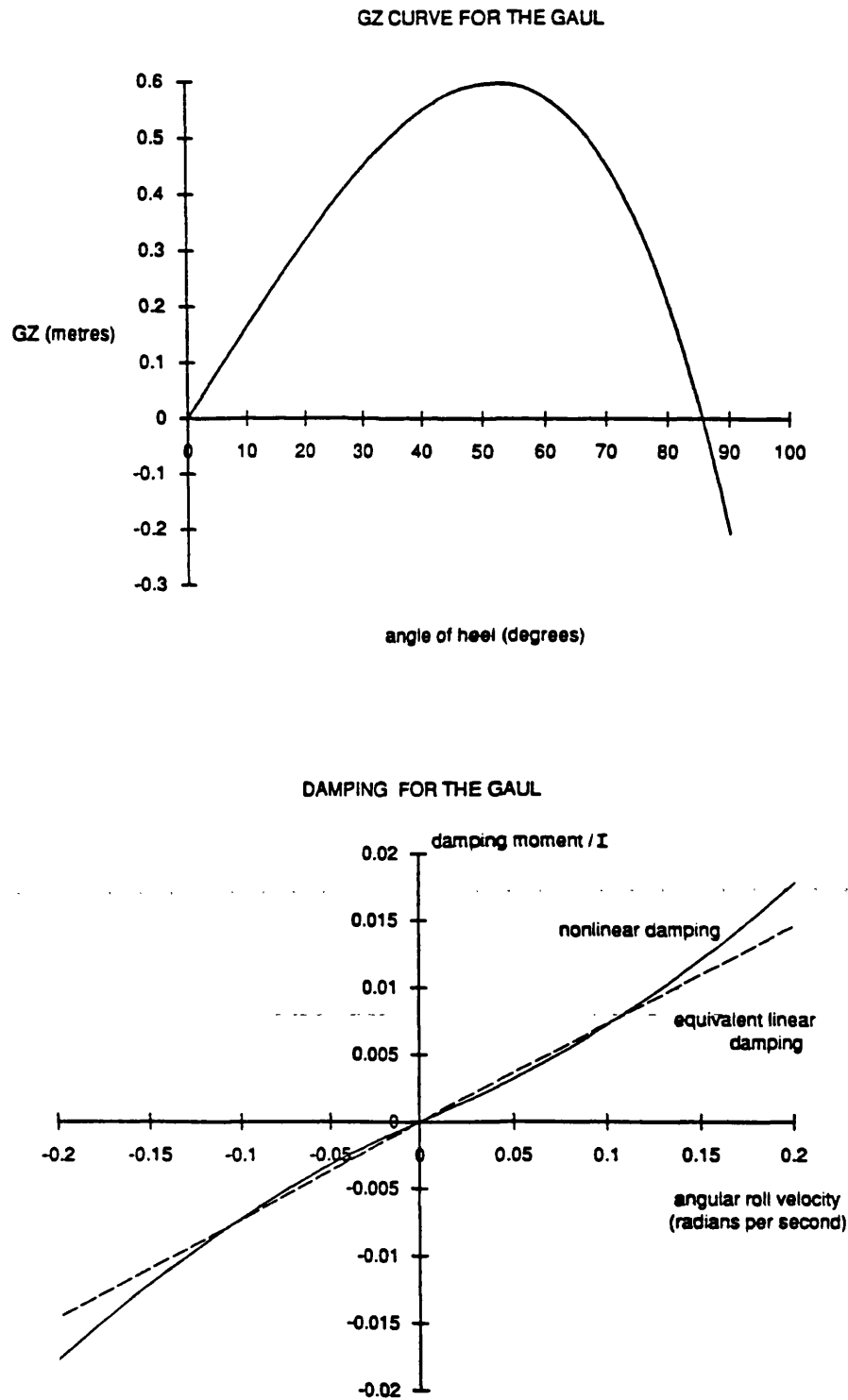


Figure 6.2 Resonance response curves for the(a) Gaul ($H=0.24$)(b) Edith Terkol ($H=0.01$)

Solid lines represent stable steady state response; arrows indicate a jump to and from resonance.

Dashed lines represent the unstable steady state response.

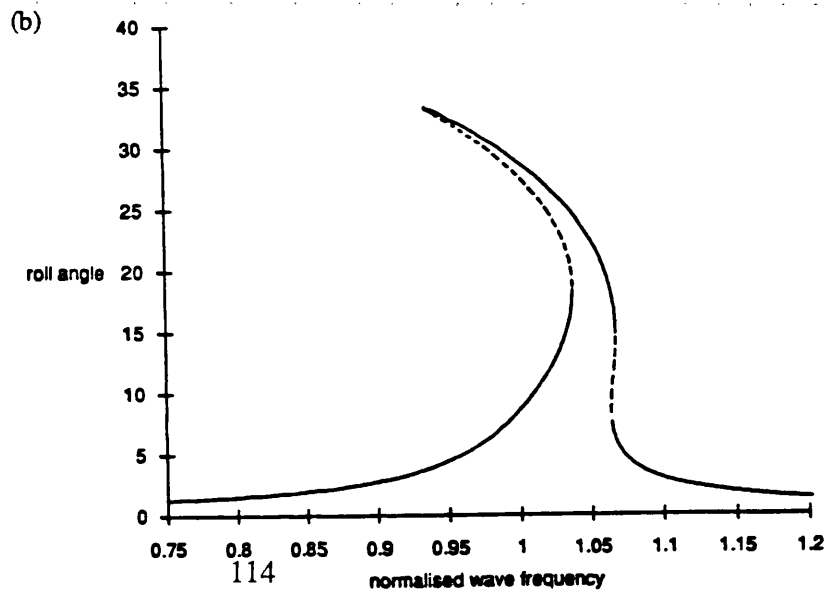
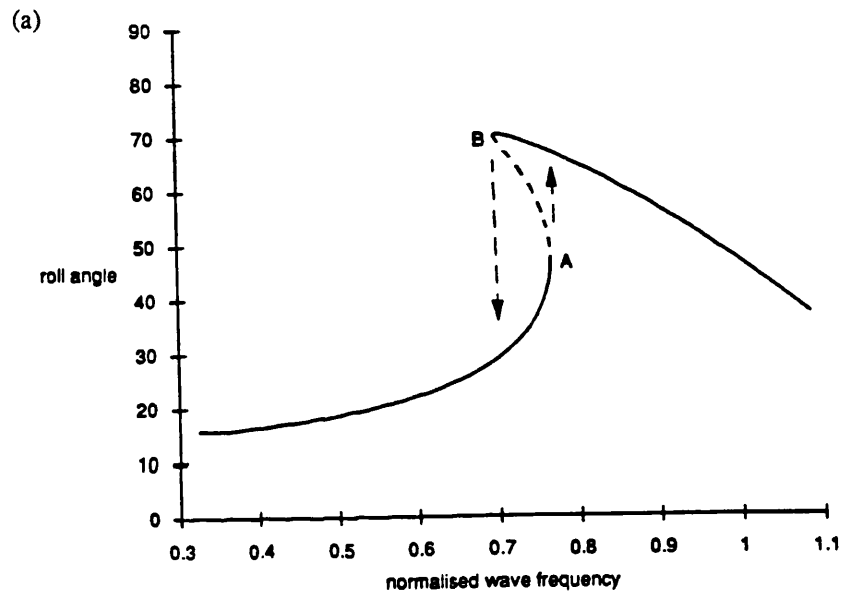


Figure 6.3 Steady state Bifurcation diagrams for the Gaul depicting:
 Dangerous folds (jumps to resonance (A_1); from resonance (B_1))
 Fatal folds (instantaneous capsizes (A_2))
 Subharmonic instabilities (period doubling (C))
 Capsize from a chaotic attractor
 Regions of inevitable capsizes.
 (a) Unbiased system ($W_M=0$)
 (b) Biased system ($W_M=2000$)
 Contours of transient stability, (H'_p, ω) , are also shown in figure 6.3a.

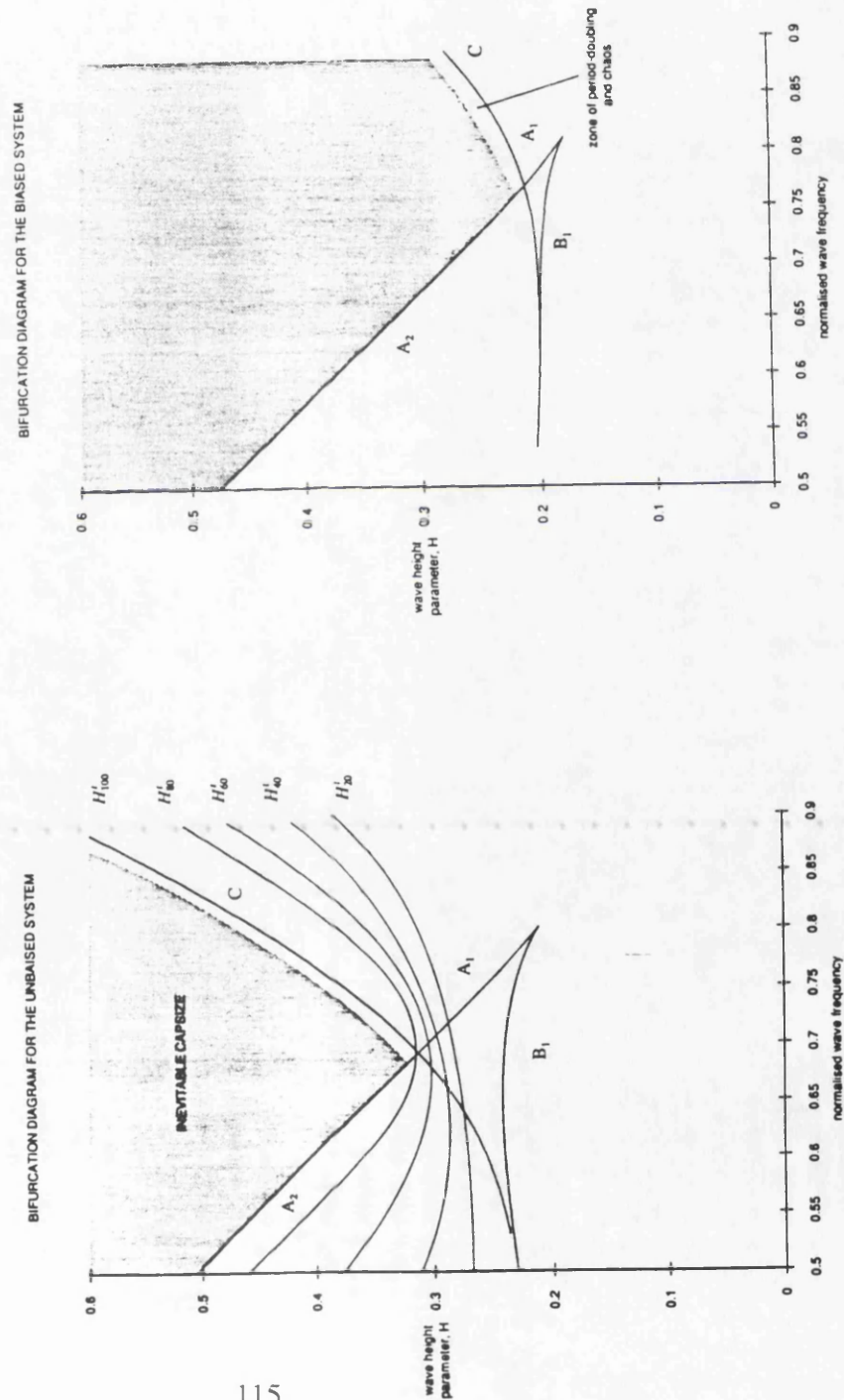


Figure 6.4 Potential energy content of the Gaul.
 Solid line represents the unbiased system ($W_M=0$).
 Dashed line represents the biased system ($W_M=2000$)

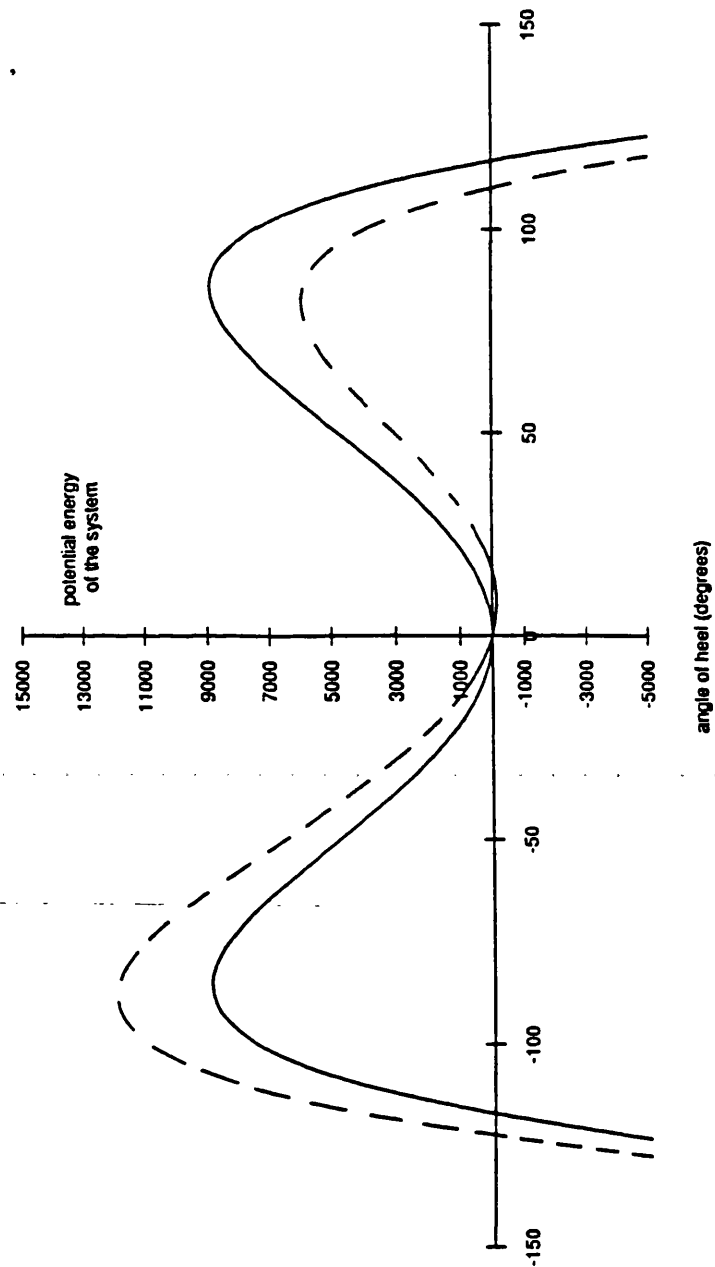


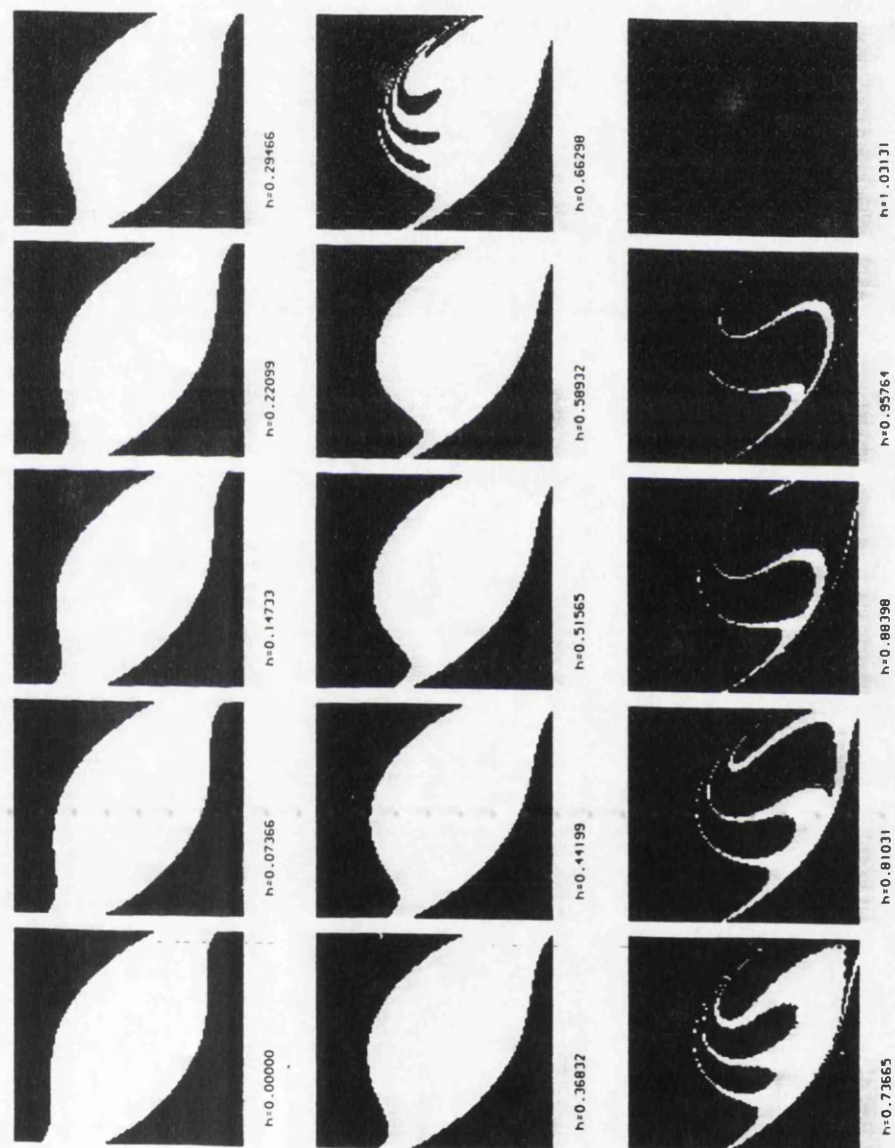
Figure 6.5 Safe basins in phase space for $\omega=0.85$.

White represents initial conditions whose trajectories *do not* capsize within 16 forcing cycles

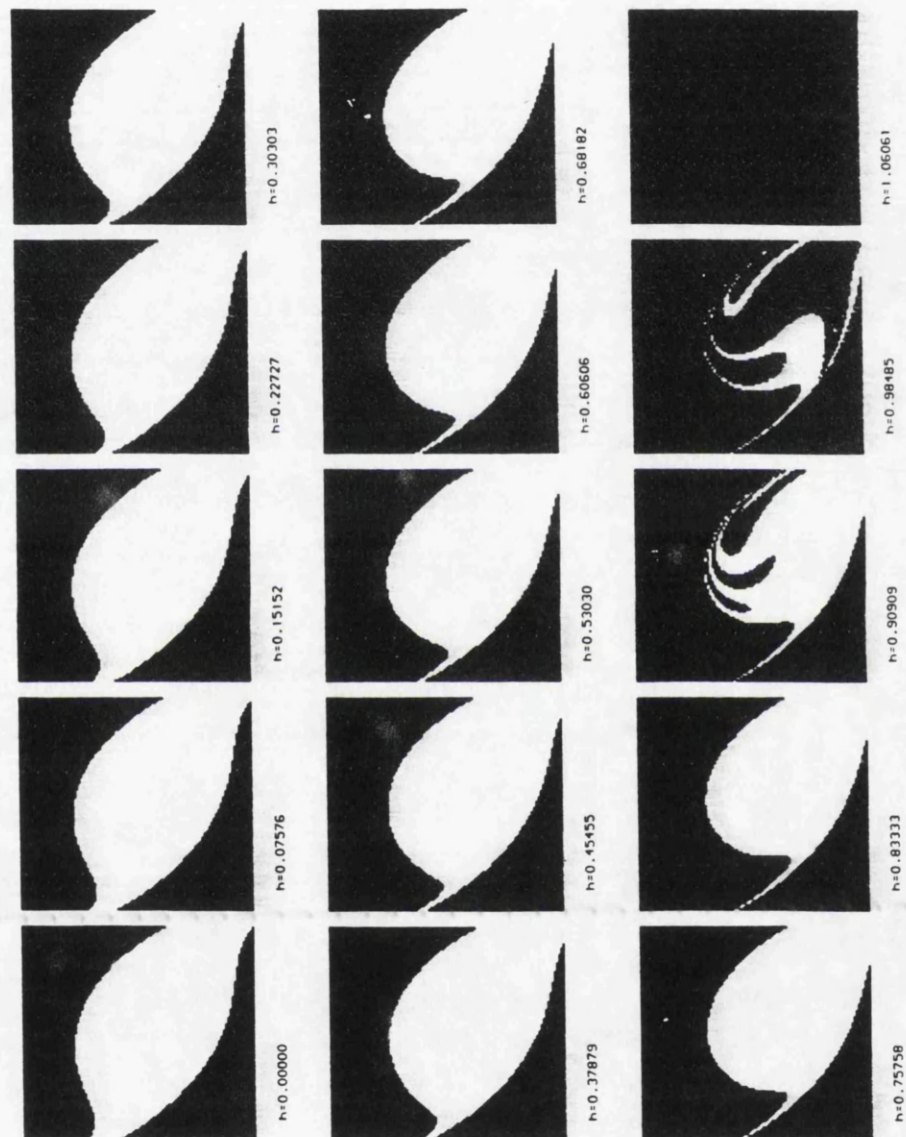
Black represents initial conditions whose trajectories *do* capsize within 16 forcing cycles.

For each basin the normalised wave height parameter $h=H/H_1^S$ is shown and:

(a) Gaul, $W_M=0.0$: $-1.74 < \theta < 1.74$ $-1.05 < \theta < 1.05$: $\theta_C = 3.142$, $H^S \approx 0.54$



(b) Gau1, $W_M=2000.0$: $-1.74 < \theta < 1.74$ $-1.05 < \phi < 1.05$: $\theta_c = 3.142, H^s \approx 0.26$



(c) Edith Terkol, $W_M=0.0$: $-0.88 < \theta < 0.88$ $-0.52 < \phi < 0.52$: $\theta_c = 0.88, H^s \approx 0.22$

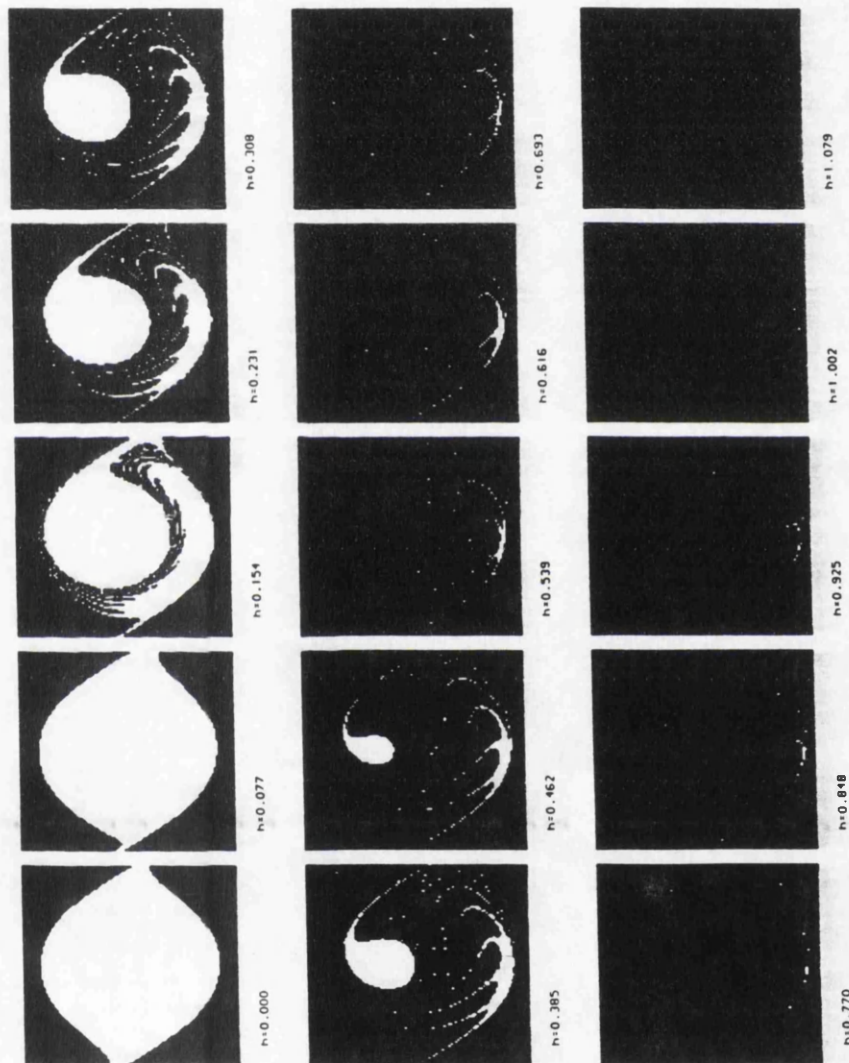
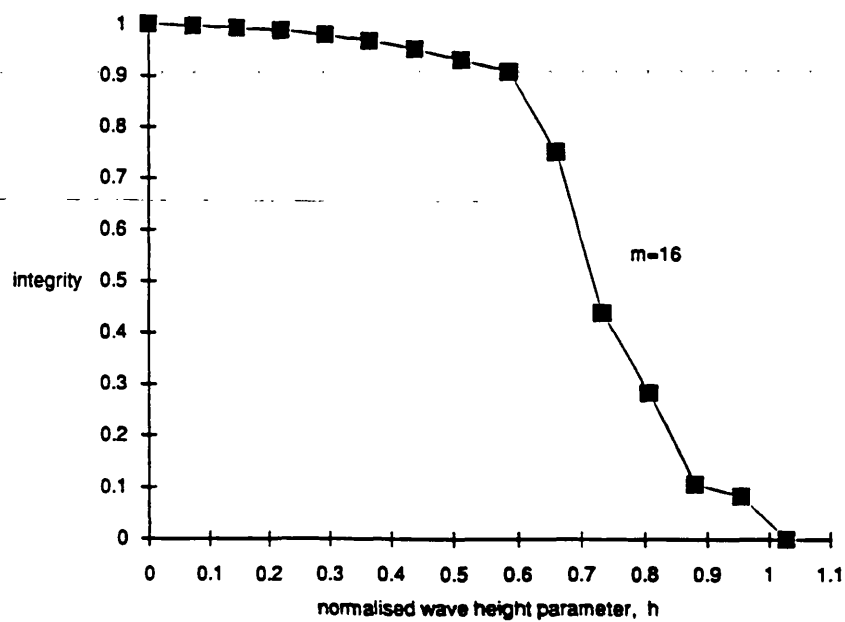
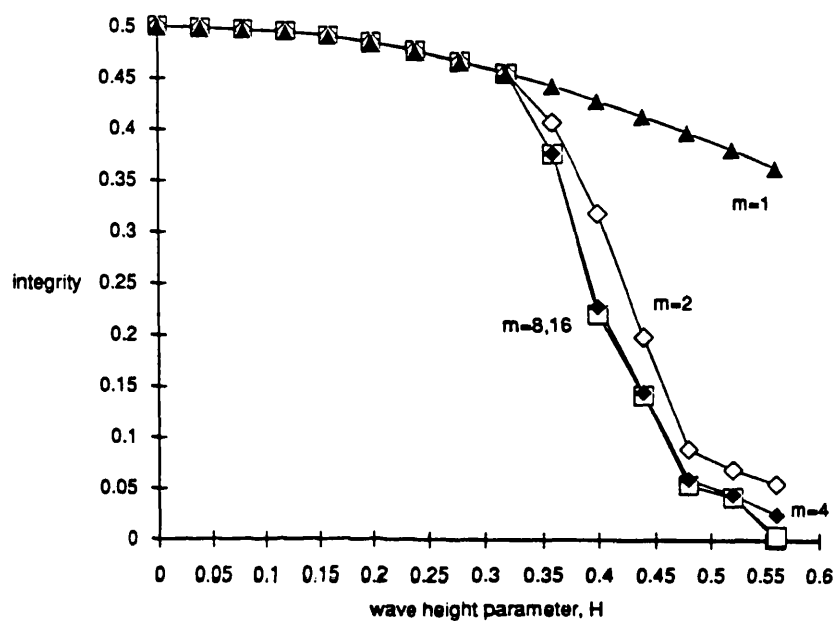
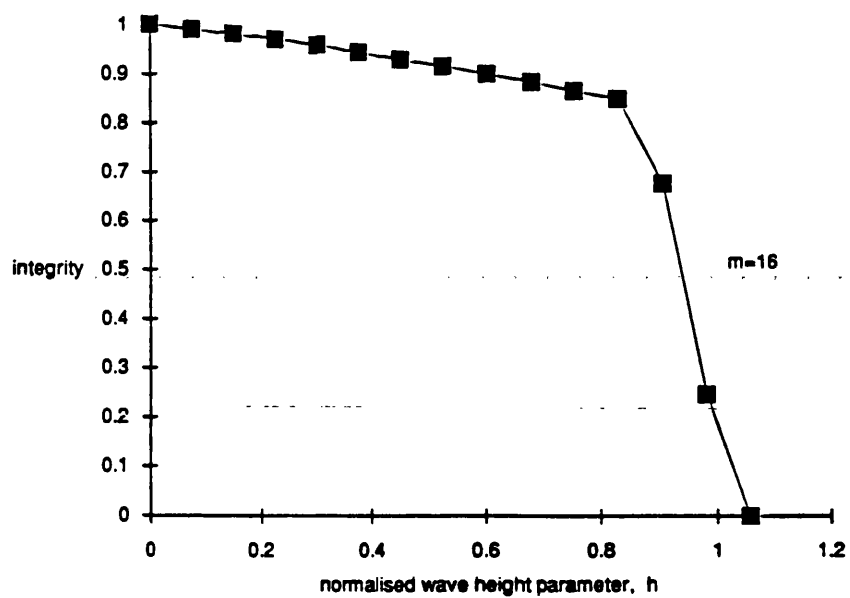
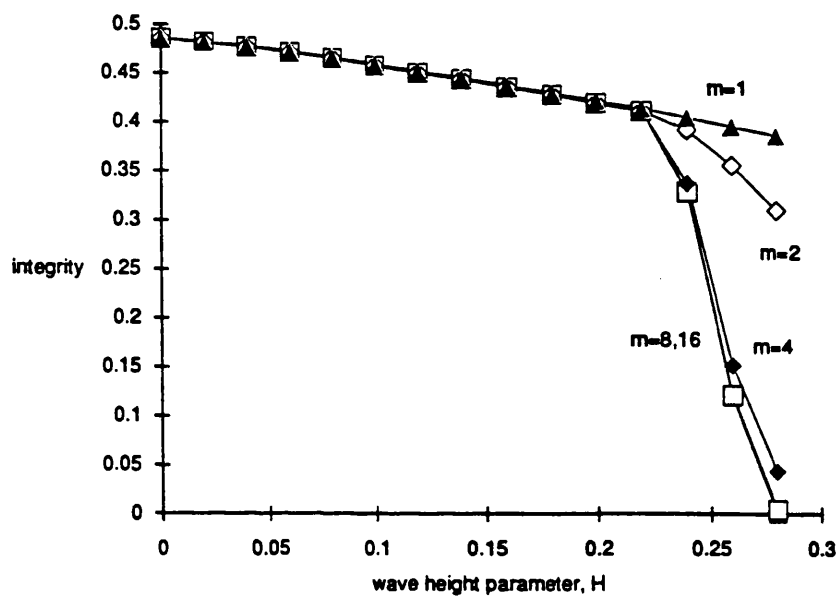


Figure 6.6 Integrity curves representing the erosion of the safe basin described in figure 6

(a) Integrity curves for figure 6.5a



(b) Integrity curves for figure 6.5b



(c) Integrity curves for figure 6.5c

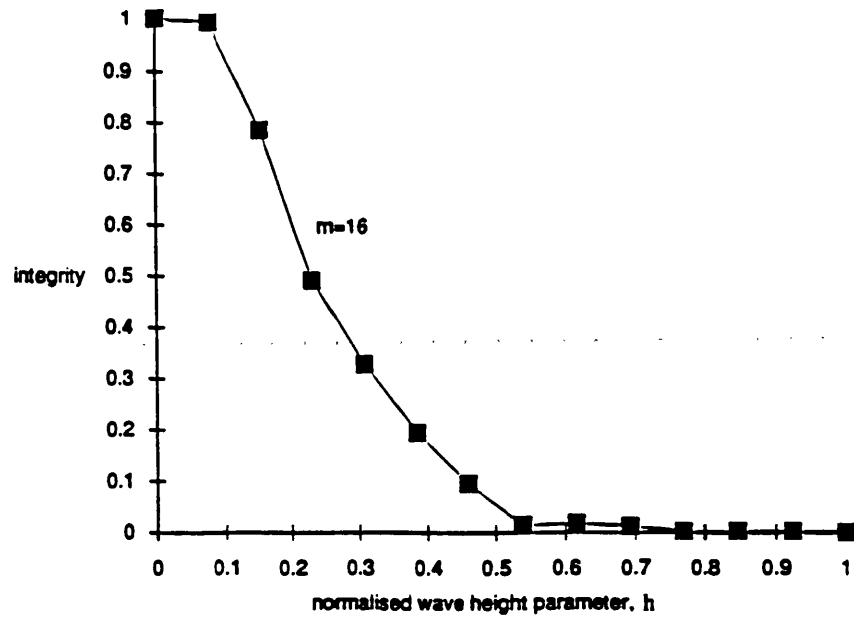
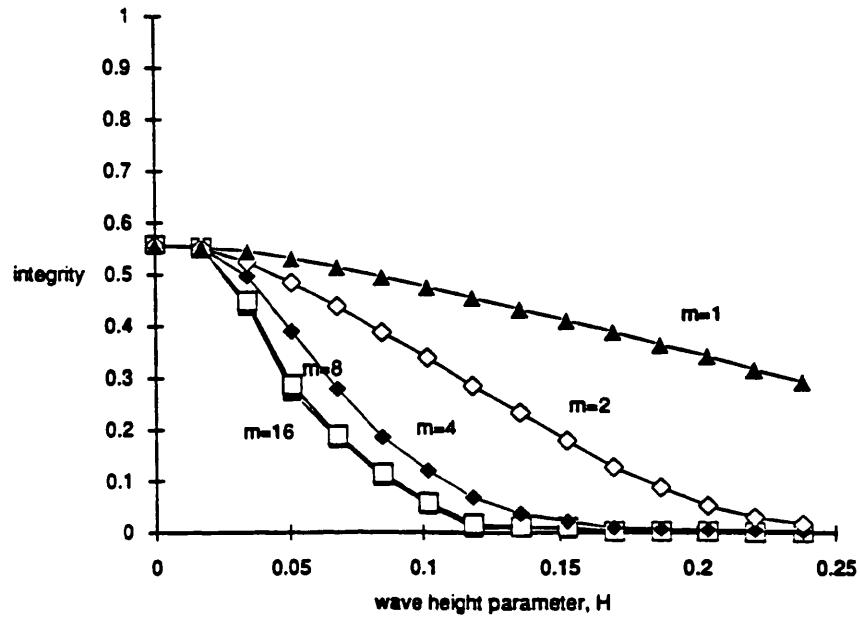


Figure 6.7 Safe basins in (H, ω) control space for the Gaul.

$$\theta(0) = \dot{\theta}(0) = 0, \theta_c = 1.57$$

Black represents no capsize within 16 forcing cycles

Grey represents capsize between 4-16 cycles

White represents capsize within 4 cycles

The dashed lines represent the steady state bifurcation values as described in figure 6.3.

(a) Unbiased system ($W_M=0$)

(b) Biased system ($W_M=2000$)

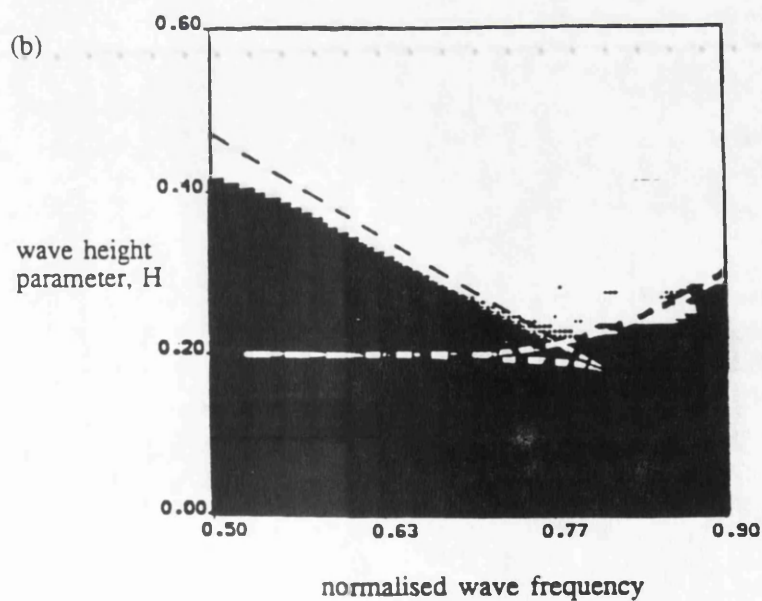
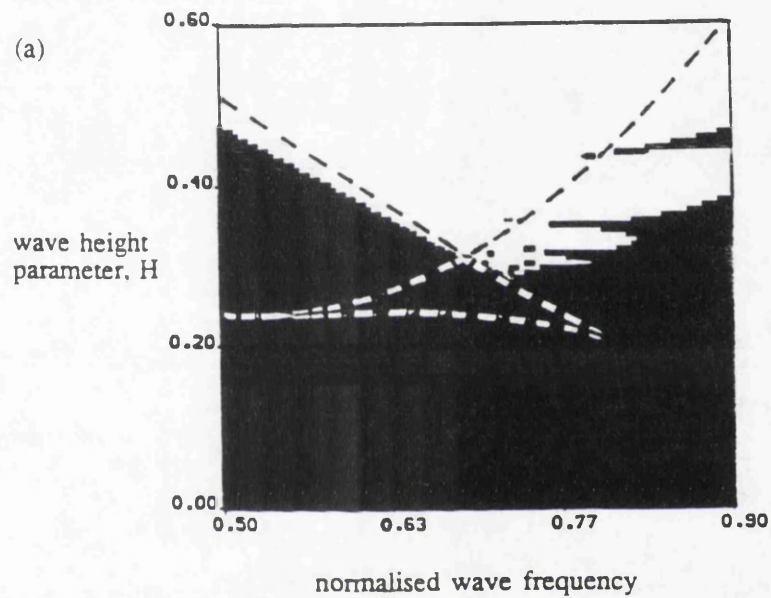
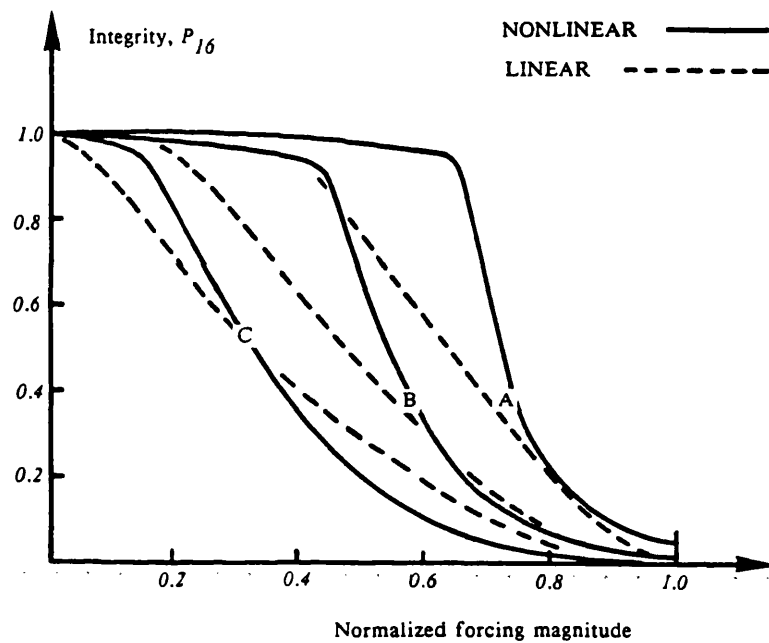


Figure 6.8

Figure 6.8 The effect of damping on the erosion of the safe basins for linear and nonlinear archetypal capsize models. Here the canonical escape equation and its linearization are considered with $\omega = 0.85$ and $\beta = 2\zeta$.

INTEGRITY at various DAMPING LEVELS for NONLINEAR & LINEAR SYSTEMS
(Canonical escape equation and its linearization, with $\omega=0.85$)



$$\text{Detuning-damping ratio} = d = (\bar{\omega} - \omega_n) / \zeta \omega_n = -0.15 / \zeta$$

Curves A:

$$\beta=0.1$$

$$\zeta=0.05$$

$$d=-3$$

Curves B:

$$\beta=0.05$$

$$\zeta=0.025$$

$$d=-6$$

Curves C:

$$\beta=0.01$$

$$\zeta=0.005$$

$$d=-30$$

CHAPTER 7: CONCLUSIONS

Although nonlinear dynamical systems exhibit extremely complex phenomena, we conclude that a nonlinear analysis has important engineering relevance, particularly when simplicity can be derived out of such complexity.

Indeed as many engineering systems are neither linear nor nearly linear, and are modelled by nonlinear equations for which closed-form analytical solutions are unobtainable, a detailed numerical analysis may be a daunting prospect for the typical engineer. A reliance on linear equations may indeed be simpler but would not give a realistic representation of his system.

This was outlined in chapter 2 where it was shown that typical nonlinear systems can exhibit complex steady state and transient behaviour. Steady state attractors, of which there can be many co-existing at the same parameter values, can typically include point equilibria, periodic oscillations (harmonic and subharmonic), quasi-periodic solutions and chaotic attractors. The variation of a system parameter can result in complex bifurcations of these attractors. The mechanisms include the well-known local bifurcations (such as the well-known jumps to and from resonance), together with subharmonic cascades, intermittencies, crises, etc. In addition it is important to recognize that in typical dynamical systems several attractors often coexist at fixed parameter values. This has lead to much interest in basins of attraction, and how they too undergo changes and metamorphoses. Under the variation of a control parameter, as the attractors move and bifurcate, the basins also undergo corresponding changes and metamorphoses.

Indeed the main conclusion of this thesis is that the study of basins of attraction has important engineering relevance as there can exist a rapid loss of engineering integrity accompanying the rapid erosion and stratification of the basin.

In chapters 3 and 4 we explored the theoretical and engineering significance of the basin erosions that occur under increased forcing. Various measures of engineering integrity of the constrained attractor were introduced: a global measure assesses the overall basin area; a local measure assesses the distance from the attractor to the basin boundary; a velocity measure is related to the size of impulse that could be sustained without failure; and by introducing a superimposed noise excitation, we quantify the response in terms of a stochastic integrity measure.

Since engineering systems may be subjected to pulse loads of finite duration, attention should be given to both the absolute and transient basin boundaries. The significant erosion of these at homoclinic tangencies was particularly high-lighted in this study, the fractal basins having a severely reduced integrity under all four criteria. Our conclusions were as follows;

(a) *Global integrity curves* clearly indicate basin boundary changes in terms of the size of the basin of attraction. A homoclinic tangency of the stable and unstable manifolds, resulting in a fractal basin, dramatically enhances the erosion of the basin of attraction.

(b) A hysteresis jump or movement of the attractor as a system parameter is varied can cause the attractor to move much closer to the basin boundary without any change in the size of the basin of attraction. This is clearly indicated by the *local integrity curves* and the *impact integrity curves*.

(c) The addition of noise can cause qualitative changes in the appearance of an attractor. Increasing the noise intensity increases the sensitivity of attractors to noise-induced hopping (in our case usually causing trajectories to escape). The stochastic integrity measure clearly quantifies such behaviour as well as the relative response of different

attractors subjected to the same noise level. *Stochastic integrity curves* give the relative response of a naturally occurring sequence of attractors subjected to a fixed noise intensity.

In chapter five we discussed how these results and ideas may have considerable engineering relevance. It was argued that in engineering design, against boat capsize or earthquake damage, for example, a study of the safe (transient) basins should augment, and perhaps entirely replace, conventional analysis of the steady state attracting solutions. This is particularly important for engineering systems which are subjected to a short pulse of regular forcing, which will manifestly never persist long enough for transients to have decayed. In these fields the phenomena that we have outlined give a qualitative guide to behaviour, rather than specific quantitative results. The fine details of the fractal structure are indeed unlikely to be important in an engineering context, especially since they will vary with the starting phase. Rather it is the rapid erosion of the bulk of the phase-space basin (a feature that is independent of the starting phase) that is of vital concern to engineers designing systems subjected to periodic or near periodic forcing.

In chapter 6 we applied the ideas presented in the previous chapters to the problem of ship capsize. Here we made a detailed numerical analysis of the steady state and transient motions of the semi-empirical nonlinear differential equations, which have been used to model the resonant rolling motions of two ships. Examination of the safe basin in the space of the starting conditions showed that transient capsizes can occur at a wave height that is a small fraction of that at which the final steady state motions lose their stability. It was seen that the basin is eroded quite suddenly throughout its central region by gross striations, implying that transient capsize might be a reasonably repeatable phenomenon, offering a new approach to the quantification of ship stability

in waves. Such an approach has the twin advantages of being both conceptually simpler, and at the same time more relevant, than one based on the steady state rolling motions. The latter analysis was shown to be dangerously non-conservative.

The ideas developed during the course of this thesis could be extended on both the theoretical and practical levels. On the theoretical side more research should be made into the microscopic dynamics of the erosion process itself. The effect of system parameters, such as the damping, on basin erosion can then be considered. This would then lead to an overall assessment on how the erosion process may be suppressed by changing certain parameters, such that engineering systems may be designed accordingly. Such an analysis can then be refined by investigating the erosion phenomena on higher degree-of-freedom models which would give a more realistic representation of a real engineering system operating in a real environment. The solution of the problem and the interpretation of the mathematical results in the context of practical experience can then lead to an improved and revised model leading to a more realistic correlation between the observed and predicted results, as well as a greater understanding on the mechanisms of the nonlinear dynamics of engineering structures.

REFERENCES

- N.A. ALEXANDER 1989 *Journal of Sound and Vibration* **135**, 63-77. Production of computational portraits of bounded invariant manifolds.
- F.T. ARECCHI, R. BADI and A. POLITTI 1984 *Physics Letters* **103A**, 3-7. Scaling of first passage times for noise induced crises.
- R.H. ABRAHAM and H.B. STEWART 1986 *Physica* **21D**, 394-400. A chaotic blue sky catastrophe in forced relaxation oscillations.
- R.E.D. BISHOP and W.G. PRICE 1974 *Probabilistic Theory of Ship Dynamics*. London, Halsted.
- S.R. BISHOP, L.M. LEUNG & L.N. VIRGIN 1986 *Proc. 5th Int. Conf. OMAE, ASME, Tokyo*. 175-185 Predicting incipient jumps to resonance of compliant marine structures in an evolving sea.
- J.B. CADWELL & Y.S. YANG 1986 *Proc. Int. Conf. on the SAFESHIP Project: Ship stability and safety, London, RINA*. Risk and reliability analysis applied to ship capsizing: A preliminary study.
- S.H. CRANDALL and W.D. MARK 1963 *Random vibrations in mechanical systems*. Academic Press, London.
- J.P. CRUTCHFIELD, J.D. FARMER and B.A. HUBERMAN 1982 *Physics Reports* **92**, 45-82. Fluctuations and simple chaotic dynamics.
- R. van DAMME and T.P. VALKERING 1987 *J. Phys A: Math. Gen.* **20**, 4161-4171. Transient periodic behaviour related to a saddle-node bifurcation.
- M.I. DYKMAN, C.J. LAMBERT, R. MANNELLA, P. MARTAÑO, P.V.E. McCLINTOCK, S. SOSKIN, N.G. STOCKS, and J.M.T. THOMPSON 1989 *Conf. Noise and chaos in nonlinear dynamical systems*. Stochastic dynamics of chaotic nonlinear dynamical systems.

- E. ESCHENAZI, H.G. SOLARI, R. GILMORE 1989 *Physical Review A* **39**, 2609-2627. Basins of attraction in driven dynamical systems.
- P.J. GAWTHROP, A. KOUNTERIS & J.B. ROBERTS 1988 *Journal of Ship Research* **32**, 101-111. Parametric identification of nonlinear ship roll motion from forced roll data.
- C. GREBOGI, E. OTT, and J.A. YORKE 1986a *Physical Review Letters* **56**, 1011-1014. Metamorphoses of basin boundaries in nonlinear dynamical systems.
- C. GREBOGI, E. OTT, and J.A. YORKE 1986b *Physical Review Letters* **57**, 1284-1287. Critical exponent of chaotic transients in nonlinear dynamical systems.
- C. GREBOGI, E. OTT, and J.A. YORKE 1987 *Physica* **24D**, 243-262. Basin boundary metamorphoses: changes in accessible boundary orbits.
- C. GREBOGI, S.W. McDONALD, E. OTT, and J.A. YORKE 1983 *Physics Letters A* **99** 415-419. Final state sensitivity: an obstruction to predictability.
- J. GUCKENHEIMER and P.J. HOLMES 1983 *Nonlinear Oscillations, Dynamical Systems and Bifurcations of Vector Fields*, Springer-Verlag, New York.
- E.G. GWINN and R.M. WESTERVELT 1986a *Physica* **23D**, 396-401. Horseshoes in the driven, damped pendulum.
- E.G. GWINN and R.M. WESTERVELT 1986b *Physical Review A*, 4143-4155. Fractal basin boundaries and intermittency in the driven damped pendulum.
- C. KUO & A.Y. ODABASSI 1975 *Proc. Int. Conf. on the Stability of Ships and Ocean Vehicles*, Strathclyde. Application of dynamic systems approach to ship and ocean vehicle stability.
- K. KURE & C.J. BANG 1975 *Proc. Int. Conf. on the Stability of Ships and Ocean Vehicles*, Strathclyde. The ultimate half roll.
- A.R.J.M. LLOYD 1989 *Seakeeping: Ship behaviour in rough weather*. Ellis Horwood.
- B.B. MANDELBROT 1977 *The fractal geometry of Nature*. New York:Freeman

- S.W. McDONALD, C. GREBOGI, E. OTT and J.A. YORKE 1985 *Physica* **17D**, 125-153. Fractal basin boundaries.
- D.R. MILLER, G. TAM, R.C.T. RAINEY and R. RITCH 1986 *Investigation of the use of modern ship motion prediction models in identifying ships with a larger than acceptable risk of dynamic capsize*. Report prepared by Arctec Canada Ltd. for the Transportation Development Centre of the Canadian Government. Report no TP7470E.
- F.C. MOON and G.X. LI 1985 *Physical Review Letters* **55**, 1439-1442. Fractal basin boundaries and homoclinic orbits for periodic motion in a two-well potential.
- F.C. MOON 1987 *Chaotic vibrations: an introduction for applied scientists and engineers*. Wiley, New York.C.
- A.MORRALL 1980 *Trans. RINA* 391-416. The Gaul disaster: An investigation into the loss of a large stern trawler.
- F. MOSS and P.V.E. McCLINTOCK (eds) 1989 *Noise in Nonlinear Dynamical Systems, Vol. 1*. Cambridge University Press, Cambridge.
- A.H. NAYFEH 1988 *Journal of Ship Research* **32**, 92-100. On the undesirable roll characteristics of ships in regular seas.
- A.H. NAYFEH and D.T. MOOK 1979 *Nonlinear Oscillations*, Wiley, New York.
- H.O. PEITIGEN and P.H. RITCHER 1986 *The beauty of fractals*. Berlin: Springer-Verlag.
- A.Y. ODABASSI 1976 *Trans. RINA* 237-256 Ultimate stability of ships.
- PEZESHKI and E.H. DOWELL 1987 *Journal of Sound and Vibration* **117**(2), 219-232. An examination of initial condition maps for the sinusoidally excited buckled beam modeled by the Duffing's equation.
- R.C.T. RAINEY & J.M.T. THOMPSON 1990 *Journal of Ship Research* The transient capsize diagram - A new method of quantifying stability in waves. (in press)
- K.J. RAWSON & E.C. TUPPER 1968 *Basic ship theory: Vol 1* Longman Inc., New

York.

M.S. SOLIMAN 1990 *Fourth International Conference on Stability of Ships and Ocean Vechiles, Naples, 24-28 Sept.* An analysis of ship stability based on transient motions.

M.S. SOLIMAN & J.M.T. THOMPSON 1989 *Journal of Sound and Vibration* **135**, 453-475. Integrity measures quantifying the erosion of smooth and fractal basins of attraction.

M.S. SOLIMAN & J.M.T. THOMPSON 1990a *Dynamics and Stability of Systems* Stochastic penetration of smooth and fractal basins of attraction (in press).

M.S. SOLIMAN & J.M.T. THOMPSON 1990b *Applied Ocean Research* Transient and steady state analysis of capsizing phenomena. (in press)

J.M.T. THOMPSON 1989 *Proc. Roy. Soc Lond. A* **421**, 195-225. Chaotic phenomena triggering the escape from a potential well.

J.M.T. THOMPSON, S.R. BISHOP, and L.M. LEUNG 1987 *Physics Letters* **121A**, 116-120. Fractal basins and chaotic bifurcations prior to escape from a potential well.

J.M.T. THOMPSON, R.C.T. RAINEY & M.S. SOLIMAN 1990 **A332**, 149-167. *Phil. Trans. Roy. Soc. Lond.* Ship stability criteria based on chaotic transients from incursive fractals.

J.M.T. THOMPSON & M.S. SOLIMAN 1990 **A428**, 1-13. *Proc. Roy. Soc Lond* Fractal control boundaries of driven oscillators and their relevance to safe engineering design.

J.M.T. THOMPSON & H.B. STEWART 1986 *Nonlinear dynamics and chaos*, Wiley, Chichester.

J.M.T. THOMPSON & Y. UEDA 1989 *Dynamics and Stability of Systems*. Basin boundary metamorphoses in the canonical escape equation. (in press)

E.C. VAZQUEZ, W.H. JEFFERYS and A. SIVARAMAKRISHNAN 1987 *Physica* **29D**, 84-94. Fractal distributions in conservative systems: direct observations of the stable manifold.

L.N. VIRGIN 1987 *Applied ocean research* **9**, 89-95 The nonlinear rolling response of a vessel including chaotic motions leading to capsize in regular seas.

L.N. VIRGIN 1988 *Journal of Sound and Vibration* **126**, 157-165 On the harmonic response of an oscillator with unsymmetric restoring force.

J.H.G. WRIGHT & W.B. MARSHFIELD 1980 *Trans. RINA* **122**, 129-144 Ship roll response and capsize behaviour in beam seas.